# MULTIMODE SQUEEZING AND QUANTUM CORRELATIONS OF DISSIPATIVE KERR SOLITONS IN OPTICAL MICRORESONATORS

A DISSERTATION
SUBMITTED TO THE DEPARTMENT OF APPLIED PHYSICS
AND THE COMMITTEE ON GRADUATE STUDIES
OF STANFORD UNIVERSITY
IN PARTIAL FULFILLMENT OF THE REQUIREMENTS
FOR THE DEGREE OF
DOCTOR OF PHILOSOPHY

Melissa A. Guidry
August 2023

# Abstract

Kerr soliton microcombs are phase-locked frequency combs generated in a microresonator via a third-order optical nonlinearity. Since their first demonstration in 2014 [1], soliton microcombs have found applications in spectroscopy [2], LiDAR [3], communications [4], and convolutional processing [5]. Experimental studies of soliton microcombs have also revealed a wealth of interesting nonlinear dynamics [6, 7, 8, 9], and fundamental research on the classical dynamics continues to-date.

This thesis is divided into two parts: (I) the modeling and experimental observation of quantum processes in multimode nonlinear photonics; and (II) the engineering of silicon carbide-on-insulator (SiCOI) integrated photonics for nonlinear and quantum technologies. Part I is general to all Kerr integrated photonics platforms. However, in experimental realizations, the choice of photonics platform matters, not only because of a variation among materials in the raw strength of the nonlinearity but also because of additional properties that influence device engineering and ultimate performance. The development of the SiCOI nonlinear photonics platform enabled the experimental quantum optics demonstrations of this thesis, and will be the focus of Part II.

# Acknowledgments

Throughout the PhD, we open the theses of our predecessors and glimpse into the unseen personal drive of science, wondering what we may one day write ourselves. As all things, the final piece is closer to a human document than that which we had imagined. In the end, I hope that all of the people who I thank here have already felt the depth of my gratitude: but it is a limitless resource, and I wish to tie the completion of this work to the names of its authors, supporters, and friends.

My thesis advisor Jelena Vučković gifted me the freedom, trust, and resources to pursue an uncertain direction. I have been happy to learn from Jelena and share her enthusiasm for quantum optics. She has given me innumerable opportunities to come into my own as a member of our field and her support has been invaluable.

My mentor Kiyoul Yang taught me a tremendous amount about Kerr combs and integrated photonics, and his experience and knowledge of the field were critical for our projects. His wisdom and belief in our direction pushed us through challenging times. I look back fondly on the many hours we shared in the lab, the many different colors of light we saw together.

Thank you to my labmates Eran Lustig, Joshua Yang, and Dominic Catanzaro: I feel singularly fortunate to work with people of good nature and excellent character.

I am grateful to my reading committee members Martin M. Fejer and Amir Safavi-Naeini for their sustained feedback on this work: in particular, for encouraging the pursuit of an analytic squeezer decomposition, which lead to results presented in Chapter 4. I am grateful to Olav Solgaard for serving as the chair of my oral dissertation committee and to Hideo Mabuchi for serving as my fifth committee member.

Thank you to my early research advisors, who all continue to encourage me long after I left their labs: Eugeniy Mikhailov, Irina Novikova, Mélanie Lebental, and Irene Fiori. Thank you to Nathalie Picqué, Lucas Deniel, Stephan Amann, and Theodor Hänsch for our ongoing collaboration (Chapter 9) and an unforgettable research visit at MPQ; to Florian Kaiser and Di Liu for hours of discussions over the years (Chapter 10); to Rahul Trivedi for serving as a mentor in quantum optics formalism (Chapter 3); to Edwin Ng and Ryotatsu Yanagimoto for their feedback on the results of Chapter 4; to Avik Dutt, Tian Zhong, and Shuo Sun for discussions and encouragement; to Jesse Lu, Guillermo Angeris, and Alexander Frenkel for advice on numerical optimization and decomposition.

Thank you to Michael, Lawrence, Shayne, Indigo, Lena, Mark, Arina, Andrey, Yetta, Jack, everyone at the fruit stand.

And thank you to Daniil, my partner in all this.

# Contents

# List of Tables

# List of Figures

# Part I

# Multimode nonlinear quantum photonics

# Chapter 1

# Introduction

The primary motivation of this Dissertation has been to explore the fundamental quantum properties of dissipative Kerr solitons (DKS) – self-assembled optical pulses in Kerr resonators driven by a continuous-wave laser source. While the topic may seem to be quite narrow in application, I would argue that it is more general than it first appears. Mathematically, the DKS state is a stationary solution of a nonlinear Schrödinger equation with dissipation, drive, and detuning: the implications of this work on Kerr resonator systems also extend to many nonlinear systems beyond nonlinear integrated photonics. For example, while we primarily consider temporal solitons born from the balance of the Kerr effect with *dispersion*, the initial drive behind formulating the Lugiato-Lefever equation (Eq. 1.1) was to describe spatial cavity solitons born from the nonlinearity balancing *diffraction* [20]. As we will see the Kerr microring resonator is a natural candidate to begin the experimental observation of the coupling of quantum fluctuations and nonlinear spatial/temporal structures.

The optical soliton is an optical field which remains unchanged with propagation, through balance of linear and nonlinear effects of the medium. As described above, the two classes are spatial and temporal solitons, where the nonlinearity balances diffraction or dispersion, respectively: this highlights the space-time analogy of nonlinear optics [21]. Both are solutions of the nonlinear Schrödinger equation. The nonlinear wave equation to describe a pulse with slowly-varying field amplitude $A(z,t)$ in distance $z$ and time $t$ propagating in a nonlinear medium, in the reference frame moving with the group velocity, is written:

$$\frac{\partial A(z,t)}{\partial z} = -ig_0|A(z,t)|^2A(z,t) - i\frac{\beta_2}{2}\frac{\partial^2 A(z,t)}{\partial t^2} \tag{1.1}$$

where $g_0$ is the nonlinear strength of the medium and $\beta_2$ represents the dispersion. The first experimental report of an optical soliton was in 1980 at Bell laboratories [22], where the authors observed soliton behavior of picosecond pulses sent through 700 m-long single-mode silica fiber,

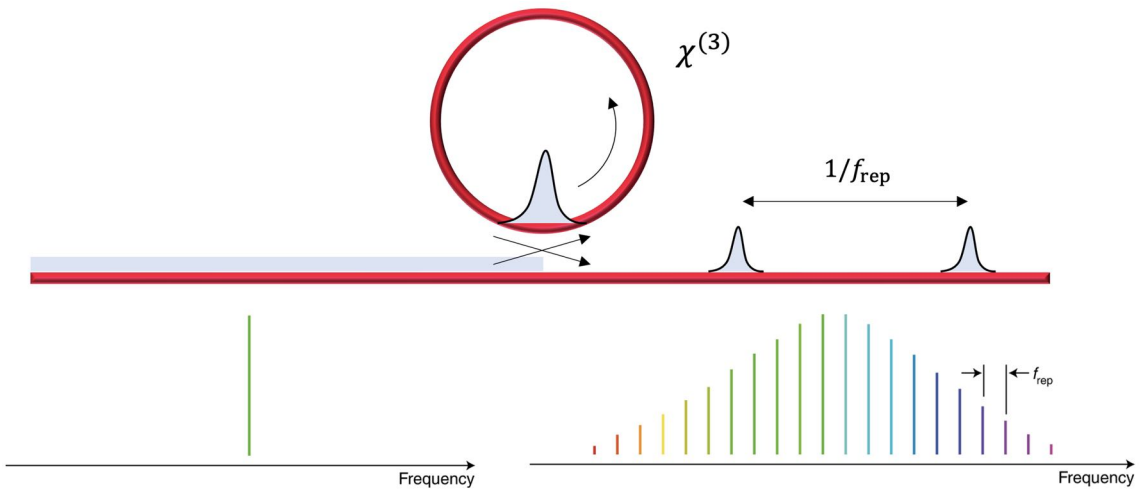


Figure 1.1: **The system under study.** A ring resonator composed of a third-order nonlinear ($\chi^{(3)}$) medium is used to generate solitons from a continuous-wave pump, injected via evanescent coupling of a bus waveguide. Bottom: A pictorial representation of the spectral composition of the pump (left) and output soliton (right). The round-trip time of the soliton pulse in the resonator is given by the inverse of the repetition rate $f_{\text{rep}}$ of the output train of pulses.

enabled by advances in optical fiber and mode-locked laser technologies. Looking at Eq. 1.1, the existence of solitons is not surprising. For Kerr media, the nonlinearity $g_0$ is positive. This term, known as *self-phase modulation*, describes an intensity-dependent refractive index and thus a time-varying refractive index for the pulse. The effect is that lower frequencies shift to the leading edge of the pulse, whereas higher frequencies shift to the back. If the dispersion $\beta_2$ is positive (*anomalous*), then the opposite effect is observed, and the two effects will balance.

What is remarkable, however, is the spontaneous formation of soliton pulses from an initial optical state which is continuous wave. Consider taking the same Kerr fiber and wrapping it on itself to form a ring resonator (Fig. 1.1), with access through an evanescently-coupled bus waveguide. The model for this system is a modification of Eq. 1.1 via the addition of dissipation ($\kappa$) and monochromatic drive ($F$), which may have a detuning ($\delta$):

$$\frac{\partial A}{\partial t} = -(\frac{\kappa}{2} + i\delta)A - ig_0|A|^2A - i\frac{D_2}{2}\frac{\partial^2 A}{\partial \theta^2} + F \tag{1.2}$$

Here the spatial coordinate is the azimuthal angle $\theta$. The switching of time and position from Eq. 1.1 is a manifestation of the application of a periodic boundary condition for each roundtrip [23]. This equation is known as the Lugiato-Lefever equation. The key feature is the pattern formation from a uniform pump, which requires symmetry breaking. As we will see, the necessary symmetry breaking occurs because of the quantum fluctuations which underlie the transition from spontaneous pair generation to a dominance of stimulated pair generation via the optical nonlinearity.

The optical mean field of the Kerr frequency comb (*i.e.*, the "classical" comb) has been modeled with great success by the Lugiato-Lefever equation (LLE), and the most commonly studied configuration is that where a single coherent pump laser (drive $F$ in Eq. 1.2) supplies parametric gain to populate the comb lines through stimulated four-wave mixing [24]. Note that spontaneous light generation is absent from the model; in order to seed threshold processes such as optical parametric oscillation (OPO), random noise must be added into every optical mode. Thus, the LLE can reveal neither the properties of the quantum state of the comb, nor the coherent dynamics of the threshold processes that drive the formation of the comb itself.

In Part I, we will show that soliton microcombs provide an excellent system for study of multimode quantum optics: (i) They provide a highly-multimode equidistant phase-locked comb (time-independent drive) which precisely balances dispersion in the resonator. (ii) They feature rich nonlinear dynamics, with many different types of states and switching behaviors. Study of their quantum properties can actually reveal physics of their classical nonlinear dynamics. (iii) Technologies for soliton capture, stabilization, and imaging are very well-developed since the first discovery in 2014. Since the LLE on its own does not consider nor has the capability to include quantum dynamics, it must be extended. We introduce a model, based on linearization of the full quartic Hamiltonian, which we use to to study quantum fluctuations in the DKS itself as well as in the states leading up to DKS formation.

In the second chapter in the thesis, we start by writing the linearized model for the below-threshold quantum comb in a Kerr microresonator with a monochromatic pump. This system is convenient because its symmetry allows for simplicity while still showing how the multimode parameters in the comb influence the measurable properties. We will show the theoretical prediction for two-photon correlations and quadrature squeezing, how they are affected by dispersion, mode crossings, and other parameters. In the third chapter of the thesis, we will describe the full linearized model for the soliton microcomb and the photon correlation measurement that we used to validate it. In the fourth chapter of the thesis, we discuss theoretical predictions for quadrature squeezing in the soliton microcomb and its stages of formation.

In some sections of this Part I of the thesis, we will be including some general derivations related to fundamental quantum optics, which may be found elsewhere in the literature, usually in pedagogical context. I hope that the inclusion of such derivations will serve as a starting point for those who wish to learn about the field.

# Chapter 2

# Below-threshold quantum comb

Before studying the quantum fluctuations that exist within the dissipative Kerr soliton, we will start by building up the multimode formalism in a simpler system by describing the quantum fluctuations within a signal-idler quantum comb [25] . The signal-idler quantum comb is the output quantum optical field of a system where a monochromatic pump laser couples to a single mode of a Kerr microring in the regime below the optical parametric oscillation threshold. In this regime, entangled photon pairs are spontaneously generated in pairs of resonator modes. To-date, this system has received perhaps the most attention in integrated quantum optics, as it (i) enables parallelized generation of entangled pairs [26] or single photon sources [27], which has direct applications to quantum technologies; and (ii) is readily modeled (modes are only coupled pair-wise and are simple to analyze) and experimentally generated (no stringent device requirements to sustain a below-threshold comb). In this chapter, I begin by applying the multimode linearized quantum model to this simple case, with both analytic expressions and generalized numeric solver that, in subsequent chapters, will be applied to the full multimode quantum system that describes solitons. I then compare the theory to experimentally-observed two-photon correlations.

The nonlinear optics process that underlies Kerr comb formation is four-wave mixing (FWM) via the third-order optical nonlinearity $\chi^{(3)}$: one pair of photons is created while another is destroyed. This process obeys energy conservation and requires phase-matching. This is to say that if a pair of photons is destroyed with frequencies $\omega_a$ and $\omega_b$, then two photons labeled $c$ and $d$ will be created at frequencies which obey the following equation: $\omega_a + \omega_b = \omega_c + \omega_d$. In the microring resonator, we consider conservation of angular momentum for the phase-matching condition, which simplifies to an azimuthal mode number matching condition: $m_a + m_b = m_c + m_d$. The nonlinearity, mode volume, and mode overlap will determine the nonlinear coupling rate between the photons. However, for interactions between modes of the same transverse mode family with similar frequencies, we can consider the mode overlap to be near-unity (see Chapter 6 for a case where conversion happens between different transverse modes).

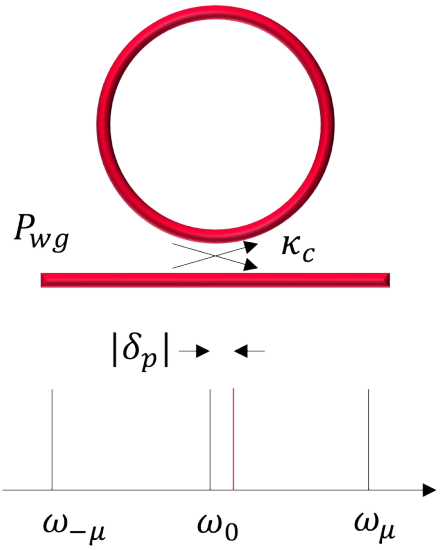


Figure 2.1: **Schematic of the ring resonator and its input waveguide.** The pump power in the waveguide is $P_{\mathrm{wg}}$, which couples to the resonator with rate $\kappa_c$. Azimuthal modes in the same transverse mode family are separated in frequency and defined by their azimuthal mode number $\mu$. The pump is injected into mode labeled $\mu = 0$ henceforth, with frequency detuning of $\delta_p$. In the absence of dispersion, the modes are separated by a fixed frequency which is the free-spectral range of the resonator.

## 2.1 Monochromatic drive of a Kerr microring

We consider a single transverse mode family, where each azimuthal mode in the family is defined by its azimuthal mode number $\mu$ with optical frequency $\omega_\mu$. Each mode is associated with an energy decay rate $\kappa_\mu$ which is related to the quality factor by $Q = \omega_\mu/\kappa_\mu$. For simplicity, we center the mode indexing $\mu$ around the pumped mode $\hat{a}_0$. Considering the four-wave mixing conditions above, we see that two photons will be destroyed from the pump modes to create pairs of photons only within the modes symmetric around the pump (Fig. 2.2). Thus the symmetric cavity modes $\hat{a}_\mu$ and $\hat{a}_{-\mu}$ are populated by parametric gain from the pump:

$$H_0 = \sum_\mu \left[\omega_\mu \hat{a}_\mu^\dagger \hat{a}_\mu + g_0(\hat{a}_0^{\dagger 2}\hat{a}_\mu \hat{a}_{-\mu} + \text{h.c.})\right] + H_p \tag{2.1}$$

where $H_p$ is the Hamiltonian for the coherent drive and $g_0$ is the nonlinear coupling strength which is inversely proportional to the effective mode volume $V_{\mathrm{eff}}$:

$$g_0 = \frac{\hbar\omega_p^2 c n_2}{n_0^2 V_{\mathrm{eff}}},$$

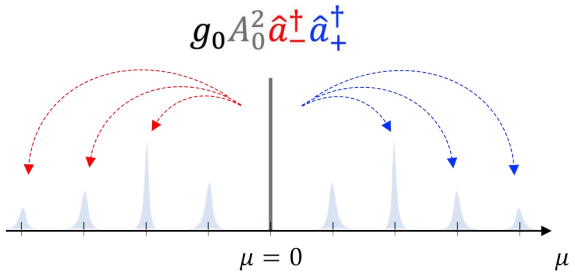


Figure 2.2: **Schematic of the signal-idler quantum comb.** A monochromatic drive at azimuthal mode $\mu = 0$ drives pair generation in the symmetric modes. The intracavity pump mode amplitude is $A_0$ and $g_0$ is the nonlinearity. In this schematic, linearization of the system has been applied (Section 2.3). As we will see in Section 2.5, the dispersion of the modes around the pump will influence the linewidth and intensity of pair generation in the below-threshold lines.

where $n_2$ is the Kerr refractive index and $n_0$ is the linear refractive index. The coherent drive is parametrized by the amplitude of the pump $A_p$ and the pump frequency $\omega_p$,

$$H_p = A_p \hat{a}_0 e^{-i\omega_p t} + \text{h.c.} \tag{2.2}$$

The amplitude of the drive field relates to the waveguide input power via the relation between intracavity amplitude and input/output power:

$$A_p = \sqrt{\frac{\kappa_c P_{\text{wg}}}{\hbar \omega_p}}$$

Here, $\kappa_c$ is the coupling rate of the cavity to the input waveguide and $P_{\text{wg}}$ is the power in the input waveguide. We define the detuning of the pump from its resonance as $\delta_p = \omega_0 - \omega_p$, an important parameter experimentally for accessing different Kerr comb states.

Although in experimental systems mode frequencies feature some spectral disorder due to mode mixing and geometric imperfections, the dispersion of the modes is typically dominated by lower orders of the Taylor expansion, which largely determine the system behavior. So, we write optical resonance frequencies $\omega_\mu$ as a Taylor series around the pump mode $\omega_0$:

$$\omega_\mu = \omega_0 + \sum_{n=1} \frac{1}{n!} D_n \mu^n \tag{2.3}$$

Imposing the mode number matching condition $m_a + m_b = m_c + m_d$, we had in effect made a rotating wave approximation, assuming that the free spectral range greatly exceeds dispersion and cavity linewidth. In this regime, it is convenient to move into the reference frame obtained via the

unitary transformation using $\hat{U}(t) = e^{i\hat{R}t}$ where $\hat{R} = \sum_\mu(\omega_p + D_1\mu)\hat{a}^\dagger_\mu\hat{a}_\mu$. Using the definition $\delta_\mu = \omega_\mu - \omega_p - D_1\mu$, This allows us to re-write our eq. (2.1) Hamiltonian as

$$H_0 = \sum_\mu \left[\delta_\mu \hat{a}^\dagger_\mu \hat{a}_\mu + g_0(\hat{a}^{\dagger 2}_0 \hat{a}_\mu \hat{a}_{-\mu} + \text{h.c.})\right] + (A_p\hat{a}_0 + \text{h.c.})$$

One can see that as a result of the term $D_1\mu$ in $\hat{R}$, $D_1$ is eliminated from all terms in the Hamiltonian via the mode matching condition. The energy offset by $\omega_p$ removes the explicit time dependence from the pump drive.

## 2.2 Coupling to the bath: the input-output formalism

Here we present a derivation of the input-output relations for open quantum systems, a powerful technique to relate the change of the field scattered off a quantum system to the system itself [28, 29]. To describe the open system where the resonator modes experience loss, we allow our cavity modes to couple to a continuum of harmonic oscillators [30], which we call the bath. To see how the bath influences the Heisenberg equations, we start by considering the Hamiltonian of a single uncoupled cavity mode:

$$H = \omega_0 a^\dagger a + \int_{-\infty}^{\infty} \omega b^\dagger(\omega) b(\omega) d\omega + \int_{-\infty}^{\infty} [\gamma a^\dagger b(\omega) + \gamma^* b^\dagger(\omega) a] d\omega \tag{2.4}$$

where $\omega_0$ is the resonant frequency of the cavity mode with annihilation operator $a$, $b(\omega)$ is the annihilation operator of the bath mode at frequency $\omega$, and $\gamma$ is the coupling rate between them. The relevant commutation relations are $[a, a^\dagger] = 1$, $[b(\omega), b(\omega)^\dagger] = \delta(\omega - \omega')$, and $[a, b(\omega)] = 0$. The Heisenberg equations of motion are:

$$\frac{da(t)}{dt} = -i[\hat{a}, \hat{H}] = -i\omega_0 a(t) - i\gamma \int_{-\infty}^{\infty} b(\omega, t) d\omega$$
$$\frac{db(\omega, t)}{dt} = -i[\hat{b}(\omega), \hat{H}] = -i\omega b(\omega, t) - i\gamma^* a(t)$$

Integrating the second equation, we obtain:

$$b(\omega, t) = b(\omega, 0)e^{-i\omega t} - i\gamma^* \int_0^t a(\tau) e^{-i\omega(t-\tau)} d\tau \tag{2.5}$$

We can then solve the second term of the first equation

$$\int_{-\infty}^{\infty} b(\omega, t) d\omega = \int_{-\infty}^{\infty} b(\omega, 0) e^{-i\omega t} d\omega - \frac{i\gamma^*}{2} a(t)$$

where we have used

$$\int_{-\infty}^{\infty} e^{-i\omega(t-\tau)} d\omega = 2\pi\delta(t - \tau)$$

$$\int_0^t 2\pi a(\tau)\delta(t-\tau)d\tau = \pi a(t)$$

We can define the input operator

$$b_{in}(t) = \frac{1}{2\pi}\int_{-\infty}^{\infty} b_0(\omega)e^{-i\omega t}d\omega$$

which depends entirely on the state of the bath at $t = 0$. We arrive at the following equation of motion for the cavity operator:

$$\frac{da(t)}{dt} = -i\omega_0 a(t) - \pi|\gamma|^2 a(t) - i\sqrt{2\pi}\gamma b_{in}(t)$$

We can define $\kappa/2 = \pi|\gamma|^2$ as the amplitude decay rate of the cavity mode, and arrive at the final expression

$$\frac{da(t)}{dt} = -i\omega_0 a(t) - \frac{\kappa}{2}a(t) - i\sqrt{\kappa}b_{in}(t)$$

which highlights the difference in units between the cavity operator and the bath operator. This energy decay rate $\kappa$ is related to the quality factor via $Q = \omega_0/\kappa$, where $\kappa$ would be measured as the full width half maximum of the Lorentzian resonance. While the emergence of the term $-\kappa a(t)/2$ is identical to the classical coupled mode equations, the term $b_{in}(t)$ is not present in the classical picture: it represents the Langevin noise operator, necessary for the Heisenberg equations to be consistent with a unitary evolution under the system Hamiltonian. This term describes the impact of bath mode vacuum fluctuations on the dynamics of the cavity.

## 2.3 Linearization

To include the coupling to the bath, our full Hamiltonian is written

$$H = H_0 + H_{\text{bath}} + V$$

where

$$H_{\text{bath}} = \sum_\mu \int \omega \hat{b}_\mu^\dagger(\omega)\hat{b}_\mu(\omega)d\omega \tag{2.6}$$

with a bath-coupling Hamiltonian

$$V = \sum_\mu \sqrt{\frac{\kappa_\mu}{2\pi}}\int \hat{a}_\mu^\dagger \hat{b}_\mu(\omega)d\omega \tag{2.7}$$

where $\kappa_\mu$ is the total loss rate for cavity mode $\mu$. Note that here we have written coupling to a single bath, but in realistic systems at least two baths must be considered (waveguide coupling and free-space losses, Chapter 4).

Equation 2.1 is fourth-order and would render cubic operator evolution equations. If, instead, the eq. 2.1 were to be transformed into a quadratic one, it would render a linear system of equations. Fortuitously, we can perform this transformation for a Kerr system where the dominant quantum effects comprise interaction of two strong pump field photons with two quantum modes. This is the crux of linearization. To linearize a system, we write a formal separation of the optical state into the mean field solution (assumed to be a coherent state) and the quantum fluctuations: $\hat{a}_\mu(t) \to A_\mu(t) + \hat{a}_\mu(t)$, where $A_\mu(t)$ is the complex amplitude of the coherent state inside the cavity. We only consider quantum fluctuation terms which are quadratic in the strong mean-field of the pump

$$\begin{aligned}\frac{d\hat{a}_\mu(t)}{dt} =& \left[ -i(\delta_\mu - 2g_0|A_0|^2) - \frac{\kappa_\mu}{2} \right] \hat{a}_\mu(t) \\ &+ ig_0 A_0^2 \hat{a}^\dagger_{-\mu}(t) - \sqrt{\kappa_\mu}\hat{b}_{\mathrm{in},\mu}(t).\end{aligned}$$

This example illustrates how a system of two modes $(\mu, -\mu)$ driven by a coherently-pumped mode $\mu = 0$ has been transformed into a two-mode system by eliminating the pump mode from the quantum space. As will become important in the next chapter, we are now free to solve for the classical field $A_0$ using the classical coupled mode equation

$$\frac{dA_0(t)}{dt} = \left[ -i(\delta_p - g_0|A_0|^2) - \frac{\kappa_0}{2} \right] A_0(t) + A_p,$$

thus tying together classical and quantum pictures.

## 2.4 Multimode input-output equations

So far we have considered only two (*i.e.*, signal, idler) modes pumped by a single coherent pump. We extend the treatment to a general multimode system as follows. Each bath-cavity mode pair has an associated input-output relation:

$$\hat{b}_{\mathrm{out},\mu}(t) = \hat{b}_{\mathrm{in},\mu}(t) - i\sqrt{\kappa_\mu}\hat{a}_\mu(t) \tag{2.8}$$

We define the following $2n$-dimensional vectors describing $n$ quantum modes in the frequency domain:

$$\bar{a}(\omega) = \begin{bmatrix} \hat{a}_1(\omega) \\ \vdots \\ \hat{a}_n(\omega) \\ \hat{a}_1^\dagger(-\omega) \\ \vdots \\ \hat{a}_n^\dagger(-\omega) \end{bmatrix} \qquad \bar{b}_{\text{in}}(\omega) = \begin{bmatrix} \hat{b}_{\text{in},1}(\omega) \\ \vdots \\ \hat{b}_{\text{in},n}(\omega) \\ \hat{b}_{\text{in},1}^\dagger(-\omega) \\ \vdots \\ \hat{b}_{\text{in},n}^\dagger(-\omega) \end{bmatrix} \qquad \bar{b}_{\text{out}}(\omega) = \begin{bmatrix} \hat{b}_{\text{out},1}(\omega) \\ \vdots \\ \hat{b}_{\text{out},n}(\omega) \\ \hat{b}_{\text{out},1}^\dagger(-\omega) \\ \vdots \\ \hat{b}_{\text{out},n}^\dagger(-\omega) \end{bmatrix} \tag{2.9}$$

We can define a matrix $N(\omega)$ from our coupled mode equations relating the output fluctuations to the input fluctuations:

$$\bar{b}_{\text{out}}(\omega) = N(\omega)\bar{b}_{\text{in}}(\omega) \tag{2.10}$$

which can also be written explicitly as

$$\hat{b}_{\text{out},\mu}(\omega) = \sum_{k=1}^{n} \Big[ N_{\mu,k}(\omega)\hat{b}_{\text{in},k}(\omega) + N_{\mu,k+n}(\omega)\hat{b}_{\text{in},k}^\dagger(-\omega) \Big]$$

## 2.5 Photon correlations below threshold

Although throughout most of this thesis we will be relying on numerical methods to solve general multimode systems, we begin with a symmetric Hamiltonian of a two-mode system to obtain some analytic results which will provide insight into the full system. Here, we can derive simple analytic expressions for expectation values of the photon correlations in the signal-idler pair generation process. We only consider interactions between pairs of modes $(-\mu, +\mu)$ centered around the pump. For this analysis, we choose $D_1 = (\omega_+ - \omega_-)/2\mu$ for which $\delta_+ = \delta_- = \delta$.

$$\hat{H}_0 = \delta(\hat{a}_-^\dagger \hat{a}_- + \hat{a}_+^\dagger \hat{a}_+) + ig(\hat{a}_- \hat{a}_+ - \hat{a}_-^\dagger \hat{a}_+^\dagger) \tag{2.11}$$

where $g = g_0|A_0|^2$, which includes both the Kerr coupling strength and the intensity in the pumped cavity mode. Assuming $\kappa_+ = \kappa_- = \kappa$, the Heisenberg equations read

$$\frac{d\hat{a}_\pm(t)}{dt} = -\left(i\delta + \frac{\kappa}{2}\right)\hat{a}_\pm(t) - g\hat{a}_\mp^\dagger(t) - i\sqrt{\kappa}\hat{b}_{\text{in},\pm}(t) \tag{2.12}$$

which gives us the following matrix $N(\omega)$ in Fourier space:

$$N(\omega) = \begin{pmatrix} 1+\frac{\kappa(\kappa/2-i(\delta+\omega))}{(g^2-\delta^2)-(\kappa/2-i\omega)^2} & 0 & 0 & \frac{g\kappa}{(g^2-\delta^2)-(\kappa/2-i\omega)^2} \\ 0 & 1+\frac{\kappa(\kappa/2-i(\delta+\omega))}{(g^2-\delta^2)-(\kappa/2-i\omega)^2} & \frac{g\kappa}{(g^2-\delta^2)-(\kappa/2-i\omega)^2} & 0 \\ 0 & \frac{g\kappa}{(g^2-\delta^2)-(\kappa/2-i\omega)^2} & 1+\frac{\kappa(\kappa/2+i(\delta-\omega))}{(g^2-\delta^2)-(\kappa/2-i\omega)^2} & 0 \\ \frac{g\kappa}{(g^2-\delta^2)-(\kappa/2-i\omega)^2} & 0 & 0 & 1+\frac{\kappa(\kappa/2+i(\delta-\omega))}{(g^2-\delta^2)-(\kappa/2-i\omega)^2} \end{pmatrix}$$

We can calculate the pair generation rate

$$R_{\pm}(t) = \left\langle \hat{b}^{\dagger}_{\mathrm{out},\pm}(t)\hat{b}_{\mathrm{out},\pm}(t) \right\rangle$$

where expectation value is taken with respect to the initial vacuum state. The expectation value is computed by applying the commutation relations

$$\left\langle \hat{b}_{\mathrm{in,i}}(\omega)\hat{b}^{\dagger}_{\mathrm{in,j}}(\omega') \right\rangle = \delta_{ij}\delta(\omega-\omega')$$

$$\left\langle \hat{b}^{\dagger}_{\mathrm{in,i}}(\omega)\hat{b}_{\mathrm{in,j}}(\omega') \right\rangle = 0$$

First we solve for a single application of the output operator:

$$\hat{b}_{\mathrm{out},+}(t)\left|0\right\rangle = \frac{1}{\sqrt{2\pi}}\int_{-\infty}^{\infty} e^{-i\omega t} d\omega N_{14}(\omega)\hat{b}^{\dagger}_{\mathrm{in},-}(-\omega)\left|0\right\rangle$$

Then the full expectation value is given by:

$$\begin{aligned} R_{+}(t) &= \frac{1}{2\pi}\int\int e^{-i(\omega-\nu)t} N^{*}_{14}(\nu)N_{14}(\omega)\left\langle \hat{b}_{\mathrm{in},-}(-\nu)\hat{b}^{\dagger}_{\mathrm{in},-}(-\omega)\right\rangle d\omega d\nu \\ &= \frac{1}{2\pi}\int_{-\infty}^{\infty} |N_{14}(\omega)|^2 d\omega \\ R_{-} &= \frac{1}{2\pi}\int_{-\infty}^{\infty} |N_{23}(\omega)|^2 d\omega \end{aligned}$$

where it is clear that $R_{+} = R_{-}$. This term integrates to

$$R_{\pm} = \frac{g^2(\kappa/2)}{(\kappa/2)^2 - (g^2-\delta^2)} \tag{2.13}$$

It is important to remember that we have tucked all detunings into the parameter $\delta$, including the cross-phase modulation induced by the pump which also depends on $g$. In the practical system where we assume higher order dispersion is negligible, $\delta = \delta_p + \frac{D_2}{2}\mu_{\pm}^2 - 2g$ where $\delta_p = \omega_0 - \omega_p$. The optical parametric oscillation threshold is reached when the generation rate goes to infinity, where linearization breaks down:

$$g^2 - \delta^2 = (\kappa/2)^2$$

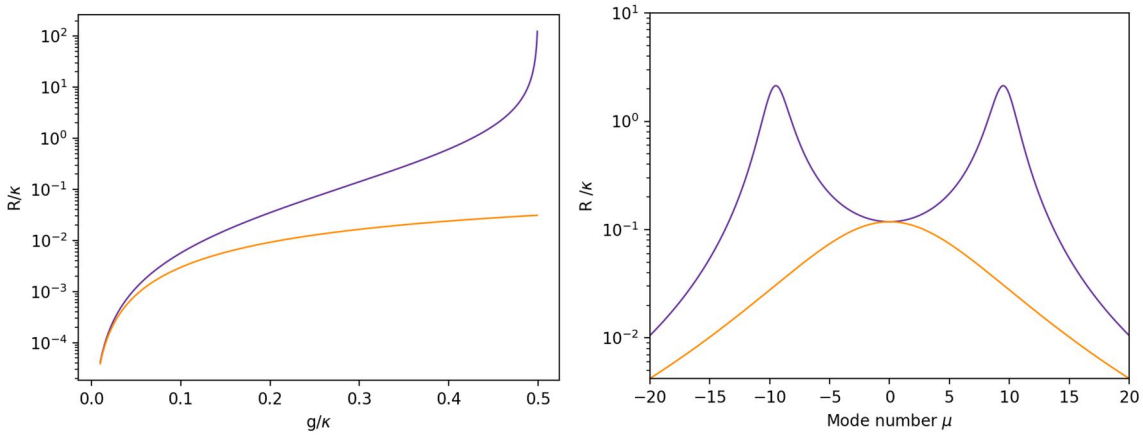


Figure 2.3: **Dependence of pair generation rate on the dispersion.** Left: Photon pair generation rate in the output waveguide, normalized to the cavity decay rate for anomalous dispersion (purple) and normal dispersion (orange). The modes with anomalous dispersion are able to reach the optical parametric oscillation threshold, whereas normal dispersion modes would not. Right: Below-threshold spectra (photon generation rate versus mode number) for anomalous and normal dispersion.

For the case $\delta = 0$, one can see that this occurs when the nonlinear gain becomes equal to the loss rate ($\kappa/2$). It is noteworthy, however, that for systems with detuning, the system can be below threshold even when $g$ exceeds $\kappa$, which has implications for squeezing. An example of a strongly detuned system is the multimode quantum state of a soliton crystal, described in Chapter 4.

With this analytic expression, we can examine the influence of dispersion on the below-threshold spectra of the comb. With respect to the point at which OPO threshold is reached, the role of dispersion is to balance the cross-phase modulation from the pump to hit the frequency matching condition of $\delta = 0$. If we perform this compensation by using $\delta = \frac{D_2}{2}\mu - 2g$ and set $D_2 = \pm 2\kappa$ and $\mu = 1$, we recover the left plot in Fig. 2.3 for varied $g$. In the case of anomalous dispersion ($D_2 > 0$), there exists a value of $g$ where the OPO threshold is reached. In contrast, for normal dispersion ($D_2 < 0$), the OPO threshold is never achieved as the detuning grows with pump strength, increasing $\delta$ despite increasing $g$. Thus, the pair generation rate does not go to infinity at $g/\kappa = \frac{1}{2}$. (Fig. 2.3, left panel).

However, absence of OPO threshold in the normal dispersion regime of course does not imply absence of a spontaneous-pair quantum comb. Figure 2.3 shows the pair generation rate versus mode number with fixed $g = 0.45\kappa$ and $D_2 = \pm 0.01\kappa$, for anomalous dispersion and normal dispersion of the same magnitude. In the normal dispersion comb, the strongest pair generation is centered close to the pump, whereas in the anomalous dispersion regime the mode pair with the largest photon rate is some distance away, at the mode number where the pump-induced detuning counteracts cold-cavity dispersion. As the comb approaches threshold, the pair generation in the mode which

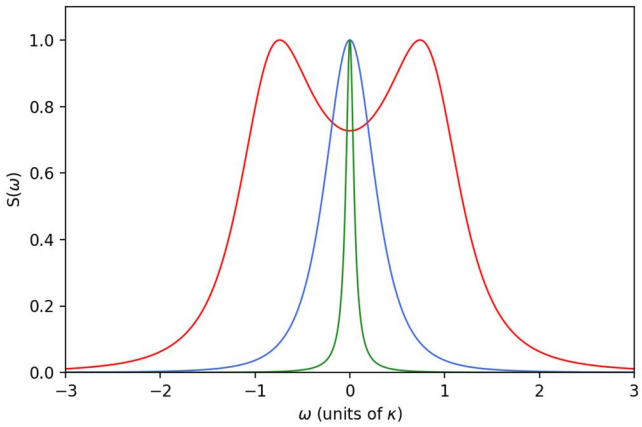


Figure 2.4: **Dependence of the spectral density on system rates.** Spectral density $S(\omega)$ normalized to the peak versus Fourier frequency for modes in three regimes: (i) drive far from threshold without significant detuning, $\kappa/2 > g > \delta$ (blue); (ii) drive approaching the threshold, $\kappa/2 \leftarrow g > \delta$ (green); and (iii) detuning larger than the drive, $\delta > g$ (red).

will reach OPO will grow asymptotically (in the case shown in Fig. 2.3, for mode pair $\pm 10$).

We can also find an analytic expression for the spectral lineshape of the photons and the dependence on the detuning parameter and proximity to threshold. The spectrum is given as the photon number spectral density versus Fourier frequency $\omega$ (detuning from the rotating frame)

$$S_{\pm}(\omega) = \left\langle \hat{b}^{\dagger}_{\mathrm{out},\pm}(\omega)\hat{b}_{\mathrm{out},\pm}(\omega) \right\rangle,$$

and is equal to $|N_{14}(\omega)|^2$:

$$S_{\pm}(\omega) = \left| \frac{g\kappa}{(g^2 - \delta^2) - (\kappa/2 - i\omega)^2} \right|^2$$

The photon pair spectra reveal three different regimes, as shown in Fig 2.4, where the spectra are normalized to the maximum value. We can define the parameter of effective gain $\lambda = \sqrt{g^2 - \delta^2}$ which can be real or imaginary. When $\kappa/2 \gg |\lambda|$, the lineshape is approximately a Lorentzian with a full width half maximum of $\kappa$. When $\lambda$ approaches $\kappa/2$, the linewidth narrows. If $\lambda$ is imaginary with magnitude greater than $\kappa/2$, then the lineshape is a split Lorentzian. As we will see in the analysis of two-photon correlations, these three regimes will also capture the different temporal coherence features of the light.

## 2.6 Two-photon correlation function

We now analyze the second-order coherence of the below-threshold quantum comb. The normalized two-photon correlation function is defined as:

$$g_{ij}^{(2)}(t+\tau,t) = \frac{G^{(2)}(t+\tau,t)}{\left\langle \hat{b}_{\mathrm{out,i}}^{\dagger}(t)\hat{b}_{\mathrm{out,i}}(t)\right\rangle \left\langle \hat{b}_{\mathrm{out,j}}^{\dagger}(t+\tau)\hat{b}_{\mathrm{out,j}}(t+\tau)\right\rangle} \tag{2.14}$$

where $G^{(2)}$ is the unnormalized second-order coherence of the field:

$$G^{(2)}(t+\tau,t) = \left\langle \hat{b}_{\mathrm{out,i}}^{\dagger}(t)\hat{b}_{\mathrm{out,j}}^{\dagger}(t+\tau)\hat{b}_{\mathrm{out,j}}(t+\tau)\hat{b}_{\mathrm{out,i}}(t)\right\rangle . \tag{2.15}$$

As before, the expectation value is taken with respect to the initial vacuum state. Notice that the normalization factor has already been calculated in the previous section.

To obtain the output operators in the time domain, we must relate them to the frequency-domain input bath operator:

$$\begin{aligned}\hat{b}_{\mathrm{out,i}}(t) &= \frac{1}{\sqrt{2\pi}}\int_{-\infty}^{\infty} d\omega e^{-i\omega t}\hat{b}_{\mathrm{out,i}}(\omega) \\ &= \frac{1}{\sqrt{2\pi}}\int_{-\infty}^{\infty} d\omega e^{-i\omega t}\sum_{k=1}^{n}\left(N_{ik}(\omega)\hat{b}_{\mathrm{in,k}}(\omega) + N_{i(k+n)}(\omega)\hat{b}_{\mathrm{in,k}}^{\dagger}(-\omega)\right)\end{aligned}$$

Using the commutation relations of the frequency-domain input bath operators

$$\left\langle \hat{b}_{\mathrm{in,i}}(\omega)\hat{b}_{\mathrm{in,j}}^{\dagger}(-\omega')\right\rangle = \delta_{ij}\delta(\omega+\omega') \qquad \left\langle \hat{b}_{\mathrm{in,i}}^{\dagger}(-\omega)\hat{b}_{\mathrm{in,j}}(\omega')\right\rangle = 0,$$

we derive the following general expression for the unnormalized correlation:

$$\begin{aligned}G^{(2)}(t+\tau,t) = \frac{1}{(2\pi)^2}\int\int d\omega d\nu \sum_{k,l}\Big[&|N_{j,(l+n)}(\omega)|^2|N_{i,(k+n)}(\nu)|^2 \\ &+N_{j,(k+n)}^{*}(\nu)N_{i,l}^{*}(-\nu)e^{i\nu\tau}\times N_{i,k}(\omega)N_{j,(k+n)}(-\omega)e^{-i\omega\tau} \\ &+N_{j,(l+n)}(\omega)N_{i,(l+n)}^{*}(\omega)e^{i\omega\tau}\times N_{i,(k+n)}(\nu)N_{j,(k+n)}^{*}(\nu)e^{-i\nu\tau}\Big]\end{aligned} \tag{2.16}$$

The first term has no time dependence, and is simply an integral over the frequency domain, which is identical to the normalization factor (the square of the generation rate). Note that this term guarantees that the normalized $g^{(2)}(\tau) \to 1$ at sufficiently long times where there is no longer temporal structure (as we will see in Chapter 3, this is no longer true for a time-dependent starting Hamiltonian). In the following sections, we evaluate the second and third terms to derive analytic expressions for the auto- and cross-correlation measurement across a below-threshold comb with monochromatic pump.

### 2.6.1 Autocorrelation derivation

Obtaining the temporal autocorrelation of one of the modes in the signal-idler mode-pair requires the evaluation of the following expression:

$$\frac{1}{2\pi}\int d\omega |N_{14}(\omega)|^2 e^{i\omega\tau}$$

To do so, we first rewrite the matrix element $N_{14}(\omega)$ in a convenient form:

$$\begin{aligned} N_{14}(\omega) &= \frac{g\kappa}{\lambda^2 - (\kappa/2 - i\omega)^2} \\ &= \frac{ig\kappa}{\lambda}\frac{i\lambda}{(i\lambda)^2 + (\kappa/2 - i\omega)^2} \end{aligned}$$

For this function, we have the following Fourier transform:

$$f(t) = \frac{ig\kappa}{\lambda}e^{-\frac{\kappa}{2}t}\sin(i\lambda t)\cdot u(t) = \frac{-g\kappa}{\lambda}e^{-\frac{\kappa}{2}t}\sinh(\lambda t)\cdot u(t)$$

where $u(t)$ is the Heaviside step function. Then the full Fourier transform is a convolution of Fourier transforms of individual Lorentzians:

$$\begin{aligned} &\int_{-\infty}^{\infty} dt \cdot e^{-\kappa/2\cdot(t-\tau)}\sinh\left(\lambda(t-\tau)\right)u(t-\tau)e^{-\kappa/2\cdot t}\sinh\left(\lambda t\right)u(t) \\ &\propto e^{-(\kappa/2)\tau}\left[\frac{\kappa}{2}\sinh(\lambda\tau) + \lambda\cosh(\lambda\tau)\right] \end{aligned}$$

The final step is to square the convolution and divide by the square of the normalization factor.

### 2.6.2 Cross-correlation derivation

To derive the expression for the cross-correlation, we evaluate the following expression:

$$G^{(2)}(\tau) = \left|\frac{1}{2\pi}\int d\omega e^{i\omega\tau}N_{22}(-\omega)N_{14}(\omega)\right|^2 + \left[\frac{1}{2\pi}\int d\omega |N_{14}(\omega)|^2\right]^2$$

Note that the second term is the normalization term, which we evaluated in Section 2.5. To evaluate the first term, it is convenient to rewrite the matrix element $N_{22}(-\omega)$ in three parts:

$$N_{22}(-\omega) = 1 + -k\frac{(\kappa/2 + i\omega)}{(i\lambda)^2 + (\kappa/2 + i\omega)^2} + \frac{\kappa\delta}{\lambda}\frac{(i\lambda)}{(i\lambda)^2 + (\kappa/2 + i\omega)^2}$$

Note this relation of the convolution:

$$F\{f\times g\} = F\{f\} * F\{g\}$$

where $*$ is a convolution in time, $\times$ is just multiplication, and $F\{f\}$ represents the Fourier transform of $f$. The Fourier transform of $N_{14}(\omega)$ was evaluated in the previous subsection. The Fourier transform of the second term of $N_{22}(-\omega)$ is:

$$f(t) = -\kappa e^{-\frac{\kappa}{2}t}\cos(i\lambda t)\cdot u(t) = -\kappa e^{-\frac{\kappa}{2}t}\cosh(\lambda t)\cdot u(t)$$

Then the convolution for this term is:

$$\frac{g(\kappa/2)}{((\kappa/2)^2-\lambda^2)}e^{-\frac{\kappa}{2}\tau}\Big(\kappa/2\cdot\cosh(\lambda\tau)+\lambda\cdot\sinh(\lambda\tau)\Big)$$

The third term uses the same structure of Fourier transform as $N_{14}(\omega)$:

$$f(t) = \frac{i\kappa\delta}{\lambda}e^{-\frac{\kappa}{2}t}\sinh(\lambda t)\cdot u(t)$$

The convolution for this term is:

$$\frac{g(\kappa/2)}{(\kappa/2)^2-\lambda^2}(-i\delta/\lambda)e^{-\frac{\kappa}{2}\tau}\Big(\kappa/2\cdot\sinh(\lambda\tau)+\lambda\cdot\cosh(\lambda\tau)\Big)$$

Then the sum of the three convolutions is:

$$\frac{g(\kappa/2)}{(\kappa/2)^2-\lambda^2}e^{-\frac{\kappa}{2}\tau}\Big[(\lambda-i\delta(\kappa/2)/\lambda)\sinh(\lambda\tau)+((\kappa/2)-i\delta)\cosh(\lambda\tau)\Big]$$

### 2.6.3 Auto- and cross-correlation: Final expressions

Recall the definition $\lambda = \sqrt{g^2-\delta^2}$. The final analytic expressions for the autocorrelation and cross-correlation are:

$$g^{(2)}_{++}(\tau) = 1+\frac{e^{-\kappa\tau}}{\lambda^2}\Big[\frac{\kappa}{2}\sinh(\lambda\tau)+\lambda\cosh(\lambda\tau)\Big]^2 \tag{2.17}$$

$$g^{(2)}_{+-}(\tau) = 1+\frac{e^{-\kappa\tau}}{g^2}\Big|\Big(\lambda-i\frac{\kappa}{2}\frac{\delta}{\lambda}\Big)\sinh(\lambda\tau)+\Big(\frac{\kappa}{2}-i\delta\Big)\cosh(\lambda\tau)\Big|^2 \tag{2.18}$$

and $g^{(2)}_{++}(\tau) = g^{(2)}_{--}(\tau)$, $g^{(2)}_{+-}(\tau) = g^{(2)}_{-+}(-\tau)$.

## 2.7 Experiment

In this section, we reproduce in experiment the analytic results we have derived above. We drive SiCOI microrings (Fig. 2.7) with a monochromatic pump around 1550 nm and measure the below-threshold spectrum and the two-photon correlations to compare to our predictions. Considerations for the choice of SiC as the nonlinear optical platform are described in Chapter 8, where classical

nonlinear experiments in SiC are presented.

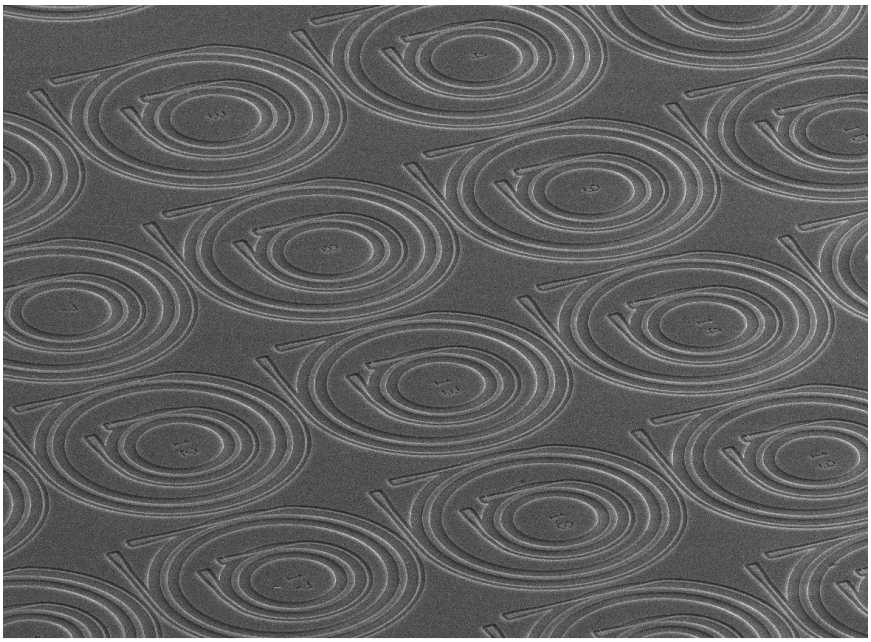

Figure 2.5: **Array of SiCOI microresonators used for experimental demonstrations in Chapters 2 and 3.** Scanning electron micrograph of silicon carbide-on-insulator microrings before encapsulation in SiO2. The large rings have a diameter of 100 um and a height of 520 nm. The bus waveguide, equipped with cross-polarized inverse-designed vertical couplers, wraps around the ring. The couplers are designed to be close together to accommodate the operation field of a cryogenic doublet (Section 9.1) used to obtain free-space access. A second smaller ring is fabricated inside each larger ring to maximize device density and sweep a larger parameter space in the waveguide width and bus waveguide coupling gap.

We generate Kerr frequency combs using microring resonators with a free spectral range (FSR) of 350 GHz, fabricated in 4H-SiCOI (see Chapter 5 and 8 for fabrication details). Broadband inverse-designed vertical couplers are used to couple light to and from the device[10]. The device is operated at 4 K to reduce the thermo-optic response [31], although traditional thermal management schemes (e.g., frequency tuning, power bumping, laser cooling, auxiliary mode pumping) may have been used instead to capture all states studied in this thesis. More information on the cryogenic operation and the dependence of system parameters on temperature can be found in Section 9.1. With intrinsic quality factors (Q) as high as $5.6 \times 10^6$, a low threshold OPO power requirement of 0.5 mW in the waveguide is achieved (Section 9.2).

The observation of the full optical spectrum of a Kerr frequency comb, including the above- and below-threshold processes, requires single-photon sensitivity and a high dynamic range. For this purpose, we designed a single-photon optical spectrum analyzer (SPOSA) using multipass grating monochromators and superconducting nanowire single-photon detectors (SNSPDs) (PhotonSpot,

Inc). The SPOSA has a broadband ($> 200$ nm) quantum efficiency of $\sim 20\%$, and close-in dynamic range of $> 140$ dB at $\pm 0.8$ nm. In the design of the single-photon optical spectrum analyzer (SPOSA), we focused on broadband operation in order to image all parts of the frequency comb, which extends beyond the operation range of standard fiber-based filtering components. For this reason, a free-space monochromator approach was chosen. Blazed gratings (600 grooves/mm) optimized for 1.5 µm operated in the Littrow configuration have $75 - 85\%$ efficiency across the range of operation (1300-1700 nm). In a single-pass monochromator, dynamic range is limited to $\sim 70$ dB by roughness-induced scattering from the grating surface. By operating the monochromator in a two-pass configuration, where the forward and return beams do not overlap on the grating, the dynamic range is doubled. To further increase the dynamic range, a second, single-pass monochromator can additionally be used. The double-pass monochromator configuration has dynamic range in excess of 180 dB and total peak efficiency as high as 55%. The superconducting nanowire single photon detectors (SNSPDs) are optimized for broadband operation with efficiency exceeding 80% from $1.0 - 1.6$ µm. The experimental setup is presented in Fig. 2.6.

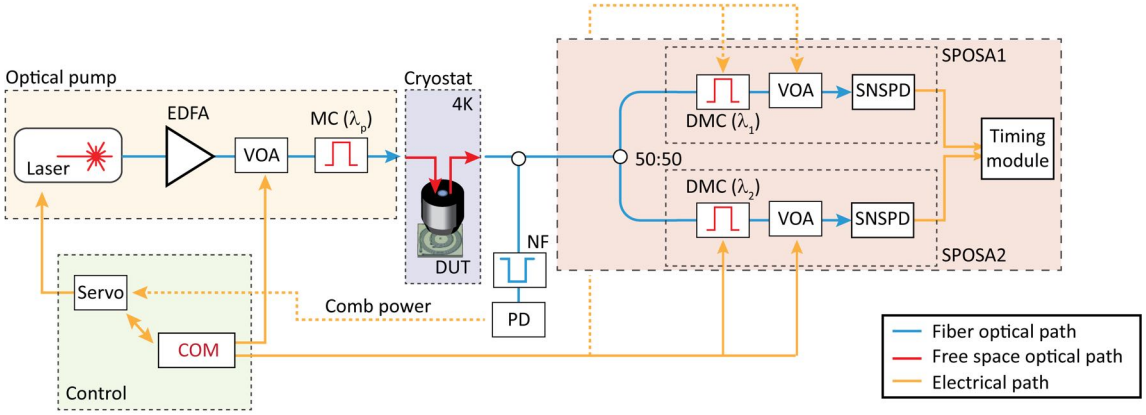


Figure 2.6: **Single-photon optical spectrum analyzer.** A silicon carbide microring resonator interfaced with inverse-designed vertical couplers[10] is mounted in a closed-cycle cryostat. Automated locking of a desired microcomb state is performed using active feedback by controlling the laser wavelength and power. A free-space tunable two-pass monochromator (MC) and double monochromator (DMC) serve as narrow band-pass filters with rejection of >130 dB and >180 dB, respectively. The dynamic range of the superconducting nanowire single photon detectors (SNSPDs) is extended from 60 dB to 180 dB via variable optical attenuators (VOA). A single SPOSA is used for spectroscopy and two SPOSAs are used for photon correlation measurements. Photon detection events are recorded with a timing module TimeTagger Ultra from Swabian Instruments.

In practice, the laser cannot be directly used to drive the resonators due to the substantial amplified spontaneous emission present in its spectrum, which would overwhelm the quantum comb signal. Furthermore, since the laser output is amplified with an erbium-doped fiber amplifier (EDFA), even noise is present due to substantial amplified spontaneous emission of the EDFA. To remove this

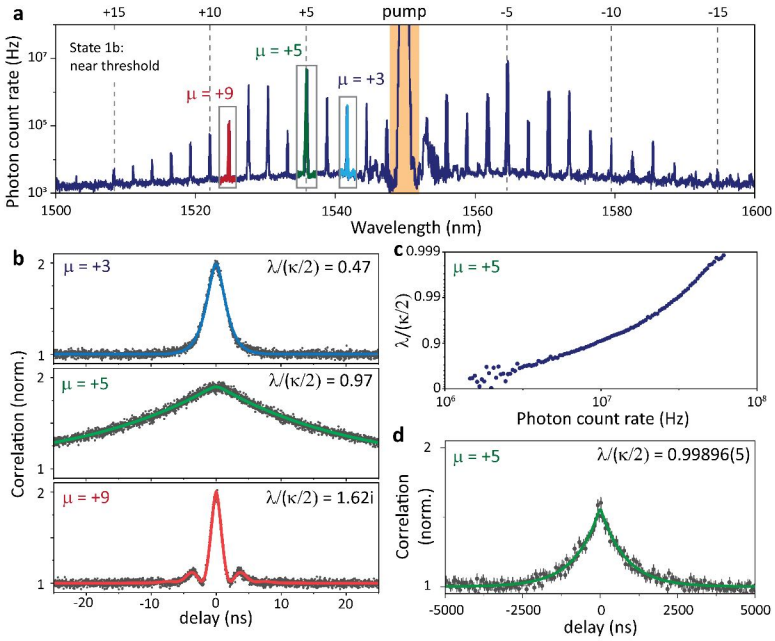


Figure 2.7: **Quantum coherence of parametric oscillation (a)** The near-threshold spectrum reproduced from Fig. 3.1a. Vertical dashed lines indicate the modes where the primary comb will form. **(b)** Measured $g^{(2)}_{\text{auto}}(\tau)$ on different modes shows the dispersion-dependent parametric gain variation throughout the comb. **(c)** Observation of asymptotic growth of coherence near the OPO threshold. The effective parametric gain $\lambda$, extracted from a numerical fit to Eq. 2.18 is plotted against the detected count rate on mode $\mu = +5$. **(d)** At the highest photon count rate, $g^{(2)}_{\text{auto}}(\tau)$ reveals coherence-broadening which corresponds to threshold proximity of 0.99896(5).

broadband noise, the pump is filtered with a free-space monochromator. We then tune the laser at a fixed power onto resonance from blue to red, operating the device close to the optical parametric oscillation threshold. Using the SPOSA, we record the below-threshold spectrum of Fig. 2.7a. We can compare the shape directly with the analytic expression plotted in Fig. 2.7b: Our resonator is designed for anomalous dispersion, and the peak of photon generation rate a few modes away from the pump, as expected. Unlike the theoretical shape, however, some modes are higher or lower than the expected smooth curve; this is likely due to avoided mode crossings. The microring is highly multimode and interactions between different families will perturb the dispersion and quality factors, which both influence the pair generation rate as seen in Eq. 2.13.

In our analysis of the spectral lineshape $S(\omega)$ of the below-threshold pairs, we identified three regimes of interest. The near-threshold comb (Fig. 2.7(a)) features all three regimes at different mode numbers. Recall the expression for the auto-correlation (Eq. 2.18)

$$g^{(2)}_{\text{auto}}(\tau) = 1 + \frac{e^{-\kappa\tau}}{\lambda^2}\left[\frac{\kappa}{2}\sinh(\lambda\tau) + \lambda\cosh(\lambda\tau)\right]^2$$

where $\lambda = \sqrt{g^2 - \delta^2}$ is the effective parametric gain, $g = g_0|A_0|^2$ is the mode coupling strength, and $\delta$ is the detuning. Here, two regimes are notable: when $\delta^2 > g^2$, $\lambda$ is imaginary which gives rise to oscillations in $g^{(2)}_{\text{auto}}(\tau)$, corresponding to the double-peaked photon spectrum for a strongly detuned parametric process[32, 33]; when $\lambda$ approaches $\kappa/2$, the $g^{(2)}_{\text{auto}}(\tau)$ coherence (decay time) increases asymptotically, reflecting the transition of the spontaneous FWM process into a stimulated FWM process (analogous to lasing). In a Kerr frequency comb close to but below the OPO threshold (Fig. 2.7a), both regimes can be observed simultaneously. We measure $g^{(2)}_{\text{auto}}(\tau)$ using two SNSPD detectors in a Hanbury Brown and Twiss configuration, and observe the dispersion-induced variation in $\lambda$ for different signal-idler pairs (Fig. 2.7b) [24]. Mode $\mu = +9$, far away from the pump, displays oscillations in $g^{(2)}_{\text{auto}}(\tau)$, signifying poor phase-matching. In contrast, mode $\mu = +5$ shows a substantial coherence increase, which correctly predicts that it will seed the formation of the primary comb. To observe the asymptotic coherence growth at threshold, we repeatedly sweep the pump laser detuning through the OPO threshold condition, while synchronously acquiring the photon count rates and two-photon correlations. Through the numerical fit to Eq. 2.18, $\lambda$ is extracted and plotted against the measured count rate (Fig. 2.7c). The maximum recorded coherence broadening exceeds the cavity coherence [29] by nearly three orders of magnitude (Fig. 2.7d), which indicates that the state is approaching the critical point at which the linearized model would break down [34, 33].

So far we have fit our data to our analytic model which leaves as free parameters the nonlinear coupling strength $g$ and detuning $\delta$. However, in the full model, these parameters are coupled. As the pump is tuned onto resonance, the intracavity amplitude grows; the modal detuning $\delta$ is dependent on both the pump detuning $\delta_p$ and this intracavity intensity of the pump via a cross-phase modulation frequency shift. The full model involves solving the LLE (eq. 1.2) for the classical mean-field of the pump and then solving for the driven quantum fluctuations of the input-output model.

The basic test case for the self-consistency of the joint LLE and input-output modelling is the OPO threshold condition: specifically, when the laser is tuned from blue to red to model the experiment, the asymptotic bandwidth narrowing in the below-threshold mode (as computed via input-output theory) and the formation of primary combs (as computed via the LLE) should happen simultaneously. We numerically reproduce the near-threshold behavior presented in Fig. 2.7. The result of the combined LLE and input-output theory simulation is presented in Fig. 2.8a. The modes $\mu = \pm 5$ indeed exit the regime of validity of the input-output formalism (when $Q_{\text{eff}}$ has positive real eigenvalues) at the onset of the LLE threshold. Although coherent comb light is present in other modes above threshold, the presented linearization failed only for the $\mu = \pm 5$ modes. A qualitative agreement between simulation and experimentally measured correlations (shown in Fig. 2.7b) is seen at the simulated detuning of $-9.3$ MHz, Fig. 2.8c.

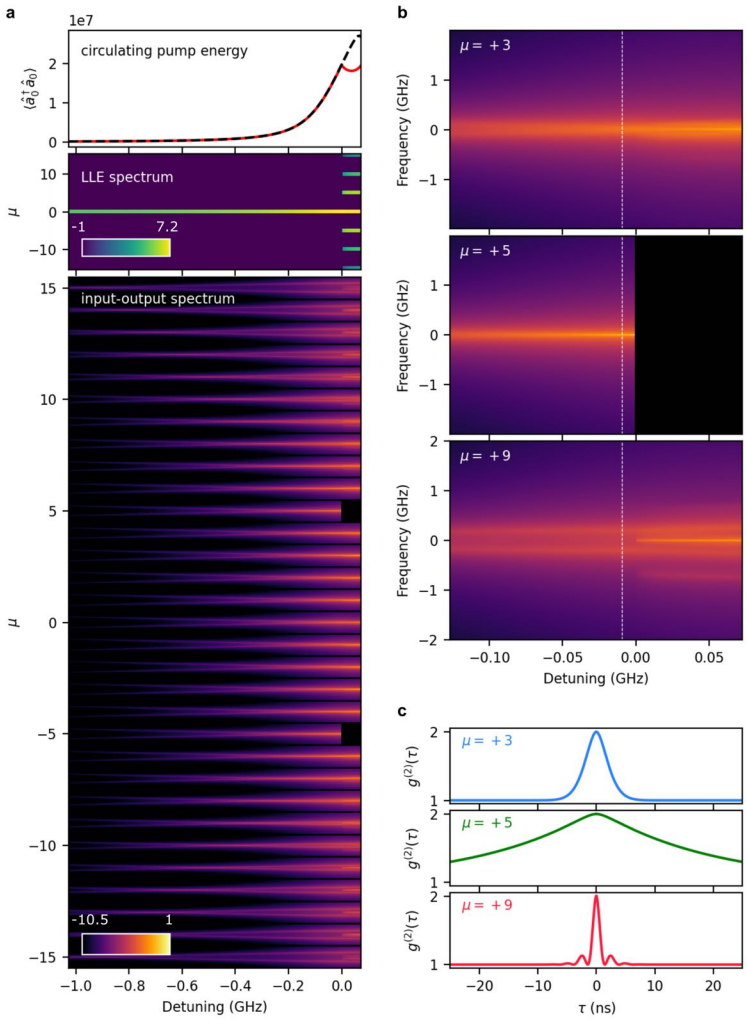


Figure 2.8: **Numerical analysis of OPO threshold a** *Top:* Dependence of the pump intensity in the microring (in units of photon number) on laser detuning. Detuning is given relative to the OPO threshold; a higher laser frequency corresponds to a more negative detuning with respect to the OPO condition. The LLE simulation (red) matches the analytic expression for the cavity mode in the presence of the Kerr nonlinear resonance shift (dashed black line) up to the threshold point, where the pump mode becomes depleted. *Middle:* Spectrum of the classical Kerr comb in the ring resonator, computed via the LLE, showing the formation of the 5-FSR primary comb. The scale represents $\log_{10}$(# of photons). *Bottom:* The photon spectrum of the below-threshold modes computed via input-output theory. For each mode, a spectral window of $\pm 2$ GHz is shown. At threshold, modes $\mu = \pm 5$ exit the regime of validity of the linearized model and are excluded from the input-output simulation. The scale represents photon number spectral density, $\log_{10}$(# of photons per Mrad/second). **b** Evolution of the spectrum of three select modes near threshold (same scale as *(b)*). Above threshold, the spectra exhibit additional features generated by the additional parametric processes driven by the primary comb lines. **c** Computed $g^{(2)}_{\text{auto}}(\tau)$ at a detuning of $-9.3$ MHz (indicated as a dashed line in *(b)*).

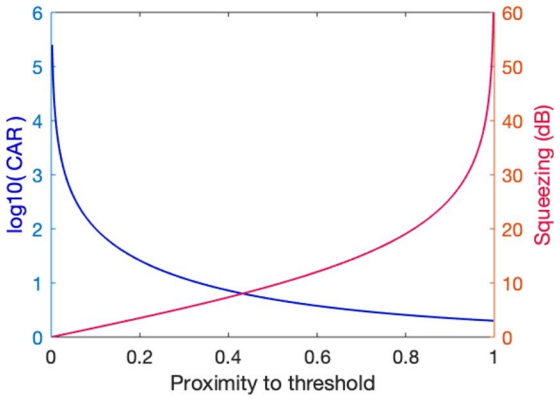


Figure 2.9: **Entanglement metrics.** Comparison of CAR and two-mode squeezing with respect to the proximity to the optical parametric oscillation threshold.

## 2.8 Entanglement metrics in below-threshold combs

It is natural to ask what is the optimal normalized drive strength $\tilde{A} = \sqrt{\kappa/(2g_0)}A_0$ to obtain maximum entanglement in the signal-idler pairs. The answer is that $\tilde{A}$ has to either approach unity (indicating infinite rate of photon generation) or otherwise be very small — depending on whether continuous variable or discrete variable entanglement is desired. The comparison is illustrated in Fig. 2.9, and described below.

In the discrete variable picture, entanglement is quantified as a strong correlation between photons detected in the signal and idler modes. However, since the generation of photon pairs is stochastic, it is possible for multiple photon-generation pair events to overlap in time, which degrades the correlation. The correlation strength is quantified by the coincidences-to-accidental ratio (CAR). Figure 2.10a shows an experimental measurement of the CAR via two-photon cross-correlation between a pair of modes. In the limit of weak drive, two-photon-pair events are dominant in degrading the CAR (appearing as "accidental" detection), and thus CAR is inversely proportional to the photon-pair generation rate, *i.e.* $\propto |\tilde{A}|^4$. It is worth noting that this sets a fundamental limit on the quality of discrete-variable entanglement, and any sources of noise photons will manifest as additional reduction in CAR. In practice, one must balance the drive strength to be weak enough that multi-photon events is not the dominant source of infidelity, but strong enough to achieve sufficiently-high rate of photon generation to be experimentally useful.

In the continuous variable regime, the situation is practically the opposite. Here, the entanglement manifests as the modification of the quadrature uncertainties of the signal-idler modes[35]: The squeezing of the uncertainty along one of the field quadratures is the entanglement resource, and is precisely the manifestation of temporal overlap of multiple signal idler photon pairs in the output field. This can be seen by considering that the maximally-entangled continuous variable two-mode

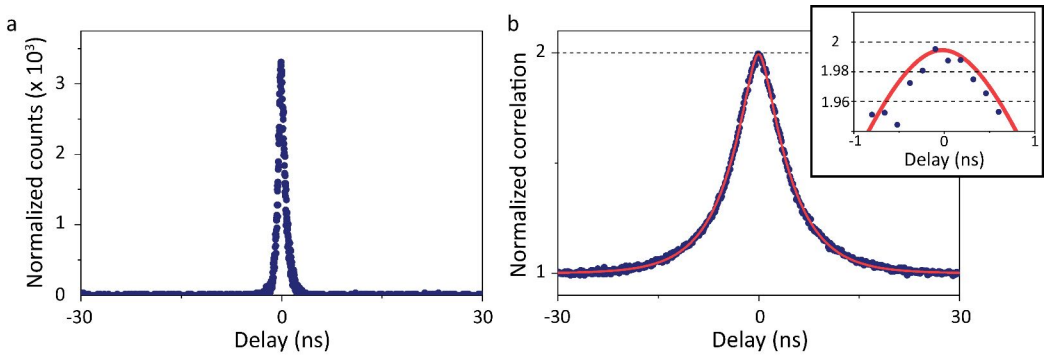


Figure 2.10: **CAR from cross correlation measurement.** Left: Cross-correlation measurement of a signal-idler pair far from threshold, where the trace is normalized to $g^{(2)}(\tau \to \infty) = 1$. The CAR is measured to be above $3 \times 10^3$. Note that the temporal lineshape is asymmetric around zero. This reflects slightly different decay rates for the two modes. Right: Autocorrelation of a single mode. This lineshape is always symmetric around zero. The proximity of the peak to $g^{(2)}(0) = 2$ reflects high single-mode purity of the measured photons. Parasitic photon sources such as pump leakage will degrade the correlation peak below the prediction for thermal statistics.

squeezed state, (analogous to the bipartite entangled Bell state in discrete variables) is the equal superposition of all signal-idler Fock states $\sum_{n=0}^{\infty} |n\rangle_s |n\rangle_i$, corresponding to infinitely-squeezed vacuum. This state is unnormalizable, containing infinite photons, and one approaches this ideal state asymptotically as $\tilde{A} \to 1$. Formalism for extracting the quadrature squeezing level of an arbitrary quadratic system is discussed extensively in Chapter 4.

Discrete variable signal-idler correlations are typically characterized using time-resolved photon detectors, whereas in the strong-drive, continuous variable regime, measurement of photon quadrature squeezing is done via a local oscillator or phase-sensitive amplification measurement. However, photon correlations can also provide valuable information about two-mode states in the strong-drive limit. In the correlation measurement, the squeezing manifests as a broadening of the coherence of spontaneously generated photons. Unlike quadrature squeezing, the correlation function is invariant to photon losses. This effect is the same in both three and four-wave mixing. As $\tilde{A} \to 1$, the fragility of the squeezed state grows asymptotically, but the correlation function is preserved. Monitoring the photon statistics of a signal-idler mode pair with threshold has this way enabled the observation of the state corresponding to $\tilde{A} = 0.99896$ (Section 2.7), which would correspond to squeezing beyond 30 dB if all the light generated was losslessly collected into a single optical mode (in practice, system losses will degrade the squeezing). The correspondence of photon correlation features to squeezed states will be discussed in Chapter 4.

## 2.9 Going above threshold

We have described the evolution of coherence and quadrature squeezing as the signal-idler mode pair approaches the optical parametric threshold. A natural question to ask is: what happens when one goes past the threshold? Or, even before OPO is reached, what happens when the rate of photon generation into the squeezed mode is so high (approaching the theoretical infinitely squeezed, infinitely energetic mode) that photon loss from the pump, so far assumed negligible (undepleted pump approximation), becomes significant? This regime is the breakdown of linearization [34, 36], where now we need to consider the effect of the quantum field on the coherent pump field, rather than assume it unperturbed by below-threshold processes. Pump depletion may be accounted for by employing a photon-number-conserving nonlinear Gaussian model, where the Gaussian moments of the classical mean-field and the quantum state are numerically solved together [37]. This is still an approximation of the full state.

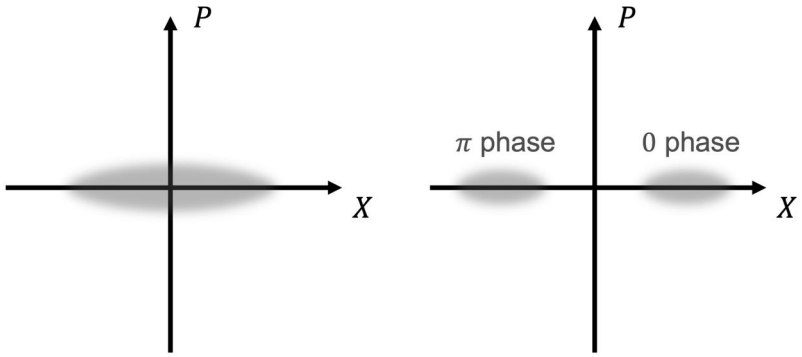


Figure 2.11: **Phase binarization at threshold.** Left: Pictorial representation of a degenerate squeezed state below the OPO threshold. Right: Degenerate squeezed state after reaching the OPO threshold. The state becomes displaced from the origin and chooses one of two phases relative to the pump: in-phase or out-of-phase.

In practice, we know that once the threshold is exceeded and OPO begins, the state ceases to be squeezed vacuum and becomes more similar to a coherent state. In phase space, this is visualized as the displacement of the squeezed state from the origin (Fig. 3). In a system where the nonlinearity and the loss rate are comparable ($g_0/\kappa \approx 1$), a cat state (coherent state superposition) forms along the squeezing quadrature axis [38]. Via strong light-matter interaction, cat states have been prepared using microwave photons in circuit quantum electrodynamics (QED) [39, 40] and Rydberg atoms in cavity QED [41]. However, in Kerr systems the nonlinear coupling rate is often much weaker by multiple orders of magnitude, even in high-confinement photonic resonators. The effect of the large relative loss rate is that the rate of destruction of quantum coherence by dissipation exceeds the rate of creation of quantum coherence by the two-mode interaction: the superposition state is replaced by a classical mixture of coherent states of opposite phase. This effect has been

used to build coherent Ising machines [42, 43]: spins are represented with above-threshold binary phases of degenerate optical parametric oscillators. Moreover, after pumping the system through its threshold, the optical parametric oscillator remains squeezed. Intensity difference squeezing in the above-threshold signal-idler beams has been measured using Kerr microrings as the source [44].

There is another interest in studying the above-threshold states: coherent, phase-locked pumps may be generated in-situ to drive quantum fluctuations in other modes. Once a pair of symmetric modes goes above the OPO threshold, the coherent pump is a comb: the connectivity is no longer pairwise but comprises multimode subgroups [45, 46] depending on the mode number of the first mode to hit the threshold. In the Kerr system, as we will see in Chapters 3 and 4, the mean field of modes which go above-threshold may directly drive pair generation and "lattice hopping" across other modes.

# Chapter 3

# Quantum correlations in soliton crystal microcombs

In the last chapter, we focused on the below-threshold quantum comb generated via a monochromatic pump injected into a Kerr ring resonator. This allowed us to introduce relevant multimode formalism for modeling the characteristics of the quantum fluctuations. We also saw how to interface the linearized model with robust measurable quantities, namely two-photon correlations, and described the experimental setup we have used to measure them.

In this Chapter, we will extend the same treatment to Kerr combs, which follow from the single-pump state after it reaches its optical parametric oscillation threshold. We will see how the stimulated multi-color Kerr comb light adds complexity to the Hamiltonian by extending the modal connectivity from pair-wise coupling of signal-idler modes to multi-mode interactions dictated by the mode-number matching condition. For certain Kerr combs, all-to-all coupling can be generated. Using the same experimental setup described in the previous Chapter, we experimentally demonstrate quantum combs generated by above-threshold Kerr combs, and validate the theoretical predictions.

## 3.1 Below-threshold spectra of Kerr combs

The below-threshold signal-idler comb studied in Chapter 2 (Fig. 2.7) is the first state in the stages of formation of a dissipative Kerr soliton (DKS). The most common method to experimentally generate DKS states is via monotonic red-tuning of the pump laser onto resonance with a microring mode. The resonator may enter the DKS state after several stages of Kerr combs (primary, secondary, chaos). While the strong mean field of these formation stages is routinely measured with commercial optical spectrum analyzers [24], the full states (including weak quantum light) have not been observed

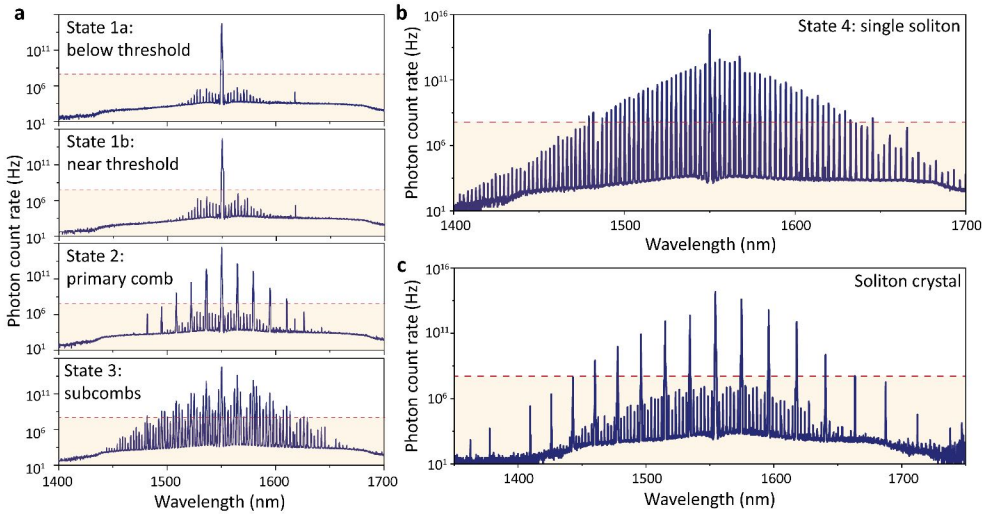


Figure 3.1: **Single-photon spectroscopy of optical microcombs (a)** Stages of frequency comb formation observed on the single-photon optical spectrum analyzer (SPOSA). Dashed line indicates noise floor of a commercial optical spectrum analyzer (-80 dBm). **(b)** The single soliton state. **(c)** A 7-FSR soliton crystal state, observed in a different device.

due to limitations of instrumental sensitivity. Here, we use the SPOSA to measure the below- and above-threshold components of these different stages simultaneously.

As we red-tune the pump further onto resonance, different states emerge and can be stabilized using a servo lock on the comb or pump power. The measured SPOSA spectra for these states are shown in Figure 3.1. The top left panels State 1a and State 1b show the signal-idler comb that we measured in Chapter 2, further from the threshold and close to the threshold, respectively. We see a dramatic increase in the photon rate for modes close to their OPO threshold.

The third panel shows the primary comb (state 2). This is the state which forms directly after the first pair of modes at $\pm\mu_{th}$ hits its OPO threshold. Those modes transition from spontaneous emission to stimulated emission; stimulated four-wave mixing fills out the comb in the modes which are integer multiples of the mode spacing $|\mu_{th}|$ — In the previous section, modes $\pm 5$ exhibited the drastic coherence broadening and increase in counts. A 5-FSR primary comb emerges after the threshold is reached. Note that the below-threshold spectrum has taken on a different shape due to the contribution of multimode drive. Figure 3.2 shows the dynamics of the below-threshold comb in the formation of primary comb, illustrating the different effect on the modes that are and are not multiples of the mode numbers that seed OPO.

As more power is injected into the primary comb, it will drive pair generation across the below-threshold comb, where the connectivity is dictated by the mode number matching condition. With enough power in the primary comb, a second OPO threshold can be reached. If the threshold is

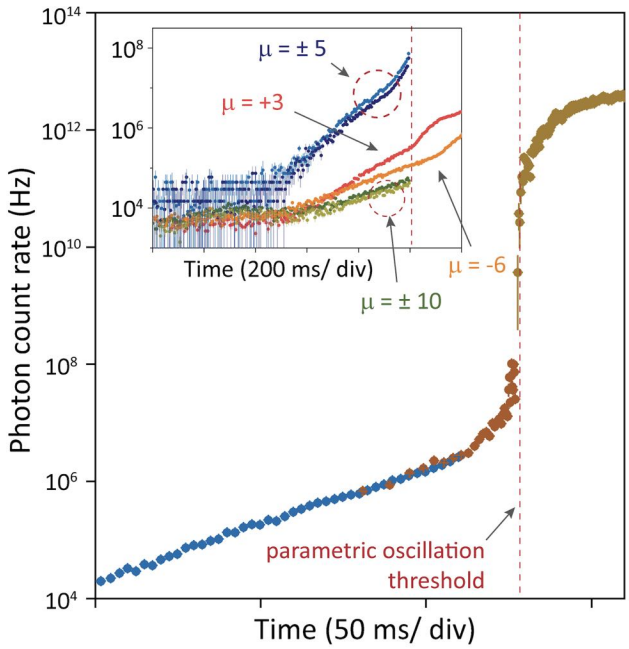


Figure 3.2: **Temporal dynamics in the birth of the primary comb.** Photon detection rate on mode 5 as the pump laser is detuned through threshold. Colors represent three detectors with different level of attenuation to capture the full dynamic range of the signal. Exponential growth away from threshold is replaced by asymptotic growth, followed by a plateau above threshold. Inset: evolution of several modes in the comb. Modes $-6$ and $+3$ do not show a discontinuity at the primary comb formation, but are still affected due to the presence of multiple pumps after OPO threshold. Mode $+10$, which is populated by stimulated FWM after OPO onset, reaches saturation (detector signal goes to 0) practically instantaneously despite low photon rate before OPO. Modes $\pm 5$ are reproduced in the inset for contrast, displaying super-exponential growth that continuously transitions to OPO.

reached in a mode which is one FSR from a primary comb mode, then the full above-threshold comb can become filled out, forming a secondary comb and subcombs (State 3). As we will see in a following section, the stimulated light and spontaneous light can exist at comparable levels within the same mode; as more power is injected into the subcombs, stimulated light will come to dominate.

Finally, the secondary comb may transition into a chaotic state that may collapse into a single bright soliton step. The spectrum of the bright soliton is shown in Fig. 3.1(b), corresponding to a single pulse traveling around the ring. A time-domain measurement of power in the output waveguide would reveal a pulse train at the repetition rate of the comb spacing. The capture of the soliton state is highly dependent on the input pump power. With too little input power, only modulation instability is observed; too much input power and a multi-soliton state (multiple pulses) will be generated. Note that in this demonstration we access the states via adiabatic pump tuning, enabled by working at cryogenic temperatures to significantly reduce the thermo-optic coefficient

of SiC. As can be seen in Fig. 3.1(b), the $\text{sech}^2$ soliton envelope is seen to persist at the tails of the DKS, in modes with very low photon number $\left\langle a_j^\dagger a_j \right\rangle < 10^{-3}$ (corresponding to a photon count rate of $< 1$ kHz). The quantum fluctuations generated in the DKS state and responsible for its quantum-limited timing jitter [47, 9] are obscured in the single-soliton spectrum as the stimulated four-wave mixing (mean-field amplitudes) dominates.

By probing the photon auto-correlation of individual teeth of the soliton, we have observed that they have the $g^{(2)} = 1$ for all $t$, same as a coherent state. Light generated via stimulated four-wave mixing will have the same photon statistics as the pump, and the laser is modeled as a coherent state. We would like to measure spontaneously generated photon pairs isolated from the strong mean-field state. A perfect soliton crystal [48, 49] (henceforth referred to as a soliton crystal) reveals these quantum fluctuations (Fig. 3.1c). Here we measure a 7-FSR soliton crystal, where strong mean-field light only occupies every 7th mode: this corresponds to seven pulses traveling around the ring with equidistant spacing.

Soliton crystals can form due to perturbations in the dispersion and quality factors of the modes, often naturally arising due to avoided mode crossings with other mode families in multimode resonators. For example, an $N$-FSR soliton crystal may be numerically accessed in the Lugiato-Lefever equation by shifting the frequency of the $N$-th mode from the pump, inducing a perturbation in the otherwise symmetric anomalous dispersion. The perturbation can induce localized enhancement of conversion efficiency in the $\mu \pm N$ mode. The pump and this strong line interfere, creating a bichromatic background wave in the resonator which stabilizes individual solitons into a perfectly-spaced soliton crystal. The numeric modeling of soliton crystal formation will be discussed in more detail in a subsequent section.

## 3.2 Equations of motion in presence of multiple pumps

Before we begin to explore the experimental correlations in these multimode Kerr combs, we will first extend the linearization approach from the first Chapter to the case of multimode strong mean field. We consider the general system Hamiltonian for four-wave mixing between cavity modes with coherent drive of the pump mode, $\mu = 0$:

$$\hat{H}_{\text{sys}} = \sum_{\mu} \omega_\mu \hat{a}_\mu^\dagger \hat{a}_\mu - \frac{1}{2} g_0 \sum_{\mu,\nu,j,k} \delta[\mu + \nu - j - k] \hat{a}_\mu^\dagger \hat{a}_\nu^\dagger \hat{a}_j \hat{a}_k + \alpha_0 (\hat{a}_0 e^{i\omega_p t} + \hat{a}_0^\dagger e^{-i\omega_p t}) \tag{3.1}$$

where $\delta[\mu + \nu - j - k]$ is the Kronecker delta which enforces the four-wave mixing mode-matching condition. Here, $\omega_\mu$ is the resonance frequency of cavity mode $\mu$ and $\omega_p$ is the frequency of the coherent pump driving the central mode. The nonlinear coupling coefficient

$$g_0 = \frac{\hbar \omega_p^2 c n_2}{n_0^2 V_{\text{eff}}}$$

represents the per photon frequency shift of the cavity due to the third-order nonlinearity of the cavity: $\hbar$ is the reduced Planck's constant, $n_2$ is the nonlinear refractive index, $n_0$ is the material index, and $V_{\text{eff}}$ is the effective mode volume of the resonator. The amplitude of the drive field is

$$\alpha_0 = \sqrt{\frac{\kappa_c P_{\text{wg}}}{\hbar\omega_p}}$$

where $\kappa_c$ is the coupling rate of the cavity to the input waveguide and $P_{\text{wg}}$ is the power in the input waveguide. To linearize the system, we write a formal separation of the optical state into the mean field solution (assumed to be a coherent state) and the quantum fluctuations: $\hat{a}_\mu(t) \rightarrow \alpha_\mu(t) + \hat{a}_\mu(t)$, where $\alpha_\mu(t)$ is the complex amplitude of the coherent state inside the cavity. Moving into the reference frame which removes explicit time dependence from the classical coupled mode equations[32], we apply a unitary transformation using $\hat{U}(t) = e^{i\hat{R}t}$ where $\hat{R} = \sum_\mu(\omega_p + D_1\mu)\hat{a}_\mu^\dagger\hat{a}_\mu$. We enter the rotating frame of an evenly-spaced frequency ruler, with spacing $D_1$, centered at the central pump mode. Defining $\delta_\mu = \omega_\mu - \omega_p - D_1\mu$, and keeping only quadratic terms, we arrive at:

$$\hat{H}_{\text{sys}} = \sum_\mu \delta_\mu \hat{a}_\mu^\dagger \hat{a}_\mu - \frac{g_0}{2}\sum_{\mu,\nu,j,k}\delta[\mu+\nu-j-k](\overbrace{A_\mu A_\nu \hat{a}_j^\dagger \hat{a}_k^\dagger}^{\text{spontaneous pair generation}} + \underbrace{A_k^* A_\nu \hat{a}_j^\dagger \hat{a}_\mu}_{\text{XPM \& Bragg scattering}} + \text{h.c.}) \tag{3.2}$$

where $A_\mu$ are the complex-valued field amplitudes, described using the Lugiato-Lefever equation [23].

Starting with the linearized Hamiltonian, we obtain the coupled-mode equations

$$\begin{aligned}\frac{d\hat{a}_\mu(t)}{dt} = &-\left(i\delta_\mu + \frac{\kappa_\mu}{2}\right)\hat{a}_\mu(t) \\ &+ ig_0\sum_{\nu,j,k}\delta[\mu+\nu-j-k]A_jA_k\hat{a}_\nu^\dagger(t) \\ &+ 2ig_0\sum_{\nu,j,k}\delta[\mu+j-\nu-k]A_j^*A_k\hat{a}_\nu(t) \\ &- \sqrt{\kappa_\mu}\hat{b}_{\text{in},\mu}(t)\end{aligned} \tag{3.3}$$

where $\kappa_\mu$ is the the total decay rate of mode $\mu$, $\delta_\mu$ is the detuning from the rotating frame (set by the group velocity of the soliton), and $\hat{b}_{\text{in},\mu}$ are the cavity bath operators. In equation 3.3, the first term accounts for the modal detunings (dispersion); the second term represents pair generation; the third term describes XPM and Bragg scattering; and the last term is the coupling to the bath. These processes are represented in Figure 3.3.

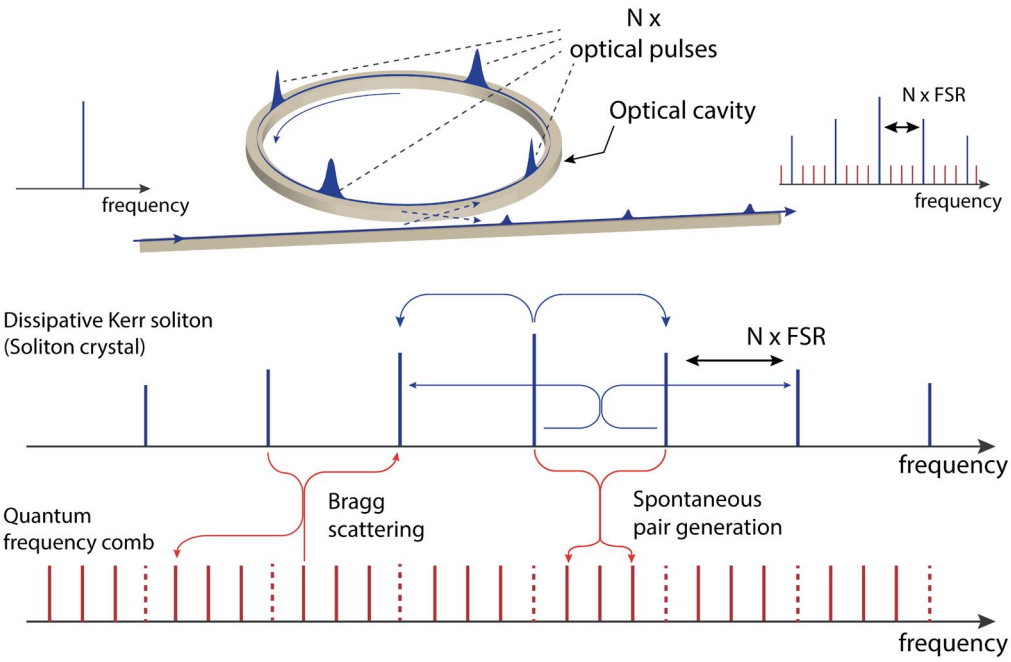


Figure 3.3: **Linearized model for quantum optical fields in a DKS state** A schematic depiction of a Kerr microresonator with a circulating perfect soliton crystal state. The full optical state is modeled as a coherent classical comb (blue) that drives the quantum comb (red) via spontaneous parametric processes.

## 3.3 Photon correlations in primary and secondary combs

In the linearized model of an above-threshold Kerr comb, a resonator mode may be occupied by both a coherent state and quantum fluctuations. In theory, the interference of the coherent state and the quantum fluctuations can be revealed through $g^{(2)}(\tau)$, but the intensity of the former is usually orders of magnitude greater (as can be seen in the spectra of the primary comb and the soliton crystal, Fig. 3.1), making the experimental observation difficult.

An exception can be found in the formation of secondary combs, where the amount of stimulated light can be controlled by the strength with which the secondary comb is driven (Fig. 3.4(a)). To isolate a state with this delicate balance, we characterize the quantum formation dynamics of secondary combs through second-order photon correlations, complementing earlier classical studies [24, 50]. We identify a device and pumping configuration where the first optical parametric oscillation threshold is formed at modes $\pm 8$ from the pump mode. We monitor the autocorrelation of mode $\mu = +4$.

In State 1 (Fig. 3.4(b)), before the threshold is reached, the autocorrelation follows the analytic lineshape derived in Chapter 1, with the coherence dictated by the lifetime of the resonator. The autocorrelation peaks at 2, reflecting the thermal statistics expected when measuring only one mode

of the signal-idler pair.

In State 2, the threshold is reached and the primary comb forms. Now the mode $\mu = +4$ is populated by two dominant spontaneous processes: (i) pair generation from the pump alone into modes $\mu = \pm 4$ via terms such as $A_0^2 \hat{a}_4^\dagger \hat{a}_{-4}^\dagger$; and (ii) degenerate pair generation into mode $\mu = +4$ via terms such as $A_0 A_8 \hat{a}_4^{\dagger 2}$. Recall that a cross correlation measurement between the two entangled modes of a signal-idler comb will have a two-photon correlation peak that may go far above $g^{(2)}(\tau = 0) = 2$. This bunching will also be observed now in the autocorrelation measured on mode $\mu = +4$ due to the degenerate pair generation. The Fourier transform (inset) captures the spectral bandwidth of the below-threshold light.

In State 3a, the primary comb has pumped a second OPO threshold and subcombs have formed. The second threshold process did not take place in the $\mu = +4$ mode, but stimulated four-wave mixing has transferred coherent light into the mode. Notably, at the onset of subcombs merging, the intensities of the (bichromatic) coherent state and the quantum optical fields become comparable, and the signature of their interference in two-photon correlations is readily observed (third panel of Fig. 3.4c, state 3a). The important feature of the correlation which distinguishes between the coherent and spontaneous light is the timescale: the coherence of the beatnote is much longer than the timescale of the resonator, corresponding to a much more narrow spectral peak. The Fourier transform of the auto-correlation shows three peaks, at 0, $\Delta/2$, and $\Delta$; they represent, respectively, the two-photon bunching of spontaneous pair generation, the interference of the quantum fluctuations with the bichromatic coherent state, and the coherent RF beat note [24, 50] of the coherent state. The details of the theory used to model the interference are presented below. As the subcombs continue to merge, the coherent light drowns out the spontaneous parametric processes, and the photon correlations correspond to the interference of two weak coherent sources [51].

The modeling of the interference in $g^{(2)}(\tau)$ of stimulated and spontaneous FWM presented in Figure 3.4 is explained below. The operator $\hat{b}_{\text{out}}(t)$ is:

$$\hat{b}_{\text{out}}(t) = \hat{b}_{\text{in}}(t) - i\sqrt{\kappa}[\alpha(t) + \hat{a}(t)],$$

or, in the frequency domain,

$$\hat{b}_{\text{out}}(\omega) = N(\omega)\hat{b}_{\text{in}}(\omega) - i\sqrt{\kappa}\alpha(\omega).$$

Since the coherent field in the mode is bichromatic,

$$\alpha(t) = A_{\text{coh},1} e^{-i\omega_1 t} + A_{\text{coh},2} e^{-i\omega_2 t}. \tag{3.4}$$

We note that in the presence of a bichromatic coherent state, there is a distinction between $g^{(2)}(\tau)$

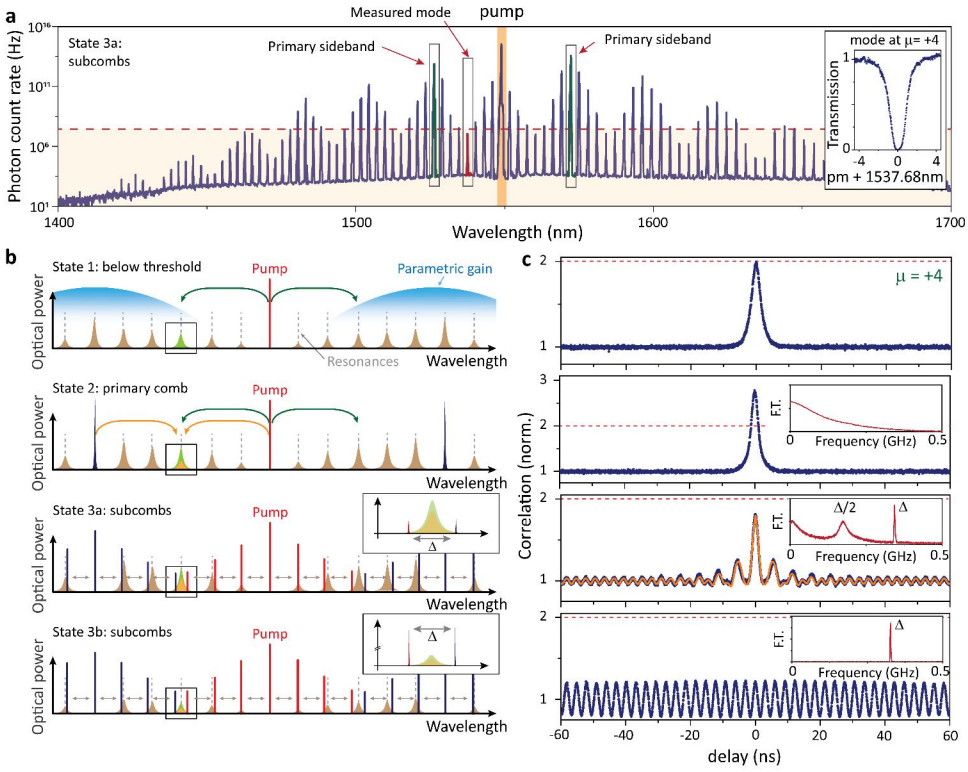


Figure 3.4: **Formation dynamics of secondary combs (a)** A SPOSA spectrum of a secondary comb state. **(b)** A graphical representation of the stages of secondary comb formation. **(c)** The auto-correlation is measured at mode $\mu = +4$ for each comb state. In state 1, only non-degenerate pair generation contributes to mode $\mu = +4$. In state 2, simultaneous degenerate and non-degenerate spontaneous pair generation is present. In state 3a, subcombs begin to merge and two-photon correlations reveal the interference of quantum fluctuations with the coherent state. The data are overlaid with the fit to input-output theory. In state 3b, the coherent state dominates and only the RF beat note is observed.

and the experimentally-measured correlations. Specifically, the measured correlations are the time-averaged two-photon coincidences $G^{(2)}(\tau) = \left\langle G^{(2)}(t+\tau,t)\right\rangle_t$, normalized to the mean value at $\tau \to \infty$:

$$g^{(2)}_{\mathrm{exp}}(\tau) = \frac{\int_{-\infty}^{\infty} G^{(2)}(t+\tau,t)\,\mathrm{d}t}{\lim_{T\to\infty}\int_{T}^{\infty}\int_{-\infty}^{\infty} G^{(2)}(t+\tau,t)\,\mathrm{d}t\,\mathrm{d}\tau} \tag{3.5}$$

To model the $g^{(2)}_{\mathrm{exp}}(\tau)$ presented in Fig. 3.4, we consider a system of three coherent drives $(A_{-8}, A_0, A_{+8})$, and four quantum modes $(\hat{a}_{-12}, \hat{a}_{-4}, \hat{a}_4, \hat{a}_{12})$. The effect of other coherent driving modes is assumed negligible, because their amplitude is much smaller. The fit parameters in the model are: 1) two pump amplitudes ($A_0$, and $A_{+8} = A_{-8}$); 2) two coherent state amplitudes ($A_{\mathrm{coh},1}$ and $A_{\mathrm{coh},2}$); 3)

two coherent state frequencies ($\omega_1$ and $\omega_2$); and 4) the pump laser detuning $\delta_p$.

## 3.4 Soliton crystal correlations

In this section, we proceed to measure the correlations within a soliton crystal and compare them to the prediction of the linearized model, where experimentally measured device parameters (dispersion, intrinsic and coupled Q-factors, pump power) are used as the input to the LLE solver, whose solution is in turn used as the driving terms of the input-output solver. In addition to soliton correlations, we also experimentally observe correlations within non-phase-locked combs (non-soliton states), which feature multiple tones at different teeth: we explore how these tones (which result in a time-dependent Hamiltonian) influence the correlations.

In a DKS state, the coherent comb is phase-locked and time-independent in the group-velocity reference frame, yielding a time-independent Hamiltonian for the quantum optical fields (Eq. 3.2). In contrast, a comb that is not phase-locked will produce a Hamiltonian with a time-dependent drive. To observe this effect in experiment, we consider a microring resonator which supports three distinct states with a 2-FSR spacing: one state is a 2-FSR soliton crystal (Fig. 3.5a); the others are non-natively spaced secondary combs [24] in the process of merging. These secondary combs are non-phase-locked states, which manifests in the frequency domain as polychromatic comb teeth. For each 2-FSR state, we measure $g^{(2)}(\tau) = \left\langle g^{(2)}(t, t+\tau) \right\rangle_t$ on mode $\mu = -15$ while simultaneously measuring the RF spectrum of mode $\mu = -6$ on a photodetector. Whereas the soliton crystal two-photon correlations are time-independent far from zero time delay, the correlations of a non-soliton state exhibit oscillations whose Fourier transform matches the RF spectrum measured on the photodetector. Such temporal dynamics may be modelled via Floquet theory [52]. We note that similar temporal oscillations in $g^{(2)}(\tau)$ have been observed in Floquet-driven two-level systems [53].

The soliton crystal state offers an excellent opportunity to experimentally verify the linearized model for the DKS state. The mean-field solution (complex amplitudes $A_m$ in Eq. 3.2) of the soliton crystal can be readily computed via the LLE; the below-threshold modes comprise the quantum fluctuations driven by the mean-field solution without any admixture of coherent light and, crucially, they are decoupled from the the quantum fluctuations of the above-threshold modes by the mode matching condition $\delta_{\mathrm{FWM}}$. We measure the correlations between all pairs of below-threshold modes of the 2-FSR soliton crystal, and compute the theoretically predicted second-order correlations matrix for the measured device parameters (Fig. 3.5c). We note that the only free parameter in the model is the pump laser detuning (within the soliton locking range). The agreement of the model with the experiment suggests that the quadratic Hamiltonian of the linearized model is indeed appropriate for describing the photon statistics of the quantum optical field generated in the below-threshold modes of a DKS state.

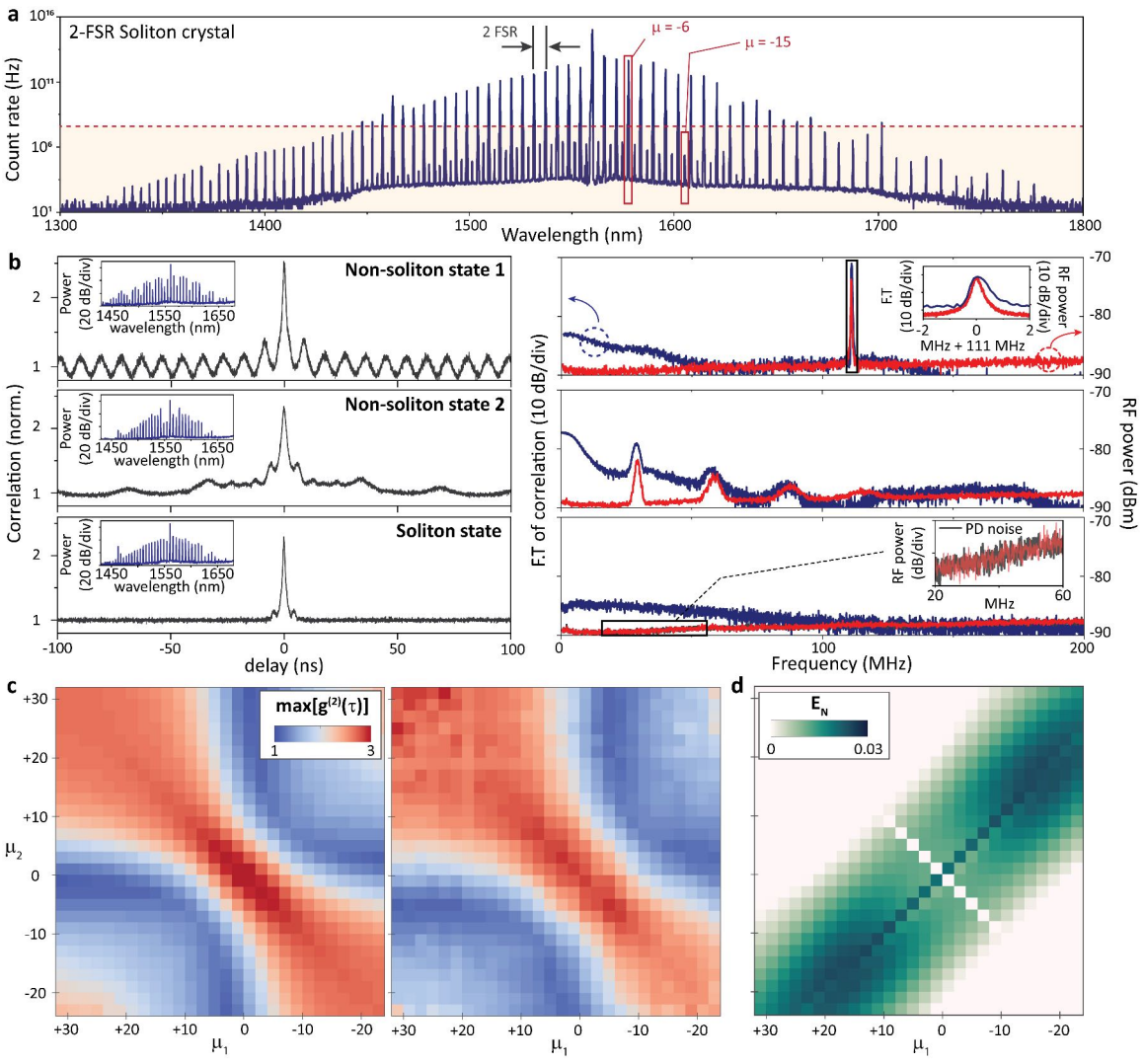


Figure 3.5: **Quantum correlations in non-phase-locked combs and perfect soliton crystals** **(a)**A SPOSA spectrum of a 2-FSR soliton crystal. **(b)** Left: The measured $g^{(2)}(\tau)$ at mode $\mu = -15$ for different 2-FSR states observed in the device (inset shows an OSA spectrum of the measured state). Right: The RF beat note measured on a photodetector at mode $\mu = -6$ (red), and the Fourier transform of the measured $g^{(2)}(\tau)$ (blue). Bottom panel includes the photodetector noise floor, corroborating the low-noise soliton state. **(c)** The second-order correlations matrix for the below-threshold modes in the 2-FSR soliton crystal. Left: theoretical model; Right: experimental data. **(d)** The logarithmic negativity ($E_N$) matrix calculated for the 2-FSR soliton crystal assuming $10\times$ increased out-coupling of the below-threshold modes. No pairwise entanglement is predicted in the device with unmodified waveguide coupling.

### 3.4.1 Logarithmic negativity

The observation of all-to-all coupling in the 2-FSR soliton crystal quantum state is suggestive of an interesting entanglement structure. One may ask whether squeezing is generated in the system. This

question is the topic of Chapter 4. Meanwhile, we may ask whether entanglement more generally is generated between pairs of modes in the system. One metric for entanglement is the logarithmic negativity. Here, we compute the logarithmic negativity [54], $E_N$, for all mode pairs to assess the entanglement across the 2-FSR soliton crystal in the resonator mode basis.

In steady state ($t \to \infty$), the density matrix describing any two modes $\alpha$ and $\beta$ is described by a Gaussian Wigner function:

$$W_{\alpha,\beta}(q_{\alpha,\beta} = [x_\alpha, p_\alpha, x_\beta, p_\beta]^T) = \frac{1}{\pi\sqrt{\mathrm{Det}[\Sigma_{\alpha,\beta}]}} \exp\left(q_{\alpha,\beta}^T \Sigma_{\alpha,\beta} q_{\alpha,\beta}\right) \tag{3.6}$$

where $\Sigma_{\alpha,\beta} = \langle q_{\alpha,\beta} q_{\alpha,\beta}^T \rangle_W$ is the $4 \times 4$ steady state correlation matrix formed from Weyl-ordered operators. The entanglement measure between these two modes can be computed as a log-negativity of this matrix, defined by

$$\mathcal{E}_{\alpha,\beta} = \max[0, -\log(\sqrt{2}\eta)] \tag{3.7}$$

where

$$\eta = \sqrt{\Theta - \sqrt{\Theta^2 - 4\mathrm{Det}(\Sigma_{\alpha,\beta})}} \tag{3.8}$$

and

$$\Theta = \mathrm{Det}(\Sigma_\alpha) + \mathrm{Det}(\Sigma_\beta) - 2\mathrm{Det}(C) \tag{3.9}$$

and $\Sigma_\alpha, \Sigma_\beta$ and $C$ are defined as different blocks of $\Sigma_{\alpha,\beta}$

$$\Sigma_{\alpha,\beta} = \begin{bmatrix} \Sigma_\alpha & C \\ C^T & \Sigma_\beta \end{bmatrix} \tag{3.10}$$

To compute the correlation matrix $\Sigma_{\alpha,\beta}$ from a quadratic Hamiltonian, it is convenient to express the correlation elements in terms of annihilation operators. We can immediately note that

$$\langle x_\alpha x_\beta \rangle_W = \frac{1}{2}\left[\langle a_\alpha a_\beta \rangle + \langle a_\alpha^\dagger a_\beta^\dagger \rangle + \langle a_\alpha^\dagger a_\beta \rangle + \langle a_\alpha a_\beta^\dagger \rangle\right] \tag{3.11a}$$

$$\langle p_\alpha p_\beta \rangle_W = -\frac{1}{2}\left[\langle a_\alpha a_\beta \rangle + \langle a_\alpha^\dagger a_\beta^\dagger \rangle - \langle a_\alpha^\dagger a_\beta \rangle - \langle a_\alpha a_\beta^\dagger \rangle\right] \tag{3.11b}$$

$$\langle x_\alpha p_\beta \rangle_W = \langle p_\beta x_\alpha \rangle_W = \frac{i}{2}\left[\delta_{\alpha,\beta} + \langle a_\alpha^\dagger a_\beta^\dagger \rangle - \langle a_\alpha a_\beta \rangle + \langle a_\beta^\dagger a_\alpha \rangle - \langle a_\beta a_\alpha^\dagger \rangle\right] \tag{3.11c}$$

The correlators for the annihilation operators required above can be easily calculated from the input-output formalism. Recall that for a quadratic, time-invariant Hamiltonian, the Heisenberg equations

read

$$\frac{d}{dt}\begin{bmatrix} a(t) \\ a^\dagger(t) \end{bmatrix} = Q_{\text{eff}}\begin{bmatrix} a(t) \\ a^\dagger(t) \end{bmatrix} + M\begin{bmatrix} b_{in}(t) \\ b_{in}^\dagger(t) \end{bmatrix} \tag{3.12}$$

Physically, we expect eigenvalues of $Q_{\text{eff}}$ to all have negative real part so as to have a well defined steady state. We then obtain by integrating the above equations that as $t \to \infty$

$$\begin{bmatrix} a(t) \\ a^\dagger(t) \end{bmatrix} = \int_0^t e^{Q_{\text{eff}}(t-\tau)} M \begin{bmatrix} b_{in}(\tau) \\ b_{in}^\dagger(\tau) \end{bmatrix} d\tau = \int_0^t X e^{\Lambda(t-\tau)} X^{-1} M \begin{bmatrix} b_{in}(\tau) \\ b_{in}^\dagger(\tau) \end{bmatrix} d\tau \tag{3.13}$$

where we can define the eigenvalue decomposition $Q_{\text{eff}} = X\Lambda X^{-1}$. It is now straightforward to calculate

$$\lim_{t\to\infty} \langle \begin{bmatrix} a(t) \\ a^\dagger(t) \end{bmatrix} \begin{bmatrix} a^\dagger(t) & a(t) \end{bmatrix} \rangle = \lim_{t\to\infty} \int_0^t X e^{\Lambda(t-\tau)} X^{-1} M M^\dagger X^{-\dagger} e^{\Lambda^*(t-\tau)} X^\dagger d\tau = XNX^\dagger \tag{3.14}$$

where $N$ is a matrix whose elements are given by

$$N_{i,j} = \frac{[X^{-1}MJM^\dagger X^{-\dagger}]_{i,j}}{\lambda_i + \lambda_j^*} \tag{3.15}$$

defined in terms of the eigenvalues of $Q_{\text{eff}}$, $\lambda_i$, where $J$ is a $2N \times 2N$ matrix:

$$J = \left[\begin{array}{c|c} I(N) & 0 \\ \hline 0 & 0 \end{array}\right]$$

We find that in this basis, no pair-wise entanglement is numerically predicted in the measured device. As will be shown in Chapter 4, this is not because entanglement is absent, but because the pair-wise mode basis is not the natural basis for this multimode system. Nonetheless, even in the native mode basis, we find that entanglement can exist if a modified device architecture is employed. Consider a *photonic molecule* device where the below-threshold modes are overcoupled to the output waveguide via a auxiliary microring[55, 56]. This architecture is advantageous because it allows for the efficient extraction of the quantum optical fields from the device while simultaneously filtering them from the coherent fields, all without impacting the soliton crystal (Fig. 3.6). For this system, we numerically observe all-to-all entanglement along the signal-idler diagonal of the pump (Fig. 3.5d). Such entanglement structure is consistent with the all-to-all connectivity in the 2-FSR soliton crystal Hamiltonian.

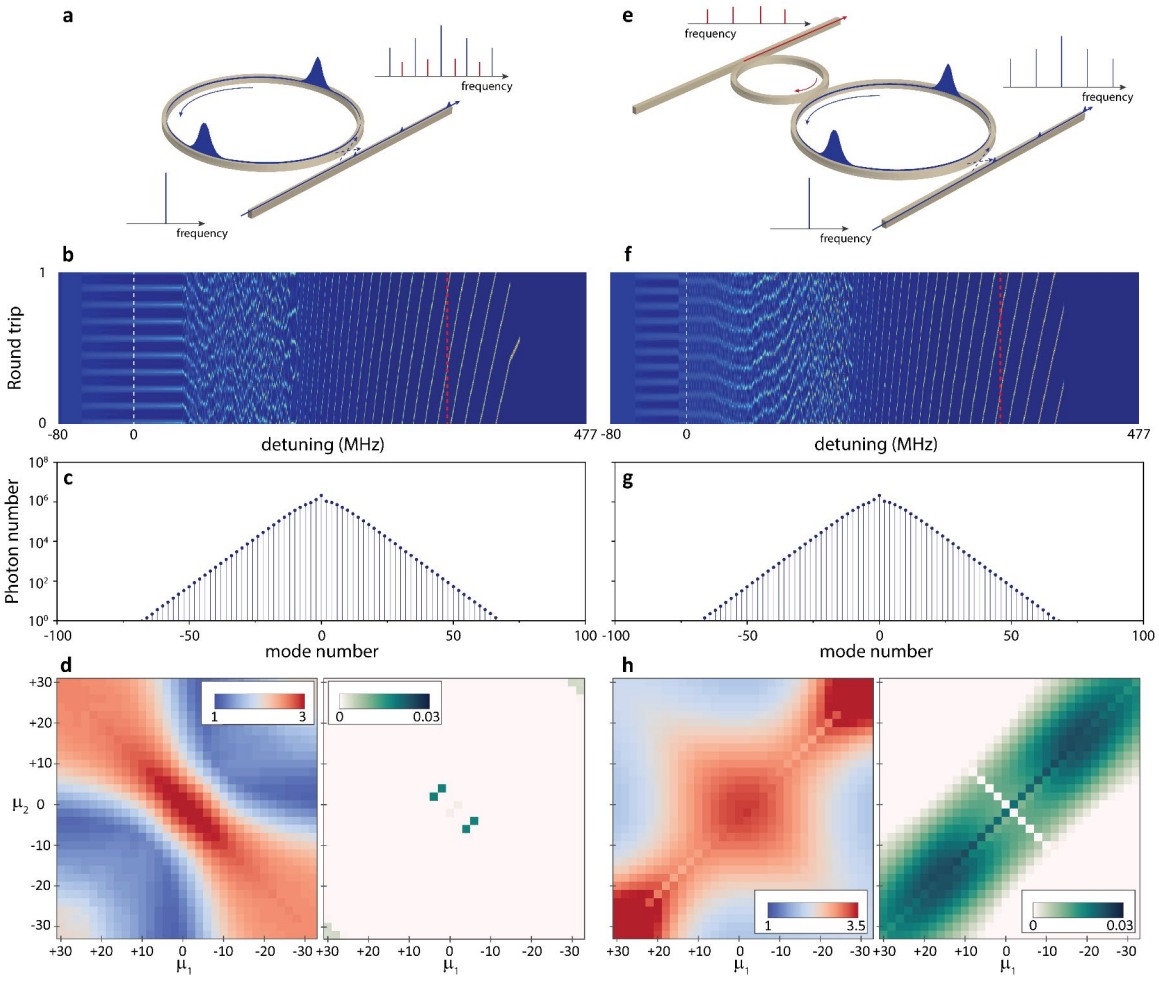


Figure 3.6: **Photonic molecule architecture for all-to-all entanglement generation (a)** Schematic of the experimentally-demonstrated device. **(b)** LLE simulation of the device for pump power of 6.6 mW in the waveguide. The desired 2-FSR soliton crystal state exists for detuning in the range 175–395 MHz. This simulated soliton step width of 220 MHz is somewhat larger than the experimentally-observed step width of 150 MHz. **(c)** The simulated spectrum taken at detuning of 330 MHz. **(d)** Left: The two-photon correlation matrix computed for the state in (c). The scale bar indicates $\max\{g^{(2)}(\tau)\}$. Right: The corresponding entanglement negativity, $E_N$, matrix. (e-h) correspond to (a-d) but for the photonic molecule configuration, where the out-coupling of the odd resonator modes is increased by 10 times via the auxilliary resonator **(e)** Schematic of the photonic molecule configuration. **(f)** It is confirmed via LLE that the same 2-FSR soliton crystal state can be captured in simulation. **(g)** The spectrum of the comb at the same detuning of 330 MHz is identical to the comb spectrum in the unmodified device, since only the below-threshold modes are affected by the addition of the auxiliary ring. **(h)** The corresponding correlation and entanglement matrices for the photonic molecule device.

### 3.4.2 Photonic molecule analysis

The second-order correlation matrix for the 2-FSR soliton crystal state (Fig. 3.5) was computed via LLE simulation and input-output theory using the following parameters:

- $D_2/2\pi = 3.65$ MHz, obtained from FEM simulation, neglecting higher-order terms. A single perturbation of $-30$ MHz was introduced at mode $\mu = -2$ to induce the formation of the soliton crystal state [49].
- For the pump mode ($\mu = 0$), the intrinsic and coupling Q factors of 2.37 and 6.55 million, respectively, were used, extracted from the measured cold-cavity transmission spectrum.
- For the other modes, intrinsic and coupling Q of 2.77 and 7.47 million, respectively, were used, corresponding to the mean of the measured Q factors for the modes within the laser scanning range ($\mu = -3$ to $+14$).
- Pump power of 6.6 mW in the waveguide, corresponding to the experimentally-measured value.

The result of the LLE simulation is shown in Fig. 3.6b. The simulated soliton crystal spectrum for the detuning of 330 MHz is shown in Fig. 3.6c. In the input-ouput theory model, the laser detuning (within the range of existence of the soliton state in the LLE simulation) is the only free parameter. The corresponding second-order photon correlations and $E_N$ matrices are shown in Fig. 3.6d. Negligible entanglement is thus predicted in the resonator mode basis for this soliton crystal state. However, entanglement can be recovered by selectively over-coupling the below-threshold modes via a photonic molecule configuration, shown in Fig. 3.6e. This configuration is as follows: The auxillary resonator has a FSR that is 2 times larger than the FSR of the primary microring. The coupling strength of the two ring resonators exceeds the total losses (scattering and waveguide coupling) of the primary resonator. The auxillary ring is further over-coupled to its output waveguide, so that rather than be strongly-coupled to the primary resonator, the auxillary resonator acts as a selective out-coupling channel for the odd-numbered modes of the primary resonator. We note that the finesse of the experimentally demonstrated resonators (approximately 3500) is sufficient for this architecture. To model this system, we perform the LLE simulation with the same device parameters as for the experimentally demonstrated device, but with the out-coupling rates of the odd modes increased by 10 times. We numerically confirm that the same 2-FSR soliton state can be prepared for this device (Fig. 3.6f). The computed second-order correlation and $E_N$ matrices for the the quantum state of this device are shown in Fig. 3.6h.

### 3.4.3 7-FSR soliton crystal

In ($N > 3$)-FSR soliton crystals, the below threshold modes are not all-to-all coupled. Instead, the modes are divided into disjoint sets grouped by the value $|\mu \mod N|$, as per the mode-matching

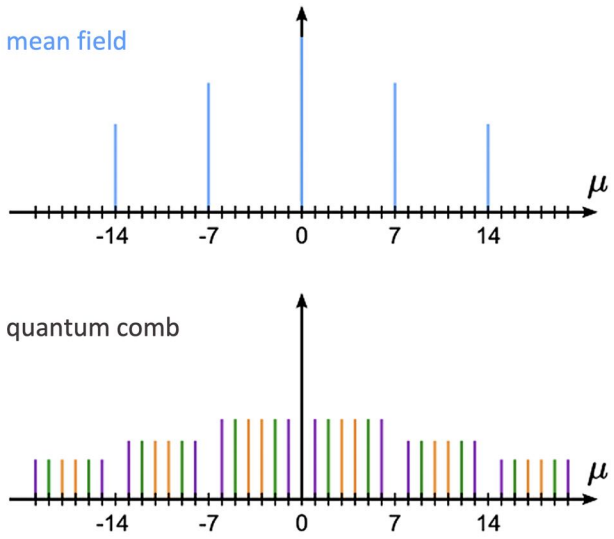


Figure 3.7: **Connectivity in the 7-FSR soliton crystal.** Diagram of the connected subgroups. The mean field comb is measured in blue and the below-threshold light is colored purple, green, and orange. The three colors represent the three connected subgroups.

condition. Thus, $\lfloor N/2 \rfloor$ non-interacting subsets (each internally all-to-all coupled) are expected in an N-FSR soliton crystal. Indeed, for the 7-FSR soliton crystal state presented in Fig. 3.1d, we experimentally confirm three disjoint all-to-all correlated sets of modes (see Fig. 3.7 for a diagram of the connectivity).

Figure 3.8 presents the generation of a 7-FSR soliton crystal state in a different device. The optical spectrum (Fig. 3.8a) as well as the transmission and comb power traces across the pump resonance identify the existence of the soliton state. The SPOSA spectrum (Fig. 3.8c) reveals quantum frequency comb lines which were obscured by the noise floor of the OSA spectrum, and their correlation matrix is presented with the prediction from the LLE-driven linearized model (Fig. 3.8d). Again we observe good agreement with the model. The multimode entanglement structure will be more precisely understood in the next chapter, through squeezed supermode analysis.

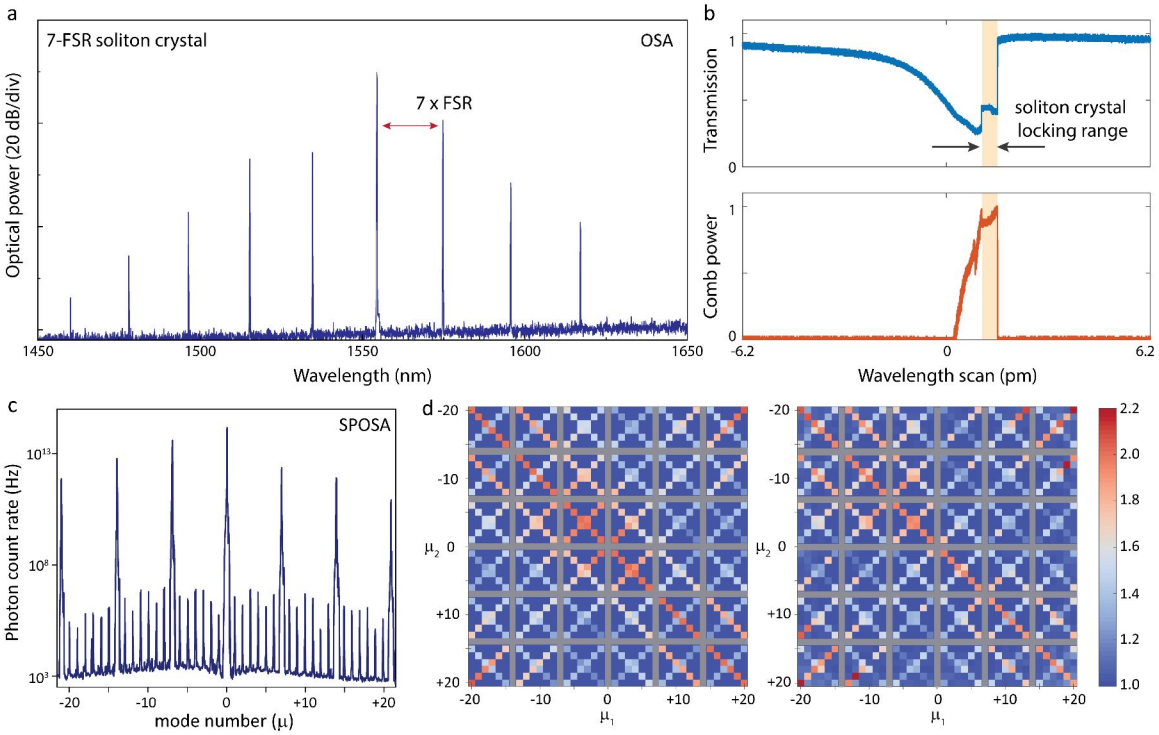


Figure 3.8: **7-FSR soliton crystal state** (**a**) OSA spectrum of the soliton crystal state. (**b**) Pump power transmission (upper panel) and comb power (lower panel) versus wavelength tuning when the pump laser is scanned from blue to red across the pump resonance. (**c**) Optical spectrum of the soliton state measured using the SPOSA. (**d**) The $\max[g^{(2)}(\tau)]$ correlation matrix for the below threshold modes in the 7-FSR soliton state (Left: theoretical model, Right: experimental data).

# Chapter 4

# Multimode squeezing in soliton crystal microcombs

In Chapter 3, we described a linearized model for the quantum fluctuations of the below-threshold modes that exist within soliton crystal microcombs. We then used two-photon correlations to validate the model. In this Chapter, we further study the linearized model of DKS states to predict the quadrature squeezing that may exist across the dissipative Kerr soliton.

As discussed in the Introduction, the optical mean field of the Kerr frequency comb (*i.e.*, the "classical" comb) has been modeled with great success by the Lugiato-Lefever equation (LLE) [23], a nonlinear Schrödinger equation which includes dissipation, drive, and detuning. The most commonly studied configuration is that where a single coherent pump laser supplies parametric gain to populate the comb lines through stimulated four-wave mixing [24]. Spontaneous light generation is absent from the model; in order to seed threshold processes such as optical parametric oscillation (OPO), random noise must be added into every optical mode. Thus, the LLE can reveal neither the properties of the quantum state of the comb, nor the coherent dynamics of the threshold processes that drive the formation of the comb itself.

The quantum state of soliton microcombs has received little attention, and studies to-date (including the work of Chapter 3) have approached it via an extension of pairwise mode analysis [32, 46] which is used to describe signal-idler quantum frequency combs [25, 57, 35]. However, the signal-idler basis cannot be expected to capture the structure of the collective quantum fluctuations in a soliton microcomb due to the extended modal coupling (Fig. 4.1), suggesting the need for a multimode analysis.

An example of a well-studied multimode system is the synchronously-pumped optical parametric oscillator (SPOPO), where an external mode-locked classical comb source drives a quantum comb via a second-order ($\chi^{(2)}$) nonlinear process. While SPOPO may also be performed with a third-order

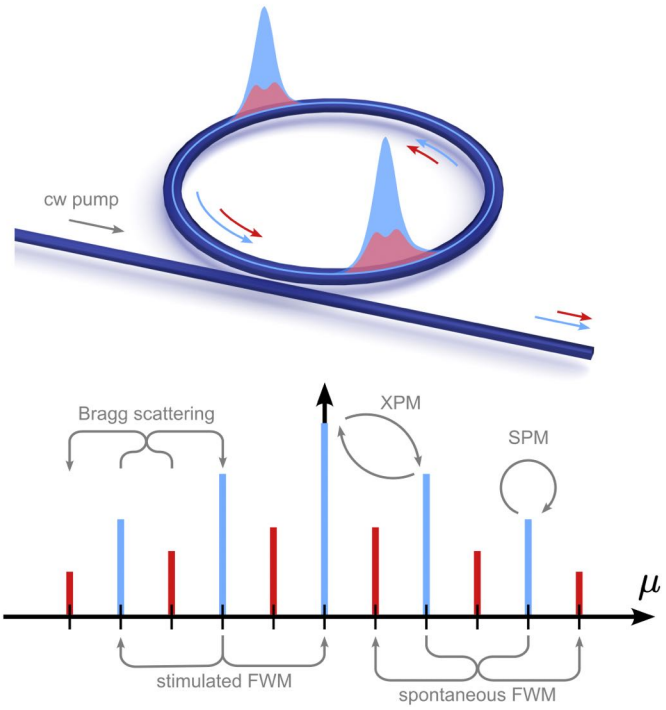


Figure 4.1: **A schematic depiction of a soliton crystal state in a Kerr microresonator.** Top: A continous-wave pump laser is evanescently coupled into the microring through a bus waveguide and used to generate the soliton crystal. In the temporal domain, the below-threshold state (red) co-propagates with the coherent soliton pulses (blue). Bottom: In the frequency mode basis, the above- and below-threshold modes form two subsets, allowing the quantum fluctuations to be studied in isolation.

nonlinearity, the majority of experimental and theoretical studies have considered SPOPO using the second-order optical nonlinearity. In this case, the pump comb is centered around frequency $2\omega_0$ which drives pair generation (spontaneous parametric down-conversion) in a comb centered at $\omega_0$. The frequency-spacing $\Delta\omega$ of the resonator modes centered around $\omega_0$ matches the repetition rate of the pump pulses. This system features all-to-all connectivity across the below-threshold modes, and the four-wave mixing interaction Hamiltonian can be written

$$H_{\text{int}} = \sum_{m,n} [G_{m,n} a_m^\dagger a_n^\dagger + h.c.] \tag{4.1}$$

We can diagonalize this interaction Hamiltonian into independent squeezers, whose composition in the native mode basis is given by the eigenvectors of the matrix $G$. The eigenvalues reflect the gain and the degree of squeezing of each supermode. The OPO threshold condition of the system is defined by the largest eigenvalue with respect to the loss rate. For a Gaussian pump pulse, the squeezed supermodes resemble Hermite-Gauss modes, where the lowest order (Gaussian) mode

features the highest degree of squeezing. By shaping a local oscillator to match the supermode spectrum in amplitude and phase, the squeezing across the different supermodes may be measured using homodyne detection.

The SPOPO is naturally described in a basis of *supermodes* (*i.e.*, superpositions of frequency modes) [58, 59] and this basis reveals multimode quadrature squeezing [60, 61]. The result is multimode squeezed states that are multiplexed both in the temporal and spectral degrees of freedom. Exploitation of the temporal degree of freedom with continuous-variable optical states has enabled the largest continuous-variable cluster states. However, the spectrally-defined multimode squeezing structure allows for reconfigurability of the entanglement [61] as well as mode-selective non-Gaussian operations [62].

Three key features distinguish the soliton microcomb from previously-studied squeezed light sources. First, Kerr cavity soliton systems typically feature (and rely on) significant modal dispersion, which contributes strongly detuned parametric processes. Second, the third-order ($\chi^{(3)}$) nonlinearity in soliton microcombs introduces four-wave mixing nonlinear terms not present in $\chi^{(2)}$ systems, most notably Bragg scattering (frequency translation of a photon). In degenerate and signal-idler squeezing schemes, these system properties are often considered as parasitic processes that degrade squeezing [63, 64]. Finally, the quantum fluctuations in a soliton microcomb are driven not by an external source [65], but by a coherent comb that is itself generated *in situ* via the same Kerr nonlinearity, intimately linking the mean-field and the below-threshold states.

In this Chapter, we apply a multimode quadrature squeezing analysis to the soliton microcomb and its formation. We show that multimode analysis is necessary to understand Kerr microcomb threshold processes beyond the single-pump regime, and that such analysis can predict the properties of the post-threshold mean field, such as spatiotemporal oscillations. We find that the quantum state of the soliton crystal microcomb is highly squeezed across the entire range of its existence, and that the passage from a soliton crystal to a single soliton state is a coherent threshold process associated with asymptotic growth in squeezing. Finally, we describe how the soliton crystal can be engineered as a practical source of multimode quadrature-squeezed light.

## 4.1 Bloch-Messiah decomposition

The quantum fluctuations of the soliton microcomb are described by a many-body quartic Hamiltonian, where all resonator modes are coupled by a four-photon interaction through the $\chi^{(3)}$ nonlinearity of the medium. In a soliton crystal microcomb [66, 8], as we saw in Chapter 3, the resonator modes can be partitioned into two sets: (i) above-threshold modes populated via stimulated four-wave mixing and comprising the classical dissipative Kerr soliton state, and (ii) the below-threshold modes populated only via spontaneous four-wave mixing [46]. Due to this robust partition guaranteed by energy and momentum conservation, the soliton crystal forms a unique system for studying

in isolation the quantum fluctuations of dissipative Kerr solitons. To model the quantum state, the simplest approach is to assume that the above-threshold modes are in a classical coherent state [38] (complex amplitudes $A_m$) and that this coherent state drives parametric processes in the below-threshold modes $\hat{a}_j$. In Chapter 3, this approximation was used to predict the second-order photon correlations that exist across the below-threshold modes of a soliton crystal state, measured pairwise in the resonator basis [46].

For convenience, we include again the coupled-mode equations recovered from the linearized Hamiltonian,

$$\begin{aligned}\frac{d\hat{a}_\mu(t)}{dt} =& -\left(i\delta_\mu + \frac{\kappa_\mu}{2}\right)\hat{a}_\mu(t) \\ &+ ig_0 \sum_{\nu,j,k} \delta[\mu+\nu-j-k] A_j A_k \hat{a}^\dagger_\nu(t) \\ &+ 2ig_0 \sum_{\nu,j,k} \delta[\mu+j-\nu-k] A^*_j A_k \hat{a}_\nu(t) \\ &- \sqrt{\kappa_\mu}\hat{b}_{\mathrm{in},\mu}(t) \end{aligned} \tag{4.2}$$

where $\kappa_\mu$ is the total decay rate of mode $\mu$ [46], $\delta_\mu$ is the detuning from the rotating frame (set by the group velocity of the soliton), and $\hat{b}_{\mathrm{in},\mu}$ are the bath operators. In equation 4.2, the first term accounts for the modal detunings (dispersion); the second term represents pair generation; the third term describes XPM and Bragg scattering; and the last term is the coupling to the bath.

From equation 4.2, it is evident that the presence of multiple pump modes $A_j$ generates multi-mode coupling, resulting in collective comb dynamics that cannot be understood through pairwise mode analysis. An example of such a collective effect is the temporal envelope of the below-threshold comb, obtained from the steady-state solution of equation 4.2. The temporal shape of the quantum fluctuations does not mimic that of the mean field, but rather has a split shape (Fig. 4.1). The origin of this peculiar feature will, in a later section, be understood through the supermode decomposition.

To calculate the maximally-squeezed supermodes of the system, we rewrite the Heisenberg equations in the basis of the quadrature operators of each mode $r(t) = (x_1(t), ..., x_n(t) | y_1(t), ..., y_n(t))^T$ where $x_n = \frac{1}{\sqrt{2}}(a_n^\dagger + a_n)$ and $y_n = \frac{i}{\sqrt{2}}(a_n^\dagger - a_n)$. Input-output relations can be written for the quadrature operators as $r_{\mathrm{out}}(t) = r_{\mathrm{in}}(t) + \sqrt{\Gamma} r(t)$ where $\Gamma$ is a diagonal matrix of the cavity decay rates $\kappa_\mu$. In the Fourier basis, the input and output fields are related by a transfer matrix, $S(\omega)$:

$$r_{\mathrm{out}}(\omega) = S(\omega) r_{\mathrm{in}}(\omega) \tag{4.3}$$

which can be diagonalized by Euler decomposition [67, 68]:

$$S(\omega) = U(\omega) D(\omega) V^\dagger(\omega). \tag{4.4}$$

The matrix $D(\omega)$ is diagonal with corresponding anti-squeezing and squeezing levels associated with maximally-squeezed orthogonal supermodes encoded in $U(\omega)$: the columns define the linear combination of quadratures, which can be mapped to a local oscillator for homodyne detection of the squeezing for $\omega$ where $U(\omega)$ is real. This is always the case for $\omega = 0$. For systems with terms corresponding to detuning or Bragg scattering, the ideal local oscillator configuration will depend on the Fourier frequency [69, 67]: *e.g.*, the ideal local oscillator configuration for measuring maximum squeezing at zero Fourier frequency may measure sub-optimal squeezing across the rest of the spectrum.

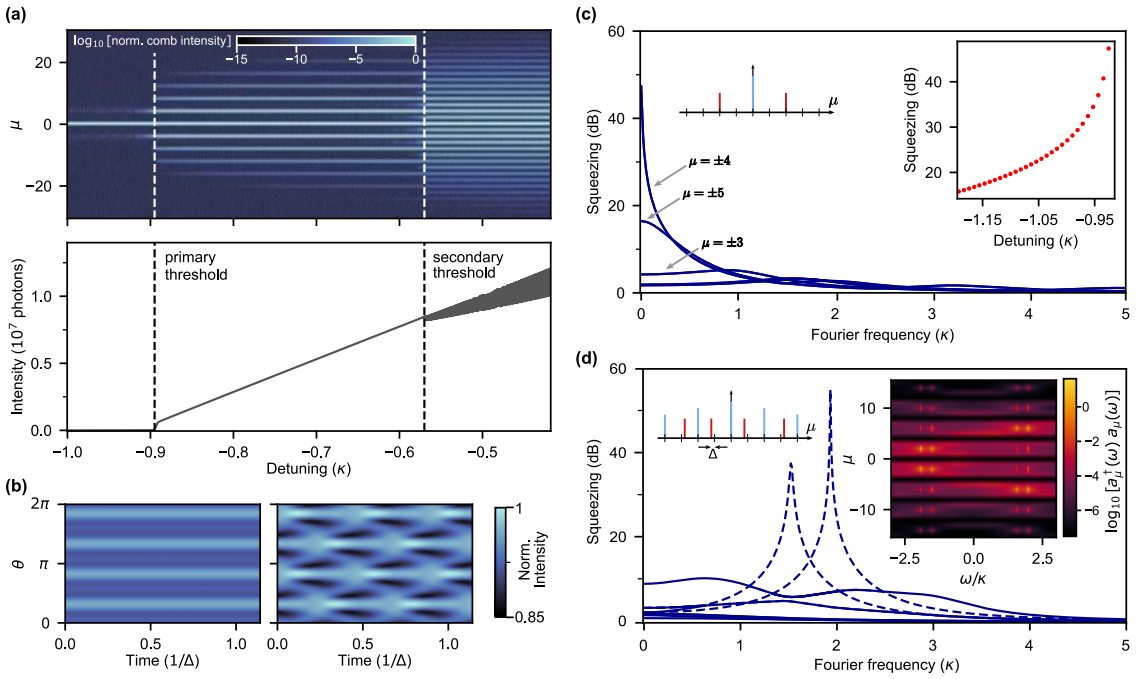


Figure 4.2: **Supermode analysis of primary and secondary comb formation. (a)** Intracavity comb intensity simulated via LLE. Top: Spectral composition of the comb. Bottom: Integrated comb intensity. Here and onward, frequency quantities are written in units of loss rate $\kappa$. **(b)** Azimuthal distribution in the rotating frame for a state at detuning of $-0.7\kappa$ (left) and $-0.5\kappa$ (right). **(c)** Squeezed supermode spectrum near the threshold of primary comb formation (detuning of $-0.93\kappa$). All supermodes are doubly-degenerate. Here and onward, unless otherwise stated, squeezing eigenspectra represent minimum uncertainty states. The maximally-squeezed supermode is composed of a signal-idler pair at modes $\pm\mu$. Left inset: Illustration of the highest-gain supermode. Right inset: Maximum squeezing versus detuning, up to the primary comb threshold. **(d)** Squeezed supermode spectrum near the threshold of the secondary comb (detuning of $-0.60\kappa$). Dashed (solid) lines represent non-degenerate (doubly-degenerate) modes. Left inset: Illustration of the detunings in the highest-gain supermode. Right inset: The spectral composition of below-threshold modes approaching secondary threshold.

## 4.2 Multimode analysis of comb formation

We begin with the supermode analysis of the stages of the microcomb that precede the soliton. The mean-field Hamiltonian coupling terms $A_m$ are obtained via an LLE simulation. We use system parameters consistent with the SiCOI microrings measured in Chapter 3: nonlinear coupling $g_0/2\pi =$ 3.4 Hz, a free spectral range of $D_1/2\pi = 350$ GHz, integrated quadratic dispersion $D_2/2\pi = 30$ MHz, and a loaded quality factor of $Q = 1.5 \cdot 10^6$ with critical coupling to the bus waveguide. The loss rate is assumed equal for all modes, and denoted as $\kappa$ (*i.e.*, $\kappa_\mu = \kappa$). We note that these parameters are similar to soliton devices in many material platforms such as silicon nitride [8, 66, 24], lithium niobate [70, 71], and tantala [72]. Figure 4.2(a) shows the evolution of intra-cavity mode amplitudes $A_m(t)$ under adiabatic red-tuning of the pump laser through the formation of primary and secondary combs. The formation of the primary comb produces a spatial rolls pattern, and the subsequent formation of the secondary comb generates spatiotemporal oscillations (Fig. 4.2(b)).

A powerful feature of supermode analysis is the ability to reveal the multimode nature of threshold processes. Figure 4.2(c) illustrates the supermode analysis near the primary comb threshold: here, maximally-squeezed supermodes consist of signal-idler pairs [25, 57] described by the supermodes $\frac{1}{\sqrt{2}}(\hat{a}_{-\mu} + \hat{a}_\mu)$ and $\frac{i}{\sqrt{2}}(\hat{a}_{-\mu} - \hat{a}_\mu)$, reflecting the amplitudes and phases of the local oscillators that could be used for homodyne detection. The well-known result of this single-pump Hamiltonian is that phase matching dictates which pair reaches threshold first, and predicts the spacing of the subsequent primary comb [24]. We now turn to the formation of the secondary comb: with the multiple nonzero-amplitude modes of the primary comb, the connectivity in the Hamiltonian increases beyond pairwise mode interactions. The squeezing spectrum just before the secondary-comb threshold is shown in Figure 4.2(d). The maximally-squeezed supermode approaches the threshold at a nonzero Fourier frequency $\omega = \Delta$, indicating the presence of detuning in the multimode parametric gain process. To understand the origin of this detuning in the squeezing spectrum, we can examine the spectral composition $\langle \hat{a}^\dagger_\mu(\omega)\hat{a}_\mu(\omega)\rangle$ of the below-threshold modes which, near threshold, is dominated by emission into the first supermode. The spectral composition (Fig. 4.2(d)) reveals that the supermode consists of two quantum subcombs of equal and opposite detuning from the primary comb spacing. This detuning in the squeezing spectrum predicts the RF beatnote $2\Delta$ that accompanies the formation of the secondary comb [24], giving rise to the spatiotemporal oscillation [50] seen in the numeric solution of the LLE (Fig. 4.2(b)). Thus, the supermode analysis sheds light on the formation process (contrasting the pair-wise mode analysis of secondary-comb formation [24]), and furthermore predicts the dynamics of the ensuing secondary comb.

## 4.3 Soliton crystal and its annihilation

After the formation of the secondary comb, the system enters the chaotic — modulation instability (MI) — regime. We will not discuss the MI state: the Hamiltonian is time-dependent and a

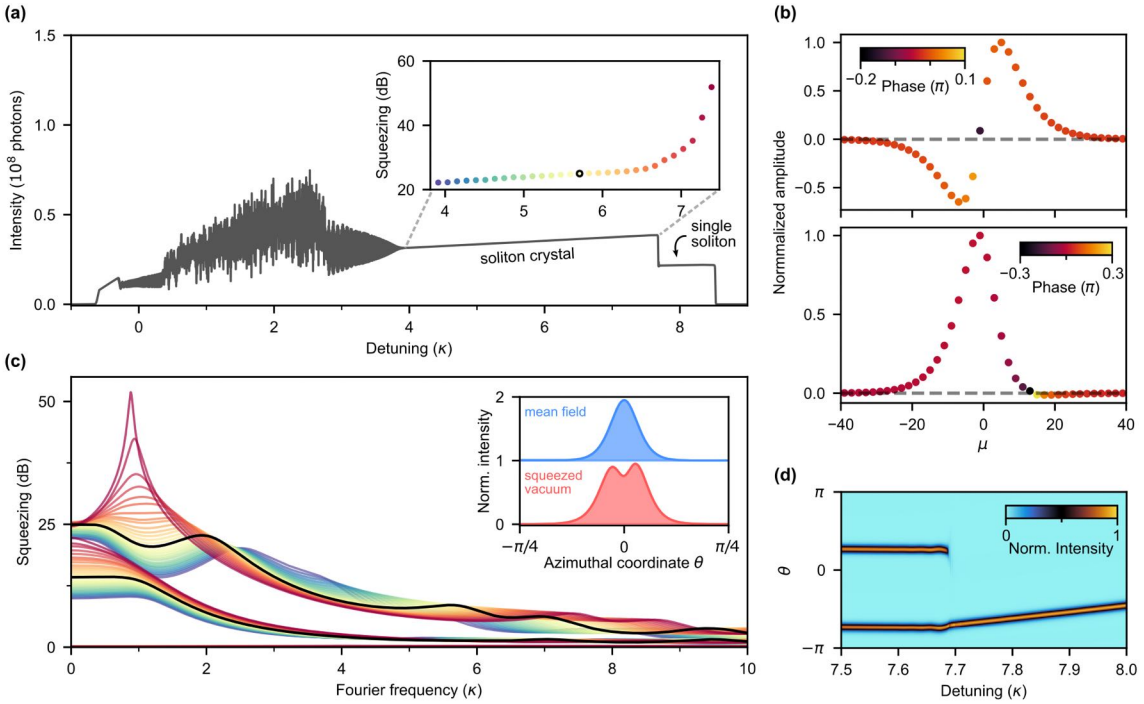


Figure 4.3: **Squeezed supermodes of a soliton crystal. (a)** Intracavity comb intensity simulated via LLE. Inset: Maximum supermode squeezing along the soliton crystal step. **(b)** Maximally-squeezed supermodes at zero Fourier frequency at the middle of the step (detuning of $5.7\kappa$). Top: quasi-$HG_1$ mode; Bottom: quasi-$HG_0$ mode. **(c)** Complete eigenspectrum of the soliton crystal versus detuning. Black curves represent the eigenspectrum at detuning $5.7\kappa$. Other detunings are shown in colors matching the inset of (a). Inset: The temporal shape of the squeezed vacuum $\langle \hat{a}^\dagger(\theta)\hat{a}(\theta)\rangle$, where $\hat{a}(\theta) = \sum_\mu \hat{a}_\mu(t)e^{i\mu\theta}$ (red), as compared with the mean field (blue), at detuning $5.7\kappa$. **(d)** LLE simulation showing the annihilation of the soliton crystal in the temporal domain.

subspace of below-threshold modes cannot be clearly delineated, thereby complicating the quantum analysis. In order to induce soliton-pair crystallization from the MI state, we introduce a $-100$ MHz perturbation at $\mu = +2$ (as described in Ref. [8]). In the LLE simulation (Fig. 4.3a), the MI state can be seen to end in a low-noise 2-FSR soliton crystal state, followed by an abrupt transition to the single soliton.

We analyze the quadrature squeezing for the below-threshold state as it evolves with detuning across the soliton crystal step. The state features significant spatiotemporal precession with respect to the resonator free spectral range and care must be taken to perform the squeezing analysis in the stationary frame of the mean-field solution for each detuning. This procedure is described in Section 4.5. The inset of Fig. 4.3(a) shows the evolution of maximum squeezing which exceeds 20 dB for all detunings. The maximally-squeezed supermodes extend across the entire comb (Fig. 4.3(b)) and resemble the Hermite-Gauss (HG) modes, the eigenmodes of SPOPO [59]. This reflects the

all-to-all coupling in the Hamiltonian.

The evolution of the complete supermode eigenspectrum across the soliton crystal step is shown in Fig. 4.3(c). For all detunings, two supermodes show strong and comparable levels of squeezing while the rest have levels below 0.5 dB. This two-mode dominance of the eigenspectrum is a unique feature to the soliton crystal, unobserved in other multimode systems studied to date [73, 59, 68, 65], although Hermite-Gauss-like squeezed supermodes have been predicted in soliton propagation through a $\chi^{(3)}$ fiber [68]. The supermode structure of the squeezed vacuum explains the puzzling contrast between its temporal profile and that of the mean field, shown in the inset of Fig. 4.3(c): the strong contribution of the quasi-$HG_1$ supermode (whose Fourier transform to the time-domain is also bi-modal) induces the temporal splitting of the squeezed vacuum pulse.

Obtaining the temporal shape of the squeezed vacuum corresponds to the evaluation of the azimuthal photon number operator, $\langle \hat{a}^\dagger(\theta)\hat{a}(\theta)\rangle$, where

$$\hat{a}(\theta) = \sum_{\mu} \hat{a}_\mu(t) e^{i\mu\theta}.$$

The evaluation is performed in the rotating frame of the soliton and is thus time-independent. To compute intra-cavity expectation values, we relate the cavity operator to the input bath operators via a $n \times 2n$ transfer matrix $Q$ which follows from the system Hamiltonian:

$$\hat{a}_\mu(\omega) = \sum_{k=1}^{n} \left[ Q_{\mu,k}(\omega)\hat{b}_{\mathrm{in,k}}(\omega) + Q_{\mu,k+n}(\omega)\hat{b}^\dagger_{\mathrm{in,k}}(-\omega) \right]$$

where $n$ is the number of longitudinal modes. Via the commutation relations

$$\left\langle \hat{b}_{\mathrm{in,i}}(\omega)\hat{b}^\dagger_{\mathrm{in,j}}(\omega') \right\rangle = \delta_{ij}\delta(\omega - \omega'),$$

$$\left\langle \hat{b}^\dagger_{\mathrm{in,i}}(\omega)\hat{b}_{\mathrm{in,j}}(\omega') \right\rangle = 0$$

where the expectation value is taken with respect to the initial vacuum state, we arrive at the expression

$$\langle \hat{a}^\dagger(\theta)\hat{a}(\theta)\rangle = \sum_{l,m,k} e^{i(l-m)\theta} \int_{-\infty}^{\infty} d\omega \; Q^*_{m,k+n}(\omega) Q_{l,k+n}(\omega)$$

Furthermore, an anti-crossing in the squeezing values of the two dominant supermodes is observed (Fig. 4.3(c)), in contrast to the signal-idler pairs preceding primary comb formation, where no modal interaction is revealed in the squeezing spectra (Fig. 4.2(c)). The apparent interaction of the supermodes at the anti-crossing is further evidenced by the hybridization of the supermode shapes. Even at zero Fourier frequency, the phase profile of the quasi-$HG_0$ mode (Fig. 4.3(b)) reveals a contribution of the odd quasi-$HG_1$ mode. This anti-crossing is observed universally for higher-order soliton crystals as well (see Section 4.5). Its physical significance is not yet understood.

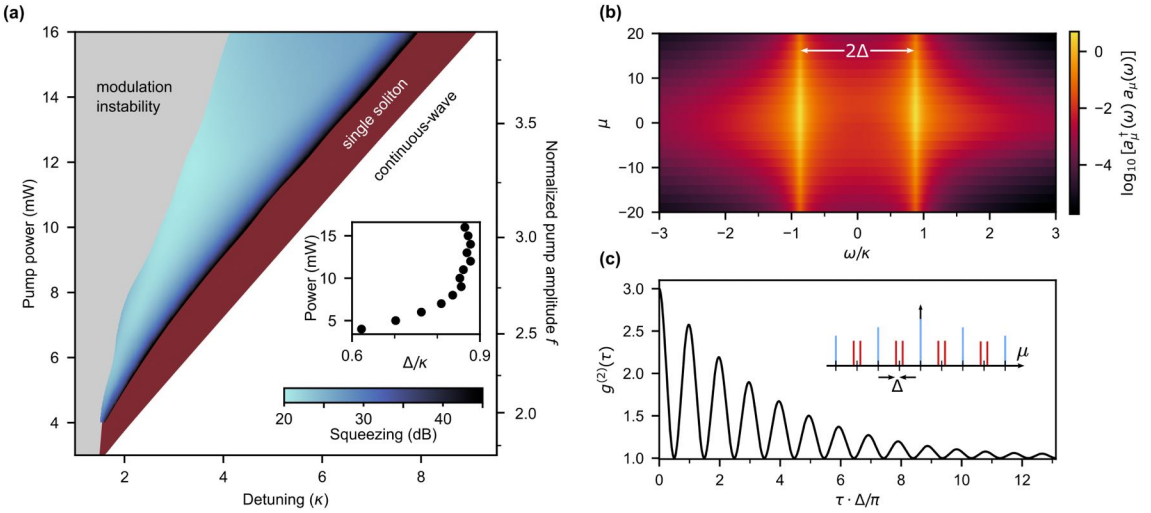


Figure 4.4: **Soliton crystal stability diagram and the quantum twin comb. (a)** A simulated stability chart of the LLE. Power and detuning dependence of the maximum squeezing of the soliton crystal within its existence range is represented by the color gradient. The secondary ordinate axis shows normalized pump amplitude $f$ as defined in Ref. [1]. Inset: Power dependence of the Fourier frequency $\Delta$ of peak squeezing of the near-threshold state. **(b)** The spectral composition of the near-threshold state, showing a prominent light generation in a twin comb structure. **(c)** The second-order autocorrelation $g^{(2)}(\tau)$ for a single resonator mode ($\mu = 1$) reveals the twin-comb signature through a temporal oscillation with period $\pi/\Delta$.

The end of the soliton crystal step is accompanied by asymptotic growth in the squeezing of one supermode, indicating that the dissociation of the soliton crystal state is a coherent threshold process. This can be anticipated from the fact that the passage from the crystallized two-soliton state to the single soliton results in the breaking of $C_2$ symmetry and correspondingly the onset of OPO in the modes $\mu = 1$ (mod 2). In this regard, soliton crystal annihilation is unique among other state transitions, such as one-by-one disappearance of pulses in multi-soliton states [7] and transitions between soliton crystals with defects [66], where symmetry breaking does not occur. The annihilation of the soliton crystal is also the only known example (to our knowledge) of a threshold process that results in a reduction of the mean-field intensity: According to the LLE simulation (Fig. 4.3(d)), one soliton disappears without energy transfer to the other.

As shown in Fig. 4.4(a), the strong squeezing across the step culminating in asymptotic growth is universally present across the soliton crystal existence condition. For all powers, the threshold is reached at a non-zero Fourier frequency $\Delta$ (inset of Fig. 4.4(a)), indicating a strongly detuned threshold process. This is confirmed through calculating the spectral composition of the squeezed vacuum near threshold, which shows that every resonator mode displays a strongly-split spectrum (Fig. 4.4(b)). The near-threshold state is thus composed of twin quantum frequency combs offset by $\Delta$ from the soliton crystal rotating frame. Equal intensities of the twin combs is guaranteed by

energy and momentum conservation. Twin combs would be directly observable in the second-order autocorrelation $g^{(2)}(\tau)$, manifesting as a temporal oscillation with a period of $\pi/\Delta$ (Fig 4.4(c)). The autocorrelation peaks at $g^{(2)}(0) = 3$ and exhibits significant coherence broadening, as expected for near-threshold OPO [33, 46].

A degenerate parametric oscillator reaches parametric oscillation in a continuous process in which damping precludes the formation of a coherent cat state and instead produces a classical mixture of coherent states [38], manifesting as random phase selection of the above-threshold OPO. If the soliton crystal did not exhibit quantum twin comb behavior ($\Delta = 0$) at threshold, the supermode analysis would lend itself to an analogous picture: the post-threshold state is a classical mixture of either one of the soliton pulses disappearing, corresponding to the modes $\mu = 1 \pmod 2$ possessing phase of 0 or $\pi$ with respect to modes $\mu = 0 \pmod 2$. However, since $\Delta \neq 0$, such a simple interpretation is not possible: the passage through threshold must be accompanied by the spectral collapse of the quantum twin comb into a rotating frame. This cannot be explained within the framework of the linearized model, which we show here to predict unbounded growth of twin combs at non-zero $\Delta$. The annihilation of the soliton crystal thus represents a clear opportunity for experimental and theoretical exploration of the breakdown of the linearization assumption in nonlinear Kerr resonators.

## 4.4 Soliton crystal squeezed light source

Until now, we have considered squeezing in the absence of parasitic loss channels—all of the quantum light generated inside the resonator is collected with unity efficiency. While in principle one may realize resonators with an arbitrarily high waveguide-coupling rate relative to the intrinsic loss, peak-efficiency Kerr soliton devices operate near the critical coupling point, which limits the outcoupled squeezing to 3 dB. Soliton operation in the over-coupled regime is associated with a severe increase in the power requirements, as the OPO threshold scales quadratically with resonator losses. For instance, the outcoupling-limited squeezing of 10 dB (15 dB) requires an escape efficiency of 90% (96.8%), and corresponds to an increase of the OPO threshold by 25 (250) times, putting into question the practicality of this approach. In this section, we present a device architecture that overcomes this limitation.

The photonic architecture based on a 2-FSR soliton crystal is shown in Fig. 4.5(a). The proposed device consists of the *squeezing resonator*, engineered for anomalous dispersion to support soliton formation, and critically-coupled to the bus waveguide ($\kappa_i = \kappa_c = \kappa/2$) for efficient in-coupling of the pump. The *auxiliary resonator* is designed to have a free-spectral range twice larger than that of the squeezing resonator, and its modes overlap in frequency with the odd ($\mu = 1 \pmod 2$) azimuthal modes of the squeezing resonator. The auxiliary resonator is strongly over-coupled to the drop waveguide (coupling rate $\kappa_{\text{aux}} \gg \kappa_i$), and is coupled to the squeezing resonator with strength $J$ such that $\kappa_{\text{aux}} \gg J > \kappa$. This corresponds to the regime known in cavity quantum electrodynamics

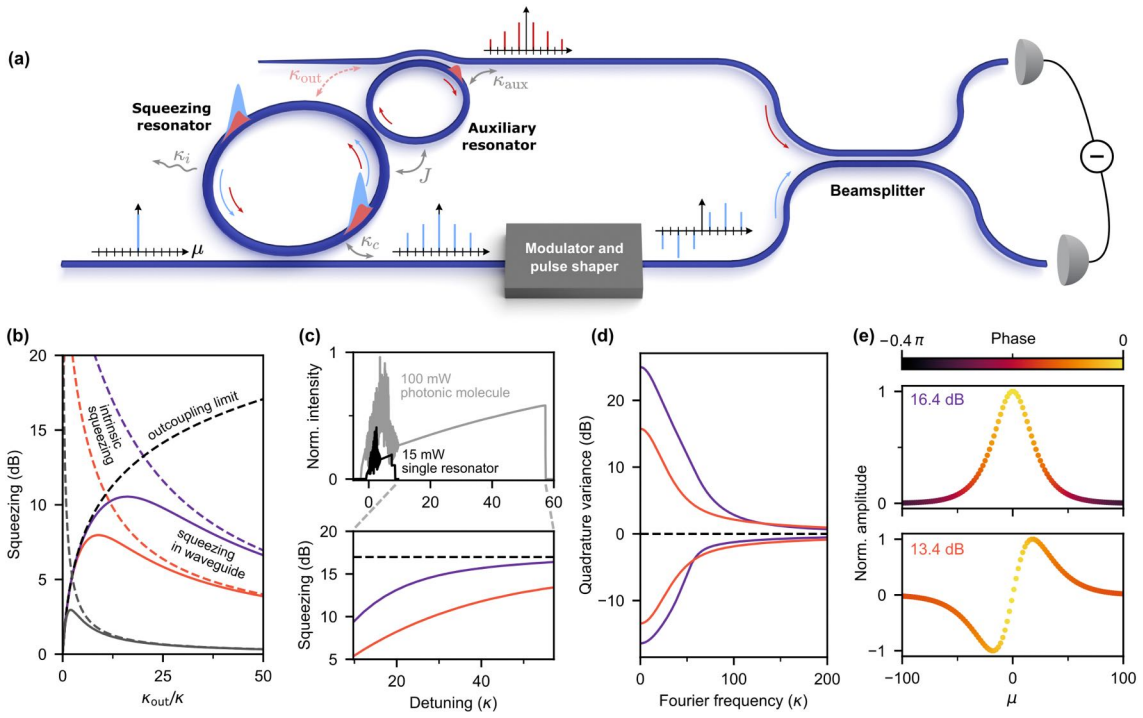


Figure 4.5: **Practical highly-squeezed multimode source (a)** A schematic of the photonic architecture for squeezed light generation and measurement. **(b)** Magnitude of squeezing extracted from the resonator as a function of outcoupling efficiency. The total outcoupled squeezing for the first (second) supermode is shown in solid purple (orange). It is bounded by the intrinsic squeezing generated in the resonator (dashed purple and orange lines) as well as the limit $-10\log(1-\kappa_{\text{out}}/(\kappa_{\text{out}}+\kappa))$ set by the extraction efficiency (dashed black line) , where $\kappa$ is the total loss of the resonator modes in absence of the auxiliary ring. Grey solid (dashed) lines represent the outcoupled (intrinsic) squeezing from a near-threshold mode driven by a single-mode pump. **(c)** Top: LLE simulation of soliton crystal generation for $\kappa_{\text{out}}/\kappa = 50$ at 100 mW input power (gray). Simulation for the case $\kappa_{\text{out}} = 0$ with a 15 mW pump (*i.e.*, the maximum power at which the soliton crystal capture is deterministic [8]) is shown for comparison in black. Bottom: Squeezing in the waveguide along the soliton crystal step. Dashed line represents the outcoupling limit. **(d)** (Anti-) squeezing spectrum in the waveguide at the end of the step. **(e)** Local oscillators for the maximally-squeezed supermodes, with measurable squeezing of 16.4 dB and 13.4 dB.

as Purcell enhancement: the odd modes of the squeezing resonator are coupled to the auxiliary resonator and experience a decay rate ($\kappa_{\text{out}}$) into the drop waveguide. If the magnitude of Purcell enhancement ($\kappa_{\text{out}}/\kappa_i$) is well below the finesse $\mathcal{F}$ of the squeezing resonator (typical $\mathcal{F}$ is $10^3 - 10^4$), the even modes in the squeezing resonator are unaffected by the auxiliary resonator. Thus, rather than disturb the formation of the soliton crystal, the auxiliary ring stabilizes its formation through the suppression of undesirable OPO processes. The choice of $J$ and $\kappa_{\text{aux}}$ thus provides control over the outcoupling rate of the below-threshold modes without negatively impacting the above-threshold

state.

The magnitude of squeezing in the drop waveguide as a function of $\kappa_{\text{out}}/\kappa$ is shown in Fig. 4.5(b). The squeezing calculation in presence of loss is presented below. In the regime of small $\kappa_{\text{out}}$, the squeezing is limited by the outcoupling efficiency into the drop waveguide, and increases with $\kappa_{\text{out}}$. The intrinsic squeezing, however, drops with increasing $\kappa_{\text{out}}$, since the classical soliton crystal state remains unchanged and thus results in weaker effective drive and increased distance to threshold. In the regime where $\kappa_{\text{out}}$ dominates other losses, the outcoupled squeezing is limited by the intrinsic squeezing of the system.

The same conditions responsible for the formation of the twin quantum frequency combs near the soliton crystal annihilation threshold also provide resilience of the squeezing strength against the addition of the outcoupling rate $\kappa_{\text{aux}}$, rendering the soliton crystal an attractive source of squeezed light. This is illustrated by contrast with the squeezing of a typical, non-detuned squeezed source (Fig. 4.5(b)). Ramping up $\kappa_{\text{out}}$ without altering the pump power, the maximum outcoupled squeezing is $\approx 3$ dB at $\kappa_{\text{out}} = 2\kappa$, beyond which it rapidly decays. In contrast, the peak outcoupled squeezing of the below-threshold soliton crystal state reaches its maximum of 10 dB at $\kappa_{\text{out}} = 20\kappa$. The resilience of squeezing to added losses is the consequence of the detuning of the squeezing process: the broadening of the below-threshold modes associated with growing $\kappa_{\text{out}}$ reduces the effective drive strength but simultaneously reduces the loss-normalized detuning of the below-threshold modes with respect to the pump modes. The detuning thus acts as a "squeezing strength" reservoir, and the auxiliary resonator enables the extraction of 10 dB of outcoupled squeezing without increasing the pump power.

We have so far described the effect of the auxiliary resonator while holding constant the power of the pump laser. Since, as noted above, the auxiliary resonator stabilizes the soliton crystal state, the state can be synthesized in the squeezing resonator at much higher pump power to achieve squeezing levels limited by the escape efficiency. We illustrate this in Fig. 4.5(c) for escape efficiency $\eta = 0.98$ ($\kappa_{\text{out}} = 50\ \kappa$), which corresponds to the outcoupling-limited squeezing of $\approx 17$ dB in the waveguide. In this condition, the soliton crystal may be captured with a 100 mW pump, over a greatly-extended detuning range. The outcoupled squeezing grows steadily along the soliton crystal step (consistent with the growing above-threshold comb power), asymptotically approaching the outcoupling limit.

A few additional characteristics of the photonic molecule architecture, as they pertain to the realization of a practical highly-squeezed multimode source, are worth noting:

*Construction of the local oscillator:* The photonic molecule conveniently separates the squeezed vacuum and the above-threshold soliton crystal into separate waveguides. The latter may then be manipulated independently of the squeezed light to construct the local oscillator. Since the temporal bandwidth of the generated squeezed vacuum matches closely that of the above-threshold modes, the local oscillator may be readily generated by first electro-optically interleaving [74] the above-threshold soliton crystal, followed by pulse-shaping the resulting state to retain coherent light with

the phases and intensities corresponding to the desired supermode. This process is illustrated in Fig. 4.5(a). The entirety of the local oscillator preparation may be implemented on-chip, with the recent advances in on-chip electro-optic frequency comb generation [75], low-loss phase-shifting [76], and, if necessary, amplification [77].

*Squeezing bandwidth:* While the above-threshold modes have linewidths on the order of 100 MHz (enabling low-power OPO and the formation of the soliton crystal), the bandwidth of the squeezed light is dictated by the total linewidth of the below-threshold modes, and thus is magnified by a factor of $\kappa_{\text{out}}/\kappa$. The photonic molecule thus may be used to generate squeezed light of bandwidth potentially much greater than that of the squeezing resonator (Fig. 4.5(d)). The local oscillator compositions corresponding to the maximum squeezing at $\omega = 0$ in Fig. 4.5(d) are shown in Fig. 4.5(e).

*Fourier frequency of maximal squeezing:* A local oscillator with optimal squeezing may be prepared in the corresponding supermode as long as $U(\omega)$ is real. However, this is only guaranteed for $\omega = 0$. In the case where $U(\omega)$ is complex, a local oscillator stationary in the rotating frame cannot be used to measure the maximum squeezing [65]. However, for $\kappa_{\text{out}} \gg \kappa$, maximum squeezing shifts to $\omega = 0$, because the loss-normalized system detunings are reduced. This fortuitously renders the squeezing in the photonic molecule configuration amenable to the straightforward local oscillator measurement.

### 4.4.1 Fixed local oscillator in the presence of parasitic loss

We model non-unity waveguide escape efficiency $\eta$ via the addition of a second decay channel, which accounts for all resonator losses other than waveguide coupling:

$$\begin{aligned}\frac{d\hat{a}_\mu(t)}{dt} =& -\left(i\delta_\mu + \frac{\kappa}{2}\right)\hat{a}_\mu(t) \\ &+ ig_0 \sum_{\nu,j,k} \delta[\mu+\nu-j-k] A_j A_k \hat{a}^\dagger_\nu(t) \\ &+ 2ig_0 \sum_{\nu,j,k} \delta[\mu+j-\nu-k] A^*_j A_k \hat{a}_\nu(t) \\ &- \sqrt{\kappa_c}\hat{b}_{\text{in},\mu}(t) - \sqrt{\kappa_i}\hat{d}_{\text{in},\mu}(t)\end{aligned}$$

Now the total cavity decay rate $\kappa = \kappa_i + \kappa_c$ is a sum of the intrinsic decay rate $\kappa_i$ to a second bath (with vacuum operator $\hat{d}_{\text{in},\mu}(t)$) and the decay rate $\kappa_c$ to the output waveguide. To obtain the squeezing in the output waveguide, we evaluate the input-output relation:

$$\hat{b}_{\text{out},\mu}(t) = \hat{b}_{\text{in},\mu}(t) + \sqrt{\kappa_c}\hat{a}_\mu(t)$$

In Fourier space, the output operators can be directly mapped to the input operators[46] via $n \times 2n$ transfer matrices $N(\omega)$ and $M(\omega)$:

$$\hat{b}_{\mathrm{out},\mu}(\omega) = \sum_{k=1}^{n}\Big[N_{\mu,k}(\omega)\hat{b}_{\mathrm{in},k}(\omega) + N_{\mu,k+n}(\omega)\hat{b}^{\dagger}_{\mathrm{in},k}(-\omega) + M_{\mu,k}(\omega)\hat{d}_{\mathrm{in},k}(\omega) + M_{\mu,k+n}(\omega)\hat{d}^{\dagger}_{\mathrm{in},k}(-\omega)\Big]$$

To calculate the noise variance spectrum for an arbitrary local oscillator, we can define a supermode decay operator

$$\hat{L}(t) = \sum_{j} \alpha_j \hat{a}_j(t)$$

whose Hermitian conjugate creates a photon in a superposition of longitudinal modes across the frequency comb, where $\alpha_j = |\alpha_j|e^{i\phi_j}$ defines the amplitude and phase composition of the supermode. Its associated supermode input-output operators are

$$\hat{L}_{\mathrm{in}}(t) = \sum_{j} \alpha_j \hat{b}_{\mathrm{in},j}(t)$$

and

$$\hat{L}_{\mathrm{out}}(t) = \sum_{j} \alpha_j \hat{b}_{\mathrm{out},j}(t).$$

The corresponding Hermitian quadrature operators of $\hat{L}_{\mathrm{out}}$ are:

$$\hat{L}^{(+)}_{\mathrm{out}}(t) = \hat{L}^{\dagger}_{\mathrm{out}}(t) + \hat{L}_{\mathrm{out}}(t)$$

$$\hat{L}^{(-)}_{\mathrm{out}}(t) = i(\hat{L}^{\dagger}_{\mathrm{out}}(t) - \hat{L}_{\mathrm{out}}(t))$$

The noise variance is then defined as

$$V^{(\pm)}(\omega) = \int_{-\infty}^{\infty} d\tau \langle \hat{L}^{(\pm)}_{\mathrm{out}}(t)\hat{L}^{(\pm)}_{\mathrm{out}}(t+\tau)\rangle e^{i\omega\tau},$$

and is computed by applying the commutation relations:

$$\left\langle \hat{b}_{\mathrm{in,i}}(\omega)\hat{b}^{\dagger}_{\mathrm{in,j}}(\omega')\right\rangle = \delta_{ij}\delta(\omega-\omega')$$

$$\left\langle \hat{b}^{\dagger}_{\mathrm{in,i}}(\omega)\hat{b}_{\mathrm{in,j}}(\omega')\right\rangle = 0$$

$$\left\langle \hat{d}_{\mathrm{in,j}}(\omega)\hat{b}^{\dagger}_{\mathrm{in,j}}(\omega')\right\rangle = 0$$

The maximally-squezed supermodes can be obtained from the columns of $U(\omega)$, which defines the linear combination of quadratures $(x_1(t), ..., x_n(t)|y_1(t), ..., y_n(t))^T$ for a given supermode. When

$U(\omega)$ is real, then the composition for the $k$th maximally-(anti)squeezed supermode at $\omega$ may be written:

$$|\alpha_j| = \sqrt{U(\omega)_{j,k}^2 + U(\omega)_{j+n,k}^2}$$

$$\phi_j = \text{atan2}\left(U(\omega)_{j+n,k}, U(\omega)_{j,k}\right)$$

## 4.5 The rotating frame of the soliton crystal

In this Chapter we consider only time-independent states (*i.e.*, when the coefficients $A_m$ in the Hamiltonian are constant). Here, we describe the process for entering the appropriate rotating frame for the soliton state. Figure 4.6 shows free-evolution of the mean-field of two states: the primary comb and the 2-FSR soliton crystal state. For the primary comb, the solution is seen to be stationary in time. Thus, to compute supermodes for this state, no additional transformation is required. In contrast, a soliton crystal state is precessing in time [8]. This can be understood as the mismatch between the $D_1$ of the resonator and the repetition rate of the soliton, determined by the group velocity of the soliton state. Thus, in order to enter the rotating frame where the soliton is stationary, we evolve the soliton state in time, extracting the rate of phase accumulation of each mode, and apply a rotating frame correction accordingly.

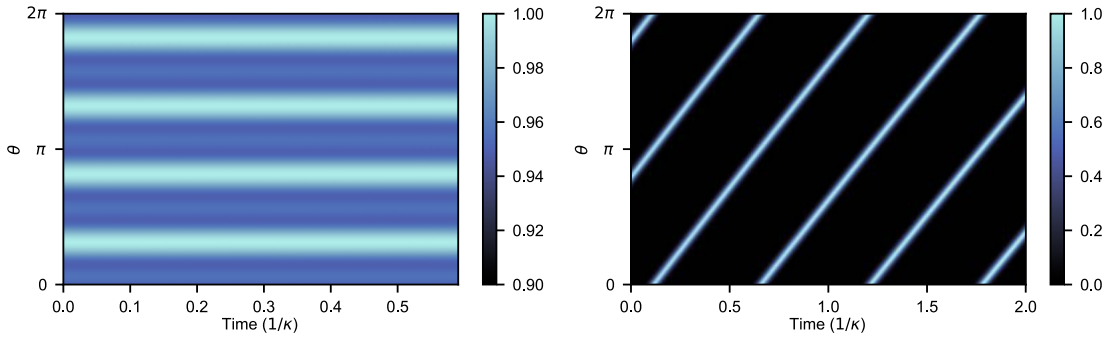


Figure 4.6: **Mean-field evolution of stationary and precessing solutions to the LLE. Left:** Time evolution of the primary comb field intensity (reproduced from Fig. 4.2(b)). The state can be seen to be time-independent in the the rotating frame of the first-order dispersion parameter $D_1$. **Right:** The time evolution of the 2-FSR soliton crystal state field intensity. The state is not time-independent due to precession in the $D_1$ rotating frame.

## 4.6 Squeezed supermodes of a 7-FSR soliton crystal

Application of the squeezed supermode decomposition to higher-order soliton crystal states ($N$ circulating pulses) results in $(N-1)$ orthogonal supermodes for each quasi-HG order. For instance,

a 7-FSR crystal features six quasi-$HG_0$ and six quasi-$HG_1$ supermodes of nearly-identical squeezing levels. Figure 4.7 shows the supermode decomposition for a soliton crystal without all-to-all connectivity. Unlike the 2-FSR soliton crystal, formation of quasi-degenerate supermodes is observed, due to the subgroups of internally all-to-all coupled modes as dictated by the Hamiltonian. Thus, the squeezing spectrum of a soliton crystal source can be tailored beyond two prominent supermodes. However, the pattern of symmetry breaking in the annihilation of higher-FSR soliton crystals is expected to be qualitatively different, as multiple pulses (and thus multiple decay pathways) are present.

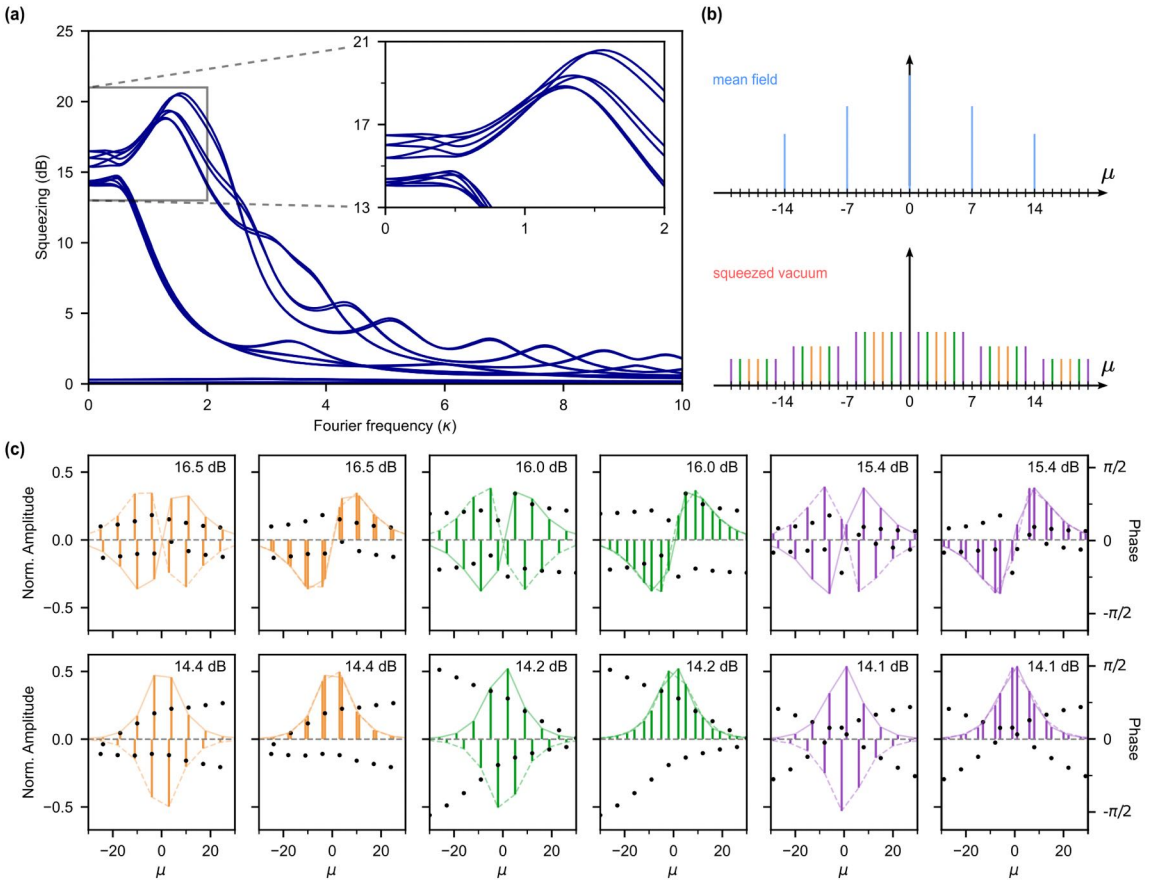


Figure 4.7: **Supermode decomposition of a 7-FSR soliton crystal. (a)** The squeezing eigenspectrum of a 7-FSR soliton crystal, showing a total of 12 strongly-squeezed supermodes. **(b)** Illustration of the mean-field soliton crystal state, comprising coherent light in modes $\mu = 0$ (mod 7), and and the squeezed vacuum, forming three independent subsets of modes (orange, green, purple) as dictated by the four-wave mixing mode-matching condition. **(c)** Local oscillators (LO) at zero Fourier frequency. The vertical lines (orange, green, purple) represent amplitudes of each constitutent frequency basis mode. The supermode envelope is illustrated in light solid and dashed lines. The black dots represent phase of each constituent frequency basis mode. The squeezing value of the supermode at $\omega = 0$ is noted in the top right corner.

# Part II

# Silicon carbide-on-insulator photonics

# Chapter 5

# Introduction

In the quantum optics studies of the preceding Chapters, the experiments utilize silicon carbide-on-insulator (SiCOI) integrated photonics as the nonlinear platform. SiC possesses attractive material properties for nonlinear optics, including substantial second- and third-order nonlinearities ($\chi^{(2)}$ and $\chi^{(3)}$), a large bandgap (3.2 eV, which allows SiC photonics to cover the entire visible spectrum), optical transparency past 5 um, and a moderately high linear refractive index ($n = 2.6$) which allows for a good confinement within cladding materials such as silica ($n = 1.44$) and air. Importantly, SiCOI is CMOS compatible, which is attractive for the prospect of scalable quantum and nonlinear systems. Additionally, silicon carbide hosts optically-addressable spin defects in its crystalline lattice, which opens up the possibility to combine nonlinear optics with cavity quantum electrodynamics. In this Part II of the thesis, I will describe demonstrations in classical nonlinear optics using high-quality SiCOI photonics, which also enabled the experimental demonstrations described in Part I.

Wafer-scale growth and processing of 4H and 6H polytypes of SiC was developed in the 1990's for applications in high-power electronics. Soon after, 4H- and 6H-SiC-on-insulator (SiCOI) were demonstrated [78] using the same ion-implantation (Smart-Cut) method that is used to produce silicon-on-insulator (SOI) wafers. This technology enabled the first demonstration of photonic crystal cavities (PhCs) in SiC [11, 79] (Fig. 5.1). As the development of photonics in Smart-Cut 4H-SiC continued [80] and Smart-Cut SiCOI became optimized on a wafer-scale [81], the intrinsic optical absorption of the SiC thin films was identified as the limiting factor for high-Q SiC photonics, limiting waveguide losses to $> 5$ dB/cm [82]. Although further optimization of the implantation conditions may remedy the low material quality [80], it is unclear whether the Smart-Cut method is suitable for producing films of SiC with the same nearly-pristine crystal quality as silicon-on-insulator. The difference between Smart-Cut SOI and SiCOI stems from the drastically different thermal properties of silicon and SiC: The lattice of silicon will soften and heal at the modest temperatures achievable in standard quartz furnaces. SiC, in turn, is one of the most refractory materials, subliming at 2700°C.

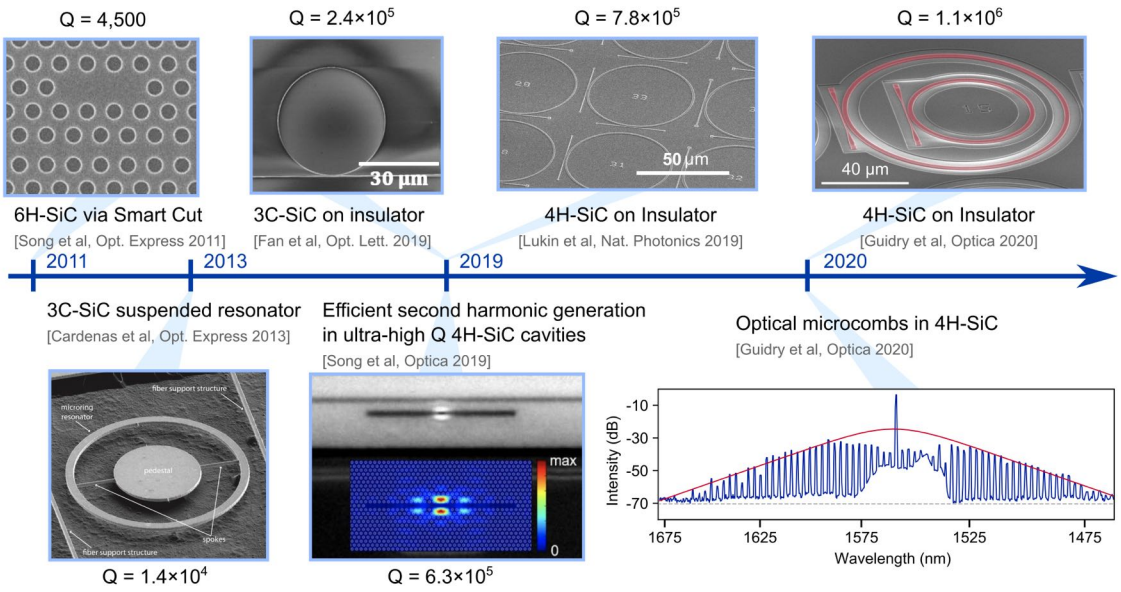


Figure 5.1: **Timeline of SiC photonics development.** First demonstration of SiC photonic device using the Smart Cut approach with 6H-SiC [11]. Soon after, suspended resonators in 3C-SiC-on-Si were demonstrated [12]. Strong intrinsic absorption of low quality Smart Cut and heteroepitaxial 3C films was hypothesized to limit the achievable Q-factors. Using thicker 3C-SiC epilayers or thinning down bulk-crystal 4H-SiC, enabled record Q factors in 3C-SiC [13, 14], ultra-high Q PhCs [15], and low-loss 4H-SiC-on-Insulator waveguides [16]. Recently, devices with Q factors exceeding $10^6$ were shown, enabling the demonstration of optical parametric oscillation and microcomb formation [10]. This figure is reprinted from Ref. [17]: individual figures are reproduced from [11, 12, 14, 15, 16, 10]

Repairing the lattice in post-processing without destroying the substrate is thus likely impossible.

Another approach to SiC photonics took advantage of the heteroepitaxial growth of 3C-SiC films on silicon. A variety of 3C-SiC-on-Si photonics devices have been demonstrated, including PhCs [12, 83] and whispering-gallery-mode resonators [84]. However, this approach also suffers from substantial intrinsic material absorption, due to the high density of crystal defects near the growth interface caused by the Si-SiC lattice mismatch. Recently, a technique based on film transfer and back-side polishing introduced the 3C-SiC-on-insulator platform and enabled waveguides with losses down to 1.5 dB/cm, still likely limited by material absorption [13, 14].

Leveraging the wafer-scale production of 4H-SiC and the advanced grinding and polishing equipment developed for processing it, a method for fabricating "quantum-grade" 4H-SiC-on-insulator was recently introduced [16]. This method enables 4H-SiCOI substrates with the same crystalline quality as bulk SiC crystal. Using 4H-SiCOI produced this way, ultra-high quality (Q) factor PhCs ($Q = 6.3 \times 10^5$) have been fabricated [15]. 4H-SiCOI also enabled quantum photonic devices with single color centers in a CMOS compatible architecture [16]. Unfettered by the material absorption limit of previous approaches, integrated SiC photonics with propagation loss below 5 dB/m have

become possible. As detailed in Chapter 7, low-loss microring resonators were used to demonstrate optical parametric oscillation and microcomb formation [10], establishing SiC as a promising material for integrated nonlinear photonics. In the same Chapter, we measure the intrinsic absorption of 4H-SiC to be as low as 2 dB/m in an unoptimized sublimation-grown sample [10], indicating that integrated photonics in SiC with Q factors of at least $10^7$ are possible.

# Chapter 6

# Resonant second-order nonlinear photonics

One of the main attractions of SiC is its moderately-strong second-order optical nonlinearity ($\chi^{(2)}$). In non-centrosymmetric crystals, second-order nonlinear processes typically are several orders of magnitude stronger than third-order processes in similar structures. This allows in principle for significantly more power efficient nonlinear photonics technologies, including quantum frequency conversion [85], optical parametric oscillation [86], and spectral translation [87]. In SiC, the prospect of monolithically combining this second-order nonlinearity with Kerr solitons for visible combs [87], supercontinuum generation for self-referencing [88], and optically-addressable spin qubits for quantum frequency conversion [89], motivate its exploration. In this Chapter, we focus on second-order processes with resonant enhancement via an integrated photonic resonator, relevant for the first two applications. In Chapter 9, we will return again to second-order nonlinear light generation in the context of supercontinuum generation in SiC waveguides.

4H-SiC is a non-centrosymmetric crystal with the point group of 6mm, $C_{6v}$. Measured at 1 µm [90], the second-order nonlinear tensor has three independent elements:

$$d_{33} = -11.7 \text{ pm/V}$$
$$d_{31} = 6.5 \text{ pm/V}$$
$$d_{15} = 6.7 \text{ pm/V}$$

The strongest term with field polarizations along the optical axis is about a factor of three less than lithium niobate. In comparison to modal phasematching, it is relevant to note that the effective nonlinearity of periodically-poled photonics is reduced by a factor of $2/\pi$ due to the quasi-phase matching condition [91] (although the near-perfect mode overlap and reduced propagation losses

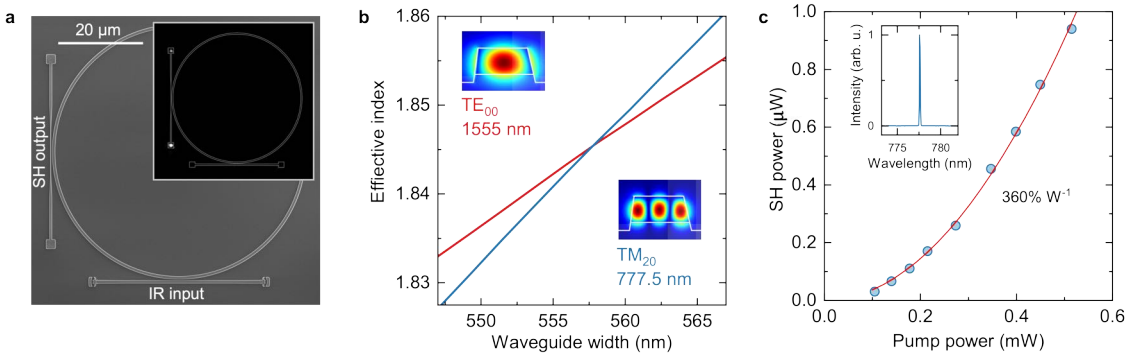


Figure 6.1: **Second-order frequency conversion in microring resonators.** **a** SEM of a ring resonator designed for second-harmonic generation. The fundamental $TE_{00}$ mode at 1555 nm is converted to a $TM_{20}$ mode at 777.5 nm, and coupled out via a single-mode, effective index-matched waveguide. Inset: Optical image of the second-harmonic out-coupled via an inverse-designed vertical coupler (ring outline is overlaid for clarity). **b** Numerical simulation of the phase-matching condition for the 1555 nm $TE_{00}$ and the 777.5 nm $TM_{20}$ modes, demonstrating mode-matching for a waveguide width of 560 nm. Insets: Simulated mode profiles. **c** Dependence of second-harmonic power in the output waveguide on the pump power in the input waveguide. A quadratic fit reveals a conversion efficiency of 360% $W^{-1}$. Inset: The second-harmonic signal imaged on a spectrometer, where linewidth is spectrometer-limited.

significantly improve the efficiency).

In this brief Chapter, we describe details for design and experimental demonstration of doubly-resonant second-harmonic generation in 4H-SiCOI microring resonators, reproduced from [16]. We then extend our analysis for the prospect of triply-resonant quantum frequency conversion from spin qubit emission wavelengths in the near-infrared into the telecommunications band.

## 6.1 Second-harmonic generation

Here, we demonstrate doubly-resonant second-harmonic generation using modal phase-matching in a microring resonator (Fig. 6.1a). Towards this end, we design the dimensions of the ring to induce geometric dispersion to balance the intrinsic material dispersion and allow for phase-matching across a wide frequency separation. To utilise the $d_{31}$ nonlinear term in c-cut 4H-SiC, we design for phase-matching between the fundamental quasi-transverse-electric mode ($TE_{00}$) at 1555 nm and a quasi-transverse-magnetic mode $TM_{20}$ at 777.5 nm. Finite-element method simulation using anisotropic Sellmeier equations [92] for air-clad 4H-SiC shows that effective refractive index matching is possible between these modes for a waveguide thickness of 350 nm, a waveguide width of 560 nm, and a microring radius of 27.5 µm (see Fig. 6.1b). Two bus waveguides are designed to selectively point couple either the pump or second harmonic, each equipped with inverse-designed grating couplers [93] optimised for the appropriate wavelength (see Fig. 6.1a). Via transmission measurements through

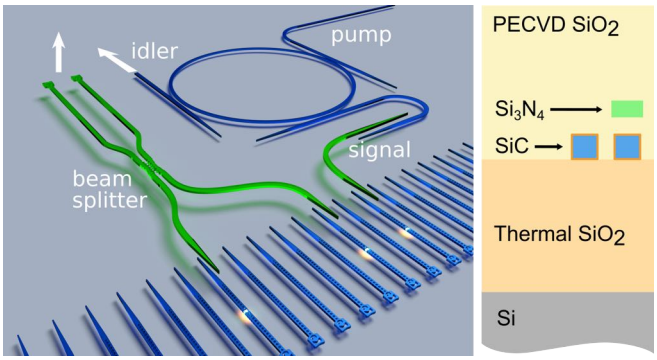


Figure 6.2: **Potential for two-layer heterogeneous integration.** A conceptual diagram showing two applications that can be implemented with the 4H-SiCOI architecture. **a** On the left, the realisation of spin-spin entanglement scheme between two emitter-cavity systems. On the right, emission from a single spin defect is delivered to a triply-resonant ring resonator to achieve frequency conversion to the telecommunication frequencies. Although for maximum circuit efficiency it is best to forgo silicon nitride interconnects, this approach may enable short term multi-qubit integration until near-unity single-qubit yield is attained **b** Material stack illustration for the proposed platform.

each bus waveguide at the respective design wavelength, we measure loaded Q factors of $8 \cdot 10^4$ for the pump at near-critical coupling and $2 \cdot 10^4$ for the second harmonic, undercoupled with a transmission of $T = 0.5$. The devices were designed to be compatible with air-clad inverse-designed vertical couplers. By varying the pump power, we obtain a linear power dependence of the SHG with the square of the pump power, as expected in the undepleted pump limit (see Fig. 6.1c). The SHG efficiency is defined as the ratio between the generated second-harmonic power in the output waveguide versus the square of the pump power in the input waveguide. The efficiency of our SHG process is measured to be 360% $\mathrm{W}^{-1}$.

The efficiency of second harmonic generation in a doubly resonant cavity may be derived using temporal coupled mode theory [94]. At low input powers in the undepleted pump limit (marked by a quadratic dependence of output power $P_2$ on input power $P_1$), the second harmonic conversion efficiency is given by

$$\frac{P_2}{P_1^2} = 32 \frac{Q_1^4 Q_2^2}{Q_{1,c}^2 Q_{2,c}} \frac{|\beta|^2}{\omega_1}$$

where $\omega_1$ is the frequency of the pump ($\omega_2 = 2\omega_1$), $\beta$ is the cavity mode coupling factor, and $Q_k$ is the total $Q$ of the $k$th cavity mode, described by $\frac{1}{Q_k} = \frac{1}{Q_{k,c}} + \frac{1}{Q_{k,i}}$ where $Q_{k,c}$ is proportional to the decay rate into the output waveguide and $Q_{k,i}$ is proportional to the loss rate due to all other loss channels (including material absorption). Via transmission measurements through each bus waveguide at the respective designed wavelength (assuming that coupling into the non-designed bus waveguide for a given wavelength is negligible), we measure $Q_1 = 8.5 \cdot 10^4$, $Q_{1,c} = 1.3 \cdot 10^5$,

$Q_2 = 3.5 \cdot 10^4$, and $Q_{2,c} = 2.3 \cdot 10^5$. The $\beta$ used here is derived via perturbation theory to be [94, 95]

$$\beta = \frac{1}{4} \frac{\int d^3x \epsilon_0 \sum_{ijk} \chi^{(2)}_{ijk} E^*_{1i} (E_{2j} E^*_{1k} + E^*_{1j} E_{2k})}{\int d^3x \epsilon |E_1|^2 \sqrt{\int d^3x \epsilon |E_2|^2}}$$

where $i, j, k \in \{x, y, z\}$, $\chi^{(2)}$ is the second-order nonlinearity of the material ($\chi^{(2)}_{ijk} = 2d_{ijk}$), and $E_{lm}$ represents the electric field component polarized along $m$ of the $l$th mode. The permittivity is $\epsilon$, where $\epsilon_0$ is the vacuum permittivity. Using a finite-element method simulation, we solve for the mode profiles in a curved waveguide at the relevant wavelengths (see Fig. 6.3) and use them to calculate $|\beta| = 4\ \mathrm{J}^{-1/2}$. Using the above model, the theoretical efficiency of our SHG process is approximately 700% $\mathrm{W}^{-1}$. This discrepancy is likely a result of nonuniformity in the microring waveguide dimensions at different azimuthal angles, which degrades overall phase-matching [96]. With improved Q-factors and optimized fabrication techniques, the conversion efficiency may be significantly improved.

### 6.1.1 Other demonstrations

This Chapter describes the first demonstration of doubly-resonant second-harmonic generation (SHG) in SiC photonics. Efficient singly-resonant SHG has also been demonstrated in photonic crystal cavities at telecommunications wavelengths [15, 79], enabled by the very high quality factor-to-mode volume ratio. In a microdisk resonator [87] and an inverse-designed Fabry-Perot resonator [97], chaotic Kerr combs have been spectrally translated from near-infrared and infrared to visible wavelengths. Simultaneous second-harmonic generation and supercontinuum generation have been observed in SiC waveguides [98] (Chapter 9).

## 6.2 Quantum frequency conversion

Photons are necessary as flying qubits in quantum information processing for long-distance communications and distributed quantum computation. However, the high-transparency window of silica fibers is limited to the 1300 nm and 1550 nm infrared bands, whereas nearly all current solid-state qubit candidates emit at other wavelengths. This has motivated a decade of development in quantum frequency conversion (QFC) technology, with the goal of enabling a quantum network which connects nodes operating at different wavelengths and allows long-distance transport of quantum information.

Quantum frequency conversion of single photons emitted by a color center to telecommunication wavelengths is possible by means of nonlinear second-order difference frequency generation [99], where the emitter ($\omega_e$) and pump ($\omega_p < \omega_e$) photons generate a telecommunication photon ($\omega_T = \omega_e - \omega_p$). A single photon may be converted with high fidelity from $\omega_e$ to $\omega_T$, *i.e.*, the conversion

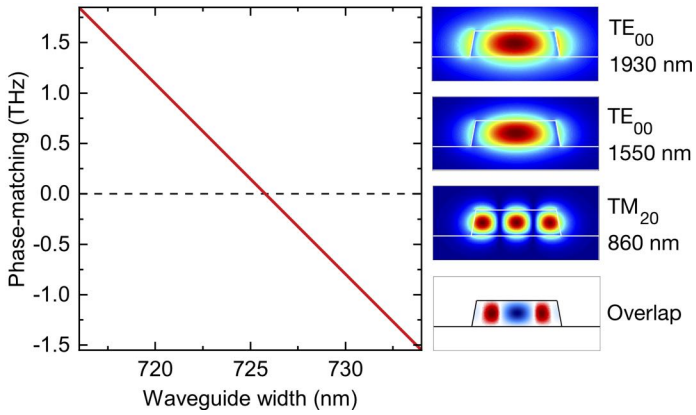


Figure 6.3: **Modal phase-matching for difference-frequency generation. Left** For a waveguide height of 350 nm, sidewall angle of $\theta = 7°$, and radius of 27.5 µm with $SiO_2$ cladding, the phase-matching condition $(n_T\omega_T + n_p\omega_p - n_e\omega_e)/2\pi = 0$ THz is achieved for a waveguide width of 725 nm. **Right** The absolute value of the primary electric field component in the ring cross-section for each mode. The spatial overlap diagram features the real component of $\sum_{ijk} \chi^{(2)}_{ijk} E^*_{1i}(E^*_{2j}E_{3k} + E^*_{2k}E_{3j})$ prior to integrating over the volume.

efficiency is quantum-limited, for a critical pump power

$$P_p = \frac{\omega_p}{16|\beta|^2 Q_e Q_p Q_T \Gamma_p}$$

where $\Gamma_p$ is the ratio of the decay rate into the waveguide over the total decay rate of the pump mode [94]. Using $\lambda_p = 1.93$ um, $\lambda_T = 1.55$ um, $\lambda_e = 860$ nm (corresponding to the silicon vacancy V1 center in SiC [16]) with $\Gamma_p = 0.5$, and $Q_T = Q_p = 2 \cdot Q_e = 5 \cdot 10^5$, we calculate a critical pump power of $P_p = 0.3$ mW. The coupling factor $|\beta| = 2.4$ $J^{-1/2}$ now includes a product of three separate fields [94] and is calculated using simulated pump and telecom TE00 mode profiles and a TM20 mode profile (see Fig. 6.3) at the emitter wavelength, where the waveguide dimensions in a 27.5 um-radius, $SiO_2$-clad microring are designed for phase-matching (*i.e.*, to satisfy the condition $n_e\omega_e = n_T\omega_T + n_p\omega_p$, where $n_k$ is the effective index of the mode with frequency $\omega_k$). This difference frequency process utilizes the same nonlinear term as the SHG process, where the polarization of the $\omega_e$ mode is chosen to match the orientation of the emitter dipole moment.

# Chapter 7

# Optical parametric oscillation

After describing the engineering of the second-order optical nonlinearity of SiC for doubly-resonant second-harmonic generation, we turn to the demonstration of optical parametric oscillation (OPO) in SiC photonics [10]. Unlike SHG, the demonstration of OPO requires significantly lower propagation loss due to the threshold-process nature of the effect. Unlike SHG, which can in principle be observed for arbitrarily low pump powers (provided one has sufficiently sensitive detectors), OPO is a phenomenon that only occurs once a certain gain threshold is met. The power requirement for this threshold scales inversely with the square of the quality factor.

As optical parametric oscillation is a predecessor of dissipative Kerr soliton formation, its first demonstration was an essential stepping stone for soliton generation. On the other hand, on-chip OPO is in its own right useful for technologies such as efficient wideband spectral translation [100] and on-chip generation of non-classical light states [57] (see Chapter 2). Furthermore, the monolithic integration of optical spin defects with a near-threshold OPO light source (*i.e.*, parametric drive) can enable the demonstration of new physical effects in cavity quantum electrodynamics.

In this Chapter, we demonstrate on-chip $\chi^{(3)}$ optical parametric oscillation (OPO) and microcomb formation in high-purity semi-insulating (HPSI) 4H-SiC-on-insulator microring resonators. This is enabled by resonator dispersion engineering, improved fabrication techniques resulting in Q factors as high as 1.1 million, and compact inverse-designed vertical couplers for a broadband, high-efficiency free-space interface. We also perform a careful study of the intrinsic material absorption of SiC, providing crucial information on the dominant sources of loss in high-Q photonic devices based on SiC.

The device fabrication follows the process described in Ref. [16], with modifications to improve the pattern-transfer fidelity and device Q factors. Instead of using HSQ e-beam resist, which suffers from low reactive-ion etching selectivity against SiC, an aluminum hard mask (deposited via evaporation and patterned with ZEP e-beam resist) is used. Combined with a low-power $SF_6$ etch, this yields a hard-mask selectivity of 9 (compared to 2 for HSQ). Using this method, devices in SiC films

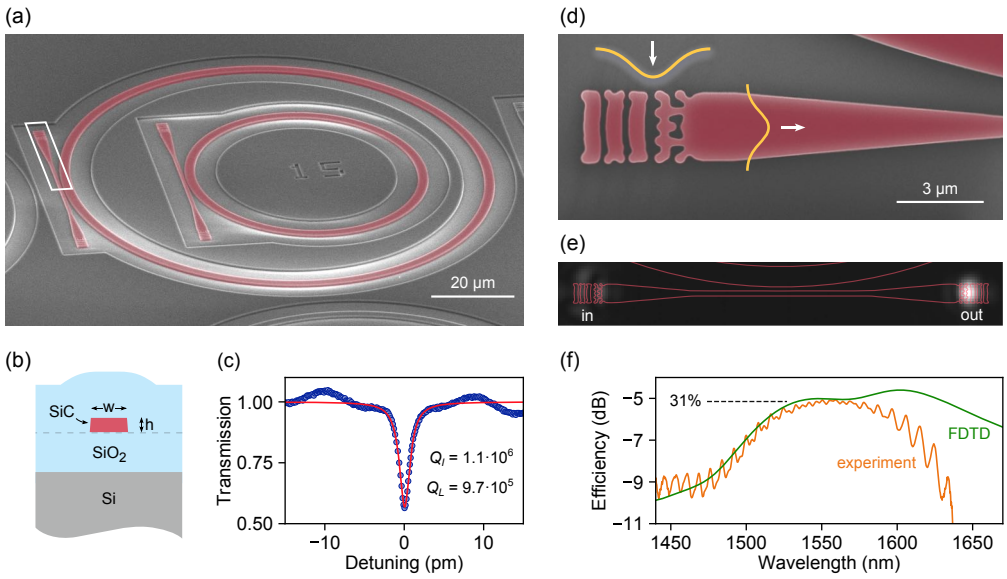


Figure 7.1: **Microring resonators and inverse-designed vertical couplers in 4H-SiC-on-insulator.** (a) A scanning electron micrograph (SEM) of two SiC microring resonators (false-colored) with diameters of 55 µm and 100 µm before $SiO_2$ encapsulation. (b) A schematic of the device cross-section after $SiO_2$ encapsulation. (c) Transmission spectrum of a ring with diameter 100 µm, width 3.0 µm, and height 530 nm, around a $TE_{00}$ resonance with an intrinsic Q of $1.1 \cdot 10^6$ and loaded Q of $9.7 \cdot 10^5$. The wavelength is relative to 1532 nm. (d) A close-up SEM image of the inverse-designed vertical coupler, highlighted in (a). The coupler converts a near-diffraction-limited free-space Gaussian beam (focused via a 50x objective with NA = 0.5) into the fundamental waveguide mode. (e) Camera image of the coupler operating at peak efficiency, showing little back-reflection from the input coupler, and a nearly-Gaussian beam at the output. (f) We measure the single-mode coupling efficiency to be 31% at the target wavelength of 1550 nm, in close agreement with finite-difference time domain (FDTD) simulation.

as thick as 1.5 µm can be fabricated. Figure 7.1a shows microring resonator devices before oxide encapsulation. Q factors as high as $1.1 \cdot 10^6$ are measured (Fig. 7.1c), which corresponds to waveguide loss of 0.38 dB/cm. Routing light to and from the chip is done via efficient and broadband inverse-designed vertical couplers [101, 93], with a peak single-mode coupling efficiency of 31%, as illustrated in Fig. 7.1(d-f). Accurate pattern transfer and high aspect ratio nanostructures enabled by the new fabrication approach were essential for the demonstration of the close agreement between the simulated and measured efficiency at the target wavelength of 1550 nm.

The waveguide loss of 0.38 dB/cm presented here approaches the previously reported upper bound of 0.3 dB/cm on the intrinsic absorption of 4H-SiC [80]. To identify the dominant source of loss in high-Q SiC devices, we perform high resolution characterization of the intrinsic absorption of SiC via photothermal common-path interferometry (PCI), which has been used to detect

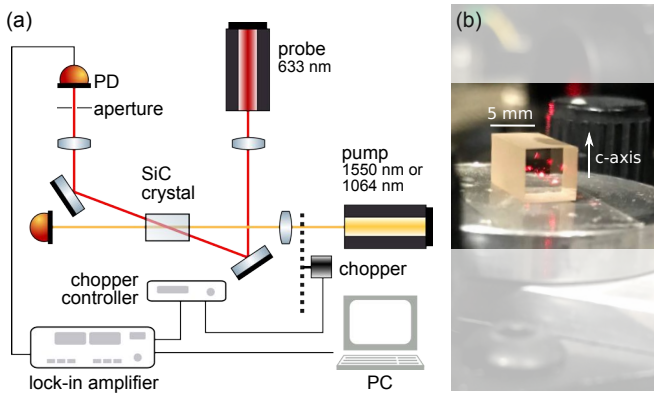


Figure 7.2: **Measurement of the intrinsic loss of 4H-SiC.** (a) Diagram of the PCI measurement setup, described in detail in Ref. [18]. (b) A crystal of 4H-SiC with dimensions of $5 \times 5 \times 10$ mm undergoing the absorption measurement. Multiple reflections of the red probe laser inside the crystal are visible.

absolute absorption down to 1 ppm/cm [18]. In PCI, a low-power probe beam is used to sense the heating effect from the absorption of a high-power pump beam, as shown in Fig. 7.2a. The pump beam, with comparatively smaller waist, is chopped, periodically modulating the heating effect, which induces self-interference of the probe beam via the photothermal effect. We perform absorption measurements on sublimation-grown HPSI 4H-SiC (Shanghai Famous Trade Co. LTD) with resistivity exceeding $10^5$ $\Omega$·m (Fig. 7.2b). The measured absorption is shown in Table 7.1. We note that the absolute accuracy of PCI requires a low-transparency calibration sample or precise knowledge of material properties, including the refractive index, the thermo-optic coefficient, the coefficient of thermal expansion, and the thermal conductivity. Based on previously-reported values of these parameters for 4H-SiC [92, 102, 103, 104, 105], we conservatively estimate the absolute accuracy of the reported values to be $\pm 25\%$. However, the relative precision is within 1%. This allows us to observe wavelength-dependent anisotropy in absorption (3.7 at 1550 nm and 2.0 at 1064 nm). Such strong wavelength-dependent anisotropy suggests that residual crystal defects with polarization-dependent near-IR and telecom absorption [106, 107, 108], rather than the bulk SiC lattice, may be the dominant source of loss; however, further investigation is necessary. Our high-resolution absorption measurements indicate that Q-factors exceeding $10^7$ are possible in SiC. Defect-free epitaxial SiC layers used in quantum technologies [108, 109, 110] may enable photonics with even higher Q factors.

In order to generate degenerate four-wave mixing OPO, one must achieve frequency and phase matching between the pump, signal, and idler modes in the resonator. The frequency matching condition $2\omega_p = \omega_s + \omega_i$ follows from conservation of energy. The phase matching condition ensures

Table 7.1: Intrinsic optical loss of HPSI 4H-SiC

| **Wavelength** | **Polarization** | **Absorption (dB/cm)** |
|---|---|---|
| 1064 nm | $\perp$ c-axis | 0.063 |
| | $\parallel$ c-axis | 0.031 |
| 1550 nm | $\perp$ c-axis | 0.074 |
| | $\parallel$ c-axis | 0.020 |

proper volumetric mode overlap and, for OPO within one mode family of a microring, reduces to the statement of conservation of angular momentum $2\mu_p = \mu_s + \mu_i$, where $\mu$ is the azimuthal mode number [111]. The spectral characteristics of the OPO and subsequent microcomb are determined by the dispersion relative to the pump mode ($\mu_p = 0$)

$$\omega(\mu) = \omega_0 + \sum_{k=1} \frac{D_k}{k!}\mu^k$$

where the $k^{\text{th}}$-order dispersion is $D_k$. Here, $D_1$ is the free spectral range (FSR) of the resonator. When $D_2$ dominates all higher-order terms and is positive (negative), the mode dispersion is said to be anomalous (normal).

We engineer microrings to possess anomalous dispersion in the $TE_{10}$ mode across the telecommunications band for broadband microcomb generation [24]. The dispersion calculations include material anisotropy [92], and are performed in cylindrical coordinates to include the effect of the microring bending radius. For 100 µm diameter microrings, a target height of 530 nm and a width of 1850 nm (with a sidewall angle of 10°) are chosen. To predict the OPO behavior, we obtain a transmission spectrum across the full range of the tunable laser (1520-1570 nm), and extract the dispersion of the $TE_{10}$ mode by measuring the frequencies of the resonances. To measure dispersion with high precision, we rely on a fiber-based Mach Zehnder interferometer, the free spectral range of which is measured using an adaption of the radio-frequency spectroscopy method [112]. Figure 7.3a shows the integrated dispersion $D_{int} = \omega(\mu) - (\omega_0 + D_1\mu)$ with respect to mode number, to visualize all $k \geq 2$ dispersion terms. Numerical simulation of the integrated dispersion for the target microring dimensions is plotted for comparison, showing agreement.

The intrinsic (loaded) Q factor of the $TE_{10}$ mode is measured to be $2.7 \cdot 10^5$ ($1.8 \cdot 10^5$). At the OPO threshold power, primary sidebands emerge at $\mu = \pm 12$. As more power is injected into the microring, a primary comb at the multi-FSR sideband spacing emerges (Fig. 7.3b). At 75 mW, spectrally-separated sub-combs are formed around the primary lines. At the maximum injected power, the sub-combs fill out and interfere around the pump, which is evidence of chaotic comb generation [24]. The thermo-optic effect we observe in our devices may require the use of active capture techniques [113] for soliton formation, and lithographic control of device structure

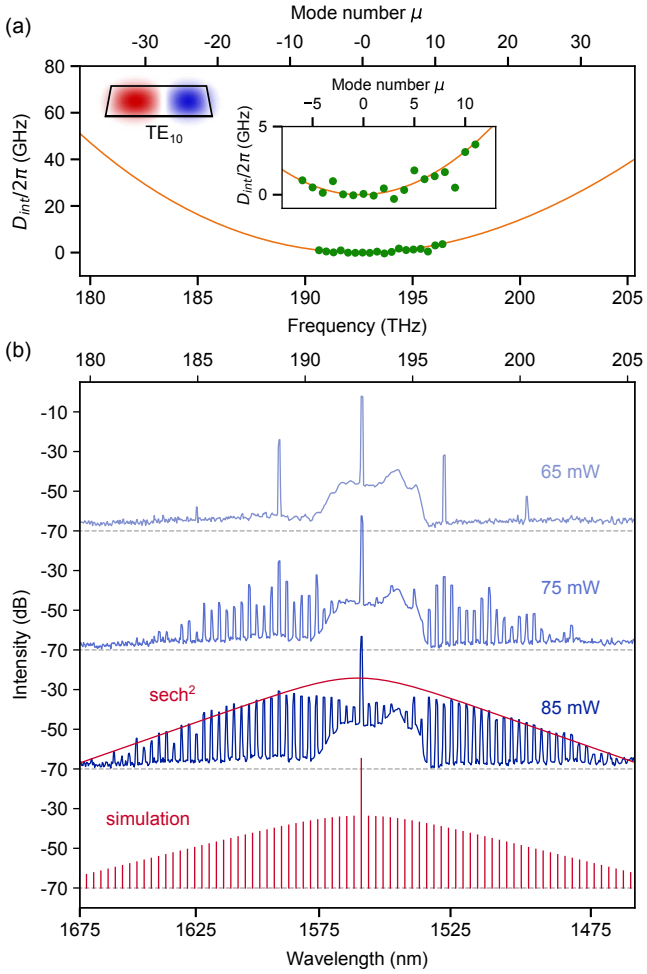


Figure 7.3: **Microcomb formation in a 4H-SiC microring.** (a) Measured integrated dispersion (green points) of the $TE_{10}$ mode versus the relative mode number $\mu$, where $\mu = 0$ corresponds to the pump mode. The orange curve is a numerical simulation, from which we extract $D_2/2\pi = 61$ MHz and $D_3/2\pi = -0.01$ MHz. Center inset: Close-up of the measured dispersion datapoints. Left inset: Numerical simulation of the $TE_{10}$ mode cross-section. (b) Measured OPO spectra (blue) at different injected powers, featuring three distinct stages in the microcomb formation. A $\text{sech}^2$ fit (red envelope) is overlaid onto the chaotic frequency comb for comparison to the characteristic soliton spectral shape. Simulation (red) of the soliton frequency comb.

can eliminate avoided mode crossings, which may otherwise impede soliton capture. Using the experimental parameters of our device, we simulate the soliton frequency comb using the Lugiato-Lefever equation [23], neglecting Raman and $\chi^{(2)}$ effects. The simulated soliton is shown in the last plot in Fig. 7.3b.

Finally, we measure the OPO power threshold in our devices and use it to determine the nonlinear

refractive index ($n_2$) of 4H-SiC. The power threshold of the OPO is defined as the power injected into the pump mode at which the primary sideband emerges. This threshold is determined by the loss and the confinement of the three modes

$$P_{th} = \frac{\omega_0 n^2}{8\eta n_2 c} \frac{V}{\sqrt{Q_{L,s} Q_{L,i}} Q_{L,p}} \tag{7.1}$$

where $n$ is the modal refractive index, $V$ is the mode volume, and $\eta = Q_{L,p}/Q_{c,p}$ where $Q_{c,p}$ accounts for coupling losses from the pump mode to the waveguide [100]. In this demonstration, we use the $TE_{00}$ mode of a 55 µm diameter ring resonator with the same cross-section as before. Although the dispersion is normal for the fundamental TE mode, pumping at an avoided mode crossing allows us to achieve frequency matching [114] and to generate OPO, while benefiting from the higher quality factors of the fundamental mode. By optimizing the pump power such that the OPO threshold is reached exactly on resonance, we measure a threshold of $8.5 \pm 0.5$ mW. Using the simulated mode volume and measured quality factors, we extract a nonlinear refractive index for 4H-SiC of $n_2 = 6.9 \pm 1.1 \times 10^{-15}$ cm$^2$/W at 1550 nm, consistent with previous studies [115, 116].

# Chapter 8

# Soliton microcombs

In this Chapter, building on the demonstration of OPO in Chapter 8, we describe the first demonstration of a soliton microcomb in SiC photonics. In Part I of this Dissertation, we used soliton microcombs generated in SiC to explore their fundamental quantum properties. However, there is strong motivation to generate soliton microcombs in SiC for classical comb technologies. The dissipative Kerr soliton has become the foundation of multiple technologies, including comb-based spectroscopy [2], LiDAR [117], optical frequency synthesizers [118], and optical processors [5]. As will become evident in this chapter, SiC is uniquely suited for low-power Kerr soliton operation. SiC possesses a high linear and nonlinear refractive indices [10] ($n = 2.6$ and $n_2 = 6.9 \cdot 10^{-15}$ cm$^2$/W at 1550 nm), which makes it suitable for highly efficient, compact Kerr photonic devices. However, the tight confinement and high material index of integrated waveguides make them susceptible to scattering losses caused by surface roughness. We demonstrate the fabrication of SiC microresonators with smooth sidewalls and strong confinement with high quality factors. The fabricated microring resonators have a radius of 100 µm, height of 500-600 nm, and width of 1850 nm.

To fabricate SiC resonators, thin films of monocrystalline 4H-SiC are used [16]. Bulk high-purity semi-insulating (HPSI) SiC crystal was purchased from Cree Inc. The devices are patterned via e-beam lithography using ZEP52A e-beam resist (Zeon Corp), combined with an aluminum hard-mask to increase the SiC etching selectivity [10].

## 8.1 Cryogenic operation

We cool the device to 4 K to reduce the thermo-optic response in order to access bright soliton states via adiabatic pump frequency tuning [31]. We use a closed-cycled Montana cryostat with a three-axis piezo stage for the sample to sit. Light is coupled on and off the chip via inverse-designed vertical couplers [10]. Free space access is performed through a cryogenic-compatible doublet lens (Fig. 8.1). The light is injected and collected using single mode fiber couplers. The top cryogenic

chamber window is anti-reflection coated for operation at telecommunications wavelengths. The coupling efficiency from the single mode of the fiber into the bus waveguide was measured to be an average of 18 % across the set of characterized devices.

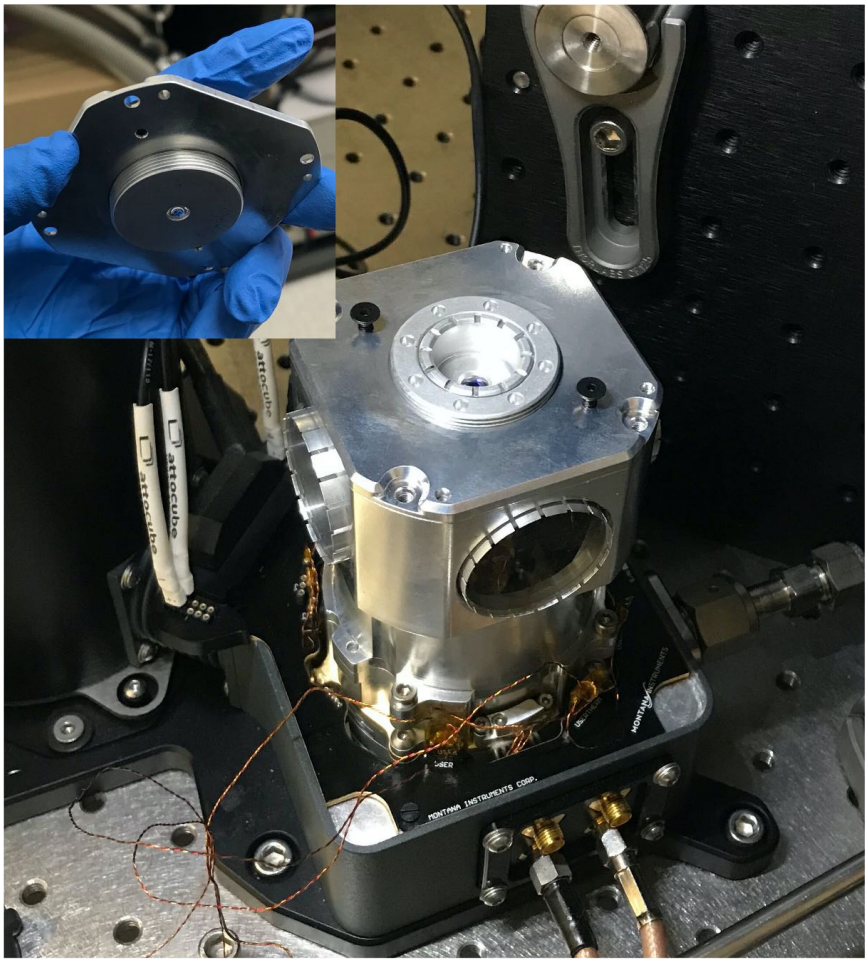


Figure 8.1: **Cryostat configuration.** Photograph of the closed-cycle cryostat used to achieve 4 K operation of the device. The sample sits inside a radiation shield where the doublet sits atop. The final enclosure features an AR-coated window at the top. Inset: view of the imaging doublet lens from below.

We first check the influence of cryogenic operation on key system parameters, including the quality factors and dispersion [31]. Figure 8.2 shows the result of tracking the resonance wavelength of a mode from room temperature to 4 K. As expected, the resonance experiences a blue shift as it is cooled. The mode shifts by 330 GHz ($\tilde{2}.7$ nm). At each temperature, we extract the drop in transmission and linewidth of the resonance to extract the intrinsic and coupling quality factors. While there is some variation in the quality factors across the scan, the average stays constant. The

variation is likely attributed to temperature tuning induced avoided mode crossings with other mode families of lower quality factor. We observe no difference in the measured dispersion with the change in temperature.

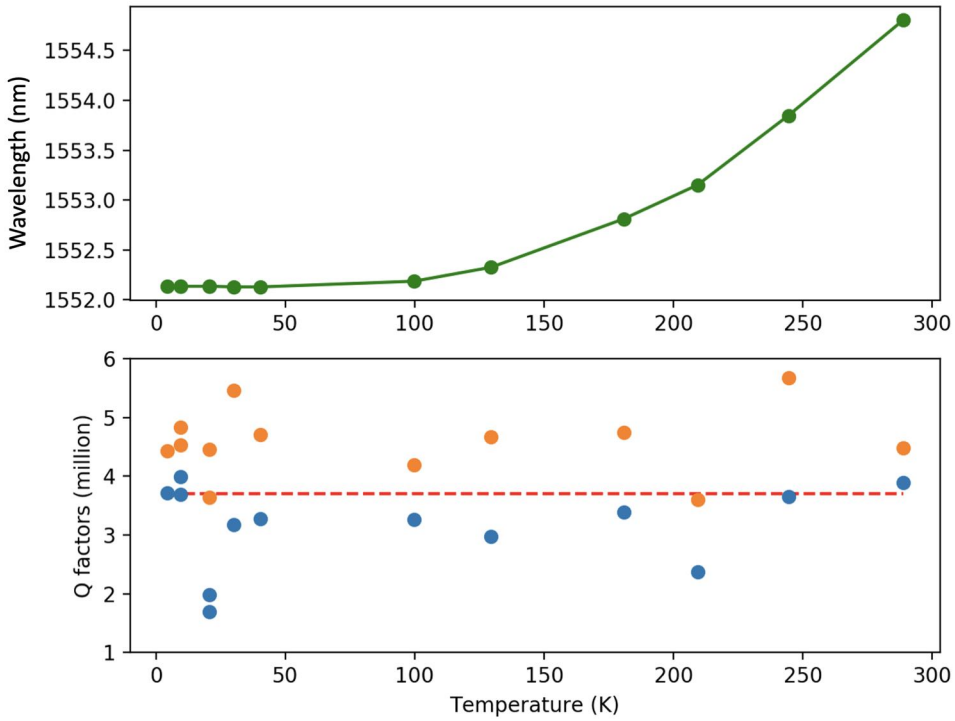


Figure 8.2: **Temperature dependence of the quality factor and resonance frequency.** Top: Resonance wavelength versus stage operation temperature for a single resonance. The stage is equipped with a local heater to tune the temperature. Bottom: Measured intrinsic and coupling quality factors versus temperature for the same resonance.

From the frequency shift, the effective thermo-optic coefficient $\partial n/\partial T$ can be retrieved if $\partial \nu/\partial n$ is calculated via an eigenmode solver [119]:

$$\partial n/\partial T = (\partial \nu/\partial n)^{-1}\partial \nu/\partial T$$

where $T$ is the temperature and $\nu$ is the frequency. We note that the shift includes a contribution from thermal expansion, though the coefficient of thermal expansion for 4H-SiC is an order of magnitude lower than the thermo-optic coefficient at room temperature. We find that at 4 K, the effective thermo-optic coefficient is reduced from its room temperature value by nearly three orders of magnitude.

## 8.2 Sub-mW parametric oscillation threshold

In the Chapter 7, we discussed the experimental details for the first demonstration of optical parametric oscillation in the platform. In this section, we show a significantly lower threshold, enabled by lower propagation loss through improved fabrication methods of the devices [46]. The efficiency of the Kerr nonlinear interaction improves with higher quality factors of the optical resonator. For example, the threshold relation for optical parametric oscillation in a microresonator can be expressed in the following form:

$$P_{th} = \frac{\pi n \omega_0 A_{\text{eff}}}{4\eta\, n_2} \frac{1}{D_1 Q^2} \tag{8.1}$$

where Q denotes the total Q factor (intrinsic loss and loading included) with pump mode frequency $\omega_0$, $A_{\text{eff}}$ is the effective mode area, $\eta$ is the cavity-waveguide coupling strength, and $D_1$ is the free-spectral range (FSR) in units of rad/s. Zero detuning of the laser frequency with respect to the pump mode frequency is assumed. The parametric oscillation threshold is inversely proportional to the square of the Q factor. Fig. 8.3 shows a sub-milliwatt (approximately 510 µW) parametric oscillation threshold of a SiC optical resonator featuring an intrinsic Q factor of 5.6 million with a 350 GHz FSR.

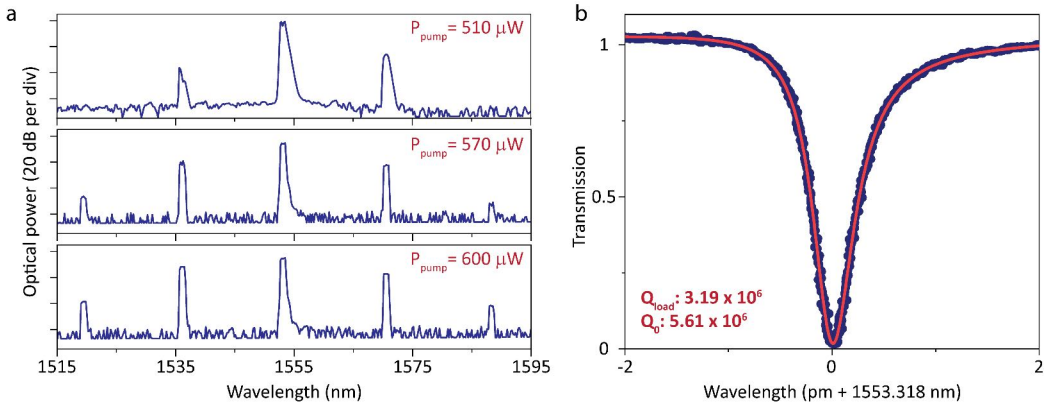


Figure 8.3: **Sub-mW parametric oscillation threshold power** (**a**) SiC parametric oscillation induced by pumping at the wavelength of 1553.3 nm. Top panel shows OPO just above the threshold power (510 µW total power in the waveguide). Middle and lower panels show measured optical spectra with loaded pump power of approximately 570 and 600 µW, respectively. (**b**) High-resolution scan of the fundamental TE mode with a loaded (intrinsic) quality factor of 3.19 (5.61) million. The mode is seen to be nearly critically-coupled to the waveguide. The scan laser wavelength is calibrated using a wavemeter, and the red curve is a fit to a Fano lineshape. The asymmetry of the resonance shape is attributed to interference with back-reflection of the vertical couplers.

## 8.3 Bright soliton

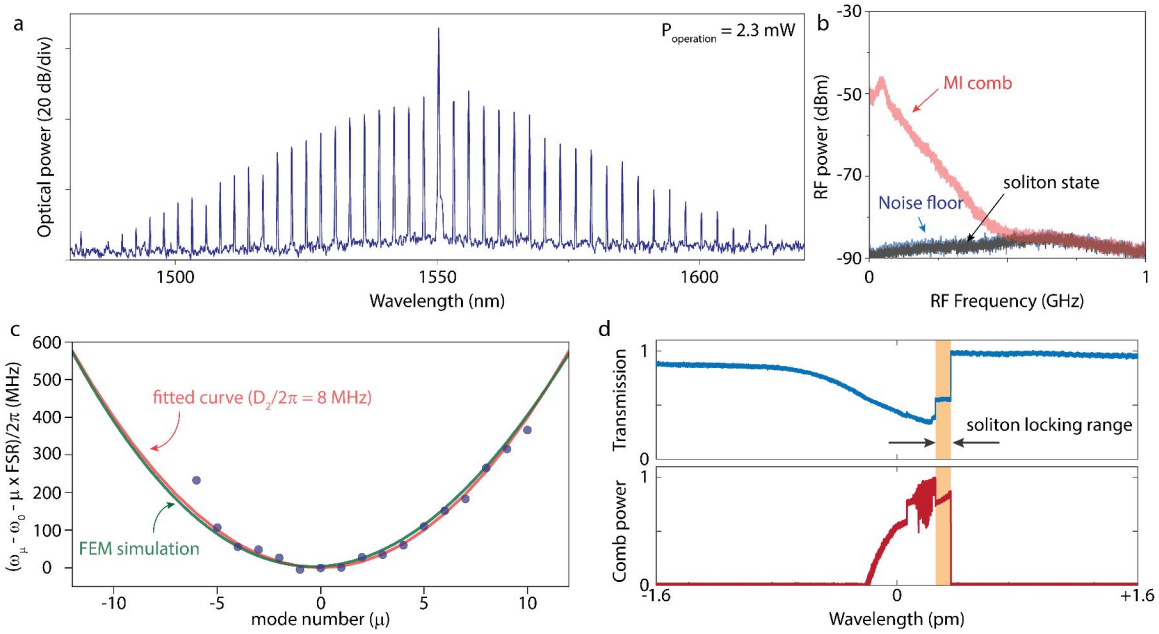


Figure 8.4: **SiC soliton microcomb** (**a**) The optical spectrum of a single soliton state with 2.3 milliwatts operation power. (**b**) RF spectrum (resolution bandwidth = 100 kHz) of the entire soliton comb confirms a low-noise state. (**c**) Measured frequency dispersion belonging to the soliton forming mode family ($TE_{00}$) is plotted versus the relative mode number. The red curve is a fit using $D_1/2\pi$ = 358.663 GHz and $D_2/2\pi$ = 8 MHz. Simulation of the soliton mode families is plotted (green curve), and the simulation fairly agrees with the measurement results. (**d**) Upper panel presents pump power transmission versus tuning across a resonance used for the soliton formation. Lower panel shows comb power trace in which the pump laser scans over the resonance from the short wavelength (blue detuned) to the long wavelength (red detuned). The shaded region (orange) depicts the spectral region where the single soliton exists.

Coherently pumped solitons in optical microresonators form as a result of the balance of the Kerr nonlinear shift and the cavity dispersion, as well as the parametric gain and the cavity loss. The soliton-forming mode family (in particular for bright solitons) in a microresonator must feature anomalous dispersion and minimal distortion of the dispersion (*e.g.*, minimal avoided-mode-crossings). The power requirement for soliton operation is inversely proportional to the total Q factor of the mode family [112].

We demonstrate the generation of a dissipative soliton microcomb in a SiC microresonator. Figure 8.4a shows the spectrum measured for a single-soliton state, and the soliton spectral shape follows the square of a hyperbolic secant function. Small spurs in the spectrum correlate with the avoided-mode-crossings in the mode dispersion spectrum (Fig. 8.4c), and the RF spectrum of the single-soliton state confirms that it is a low-noise state (Fig. 8.4b). While tuning the laser through

| **Material** | **$Q_0$ (M)** | **FSR (GHz)** | **Soliton operation power (OPO threshold) (mW)** | |
|---|---|---|---|---|
| $Si_3N_4$ | 260 | 5 | $\sim 20$ | Ref. [120] |
| $Si_3N_4$ | 8 | 194 | 1.3 (1.1) | Ref. [121] |
| $Si_3N_4$ | 15 | 99 | 6.2 (1.7) | Ref. [122] |
| $SiO_2/Si_3N_4$ | 120 | 15 | 28 (5) | Ref. [123] |
| $LiNbO_3$ | 2.4 | 199.7 | 5.2 | Ref. [124] |
| AlGaAs | 1.5 | 450 | 1.77 (0.07) | Ref. [125] |
| SiC | 5.6 | 350 | 2.3 (0.51) | Chapter 8 |

Table 8.1: **Comparison of integrated soliton device performance**

the resonance mode, the pump power transmission as well as the comb power (Fig. 8.4d) show a step transition from modulation instability (MI) and a chaotic comb state to a stable soliton comb state. The high Q SiC resonator enables a low operation power of the soliton microcomb of 2.3 mW: Table 8.1 compares operation powers of various chip-scale soliton devices.

## 8.4 Soliton crystals

Soliton crystals, temporally-ordered ensembles of soliton pulses, have been observed in various optical resonator platforms, and their dynamics as well as defect-free generation have been actively explored. We demonstrate soliton crystal states with 2- and 7-FSR comb spacing, corresponding to phase-locked lattice of 2 and 7 identical solitons, respectively. We characterize the soliton crystals through the analysis of their optical spectra, RF beatnote, and second-order photon correlations. The 7-FSR soliton crystal measurement is shown in Part 1, Chapter 4.

Figure 8.5 shows the OSA spectrum and RF beatnote noise of the 2-FSR soliton crystal state that is studied in Chapter 4. In that Chapter, the RF beatnote of a single resonator mode is shown; In Fig. 8.5, we show the RF spectrum of the whole comb. Sweeping the laser from blue- to red-detuned, we observed a transition from a broad and noisy RF signal corresponding to the modulation instability (MI) state, to a low-noise state, coinciding with the beginning of a discrete step in the transmission trace across the cavity resonance.

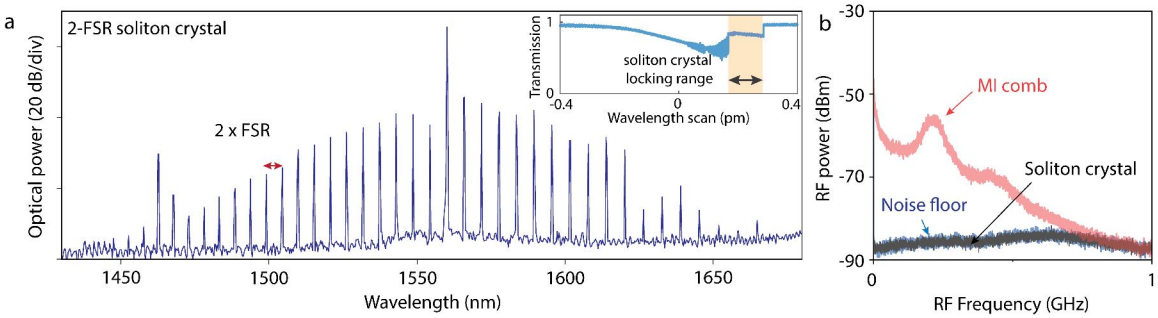


Figure 8.5: **2-FSR soliton crystal state** (**a**) OSA spectrum of the soliton crystal state. Inset: pump power transmission versus laser tuning when the pump laser wavelength is scanned from blue- to red-detuned across the pump resonance. (**b**) RF spectra (resolution bandwidth = 100 kHz) of the soliton comb (black) and MI comb (red).

# Chapter 9

# Supercontinuum generation

In this Chapter, we further extend the nonlinear light generation toolbox of SiC photonics to demonstrate broad (2.8 octaves) supercontinuum generation in silicon carbide waveguides, with comb generation in the mid-infrared (as far as 3.8 um) [98]. The bandgap of 3.2 eV of the 4H polytype allows use of the visible spectrum, while the optical transparency window extends beyond 5.5 um.

The principle behind supercontinuum generation is the extreme coherent broadening of an optical spectrum from nonlinear effects. One application of supercontinuum generation is to extend combs into wavelength regimes which are difficult to access with conventional lasers. For example, with appropriate dispersion design, femtosecond pulses centered at 1600 nm can be used to efficiently generate a comb in the mid-infrared. By using an additional nonlinear process, such as second-harmonic or third-harmonic generation, and beating its generated signal with light from the broadened supercontinuum, the carrier-envelope offset frequency of the comb may be measured and stabilized, known as self referencing. This enables one to precisely know the exact optical frequencies of all teeth of the broadened comb (which may span many octaves, comprising millions of teeth), a powerful instrument for spectroscopy. The key parameter which controls the shape of the generated supercontinuum is the waveguide dispersion. One can control the integrated dispersion by tuning the thickness and width of the SiC waveguides:

$$\Delta\beta(\omega) = \beta(\omega) - \beta(\omega_0) - \beta_1 \times (\omega - \omega_0) \tag{9.1}$$

The dispersive waves will be generated at the zero-dispersion points in the spectrum [126]. Numeric solutions of integrated dispersion for waveguides of different width are shown in Fig. 9.1.

We fabricate 4 mm-long 500 nm thick 4H-SiC waveguides encapsulated in SiO2, where the widths of the waveguides are swept to measure different dispersion conditions (Fig. 9.2). The waveguides are designed with inverse tapers at to optimize the edge-coupling to the fundamental TE mode. The waveguide dimensions are chosen to feature anomalous dispersion for a pump wavelength of

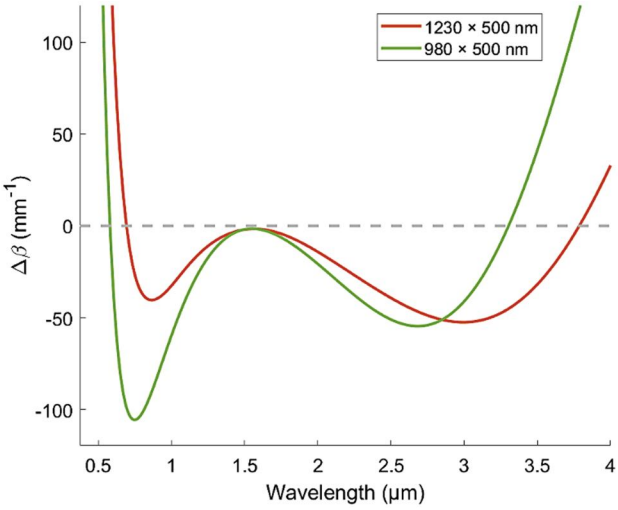


Figure 9.1: **Dispersive wave phase-matching condition.** Integrated dispersion versus wavelength for waveguides with two different cross-sections. The zero-crossing point indicates the best phase-matching for the dispersive wave. By tuning the waveguide width, the dispersive wave frequency may be shifted.

1550 nm. The integrated dispersion is tailored to target dispersive wave generation in the mid-infrared, between 3 um and 4 µm.

The pump pulse source is an erbium-doped fiber mode-locked laser emitting pulses of 70 fs, at a rate of 100 MHz, centered at 1570 nm and with a free-space power of 300 mW. The generated supercontinuum light at the end of the waveguide is collected via lensed fiber and measured on an optical spectrum analyzer. We collect the mid-infrared region of the spectrum using a set of lenses and fiber adapted for operation in that wavelength regime. The spectrum is then measured using an optical spectrum analyzer with operation up to 2.4 µm and a Fourier-transform spectrometer for the longer end of the spectrum.

Figure 9.3 shows measured supercontinuum spectra for two of the waveguides. The initial pump spectrum is shown in blue. The red is the measured spectrum at the waveguide output. We observe the expected broadening as well as dispersive waves generated around 3.2 and 3.8 µm, per the design of the integrated dispersion. The system parameters are used to simulate the expected spectrum via numeric solution of the nonlinear Schrödinger equation [127]. The spectra were measured for an estimated on-chip pulse energy of 0.2 nJ, slightly lower than demonstrations of mid-IR dispersive waves in silicon nitride [127] and aluminum nitride [128], suggesting that SiC is an efficient platform for this application. The integrated dispersion can be designed to be almost flat across the spectral region of interest. In this configuration, we generate smooth continuum spanning 2.8 octaves (Fig. 9.4). This spectrum was also obtained with an on-chip pulse energy of 0.2 nJ.

A frequency comb is defined by its repetition rate and the absolute offset of the comb, known

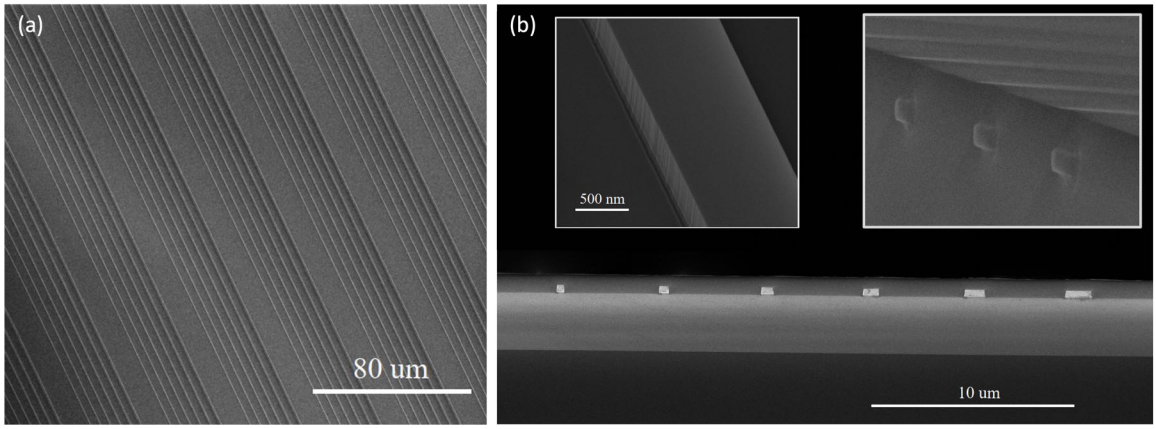


Figure 9.2: **Device under test.** Scanning electron micrographs of SiC waveguides before encapsulation with SiO2. (a) View from above of the waveguides. (b) View of waveguide cross-section and sidewall roughness.

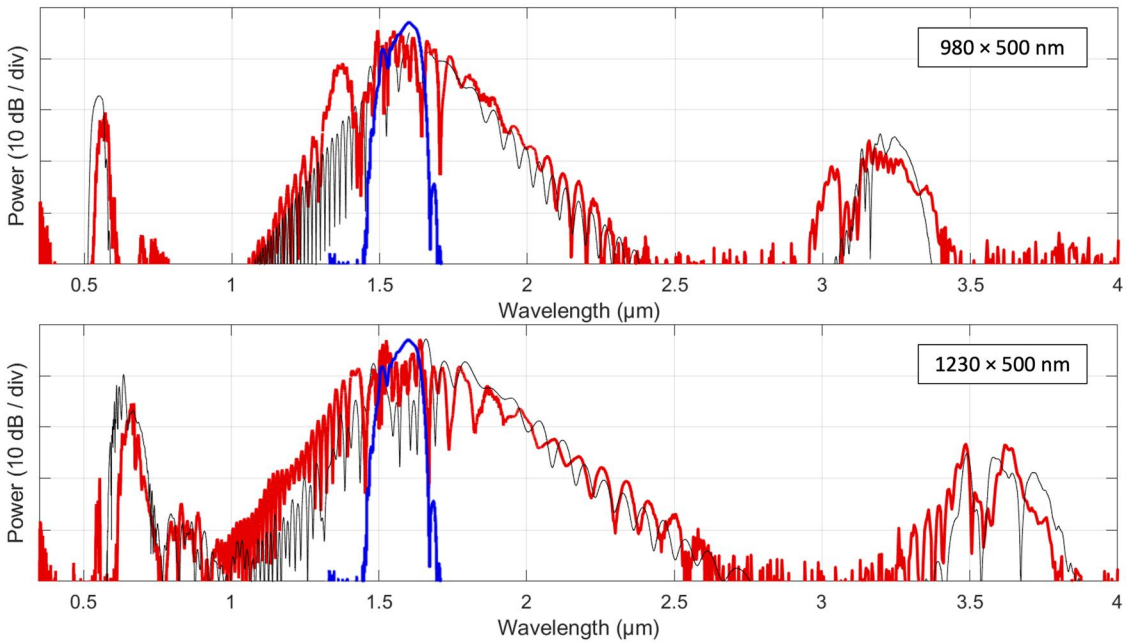


Figure 9.3: **Supercontinuum generation into the mid-infrared.** Measured (red) and simulated (black) supercontinuum versus the initial pulse spectrum (blue). Top: Waveguide dimension of 980 nm width and 500 nm height. Bottom: Dimension of 1230 nm width and 500 nm height.

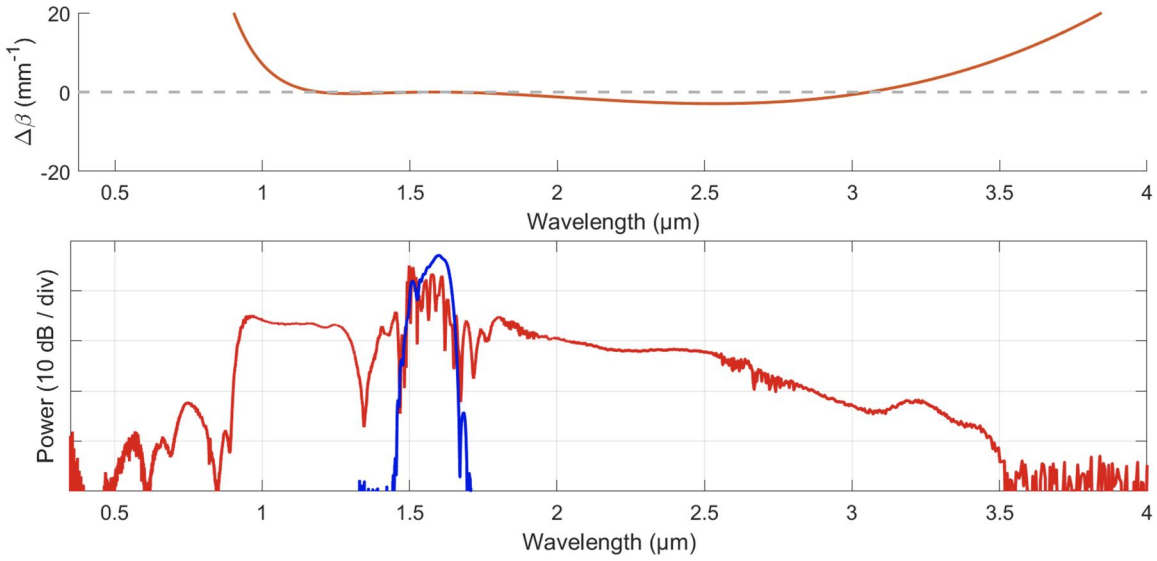


Figure 9.4: **Broad supercontinuum generation.** Top: Simulated integrated dispersion for a 2000 nm by 500 nm waveguide. Bottom: Measured output spectrum versus the input pulse spectrum.

as the carrier-envelope offset (CEO) frequency. The repetition rate may be measured in a straightforward way by sending the pulses to a photodetector, but the CEO cannot be accessed directly. A convenient way to measure it is via the self-referencing method: the principle consists in interference between high-frequency comb lines and frequency-doubled low-frequency comb lines, measured on a fast photodetector. The observed beating signal is the carrier-envelope offset frequency. This technique requires a second harmonic process as well as an octave-spanning comb. As discussed in Chapter 6, silicon carbide features an optical second-order nonlinearity and resonant second-harmonic generation has been demonstrated. Using a similar phase-matching condition as in Chapter 6, the supercontinuum waveguides were designed specifically for second-harmonic generation from the TE00 mode at 1600 nm.

In the waveguides where phase-matching was engineered, there are peaks near the second-harmonic frequency of the pump that shift with waveguide dimension (Fig. 9.5). The power of the highlighted peak is measured against the input power; a quadratic relation with input power is recovered, indicating that the peak is likely originating from second-harmonic generation. Depending on the second-harmonic generation phase-matching condition and the position of the dispersive wave, different visible colors are observed scattering from the end of the waveguide (Fig. 9.6). Some peaks are overlapped with the main body of the supercontinuum, suggesting that these devices may be suitable for measuring and stabilizing the CEO frequency of the comb. A next step is to identify a waveguide dimension that simultaneously features self-referencing and dispersive waves in the mid-infrared and to lock the CEO frequency of the mid-infrared comb for spectroscopy applications.

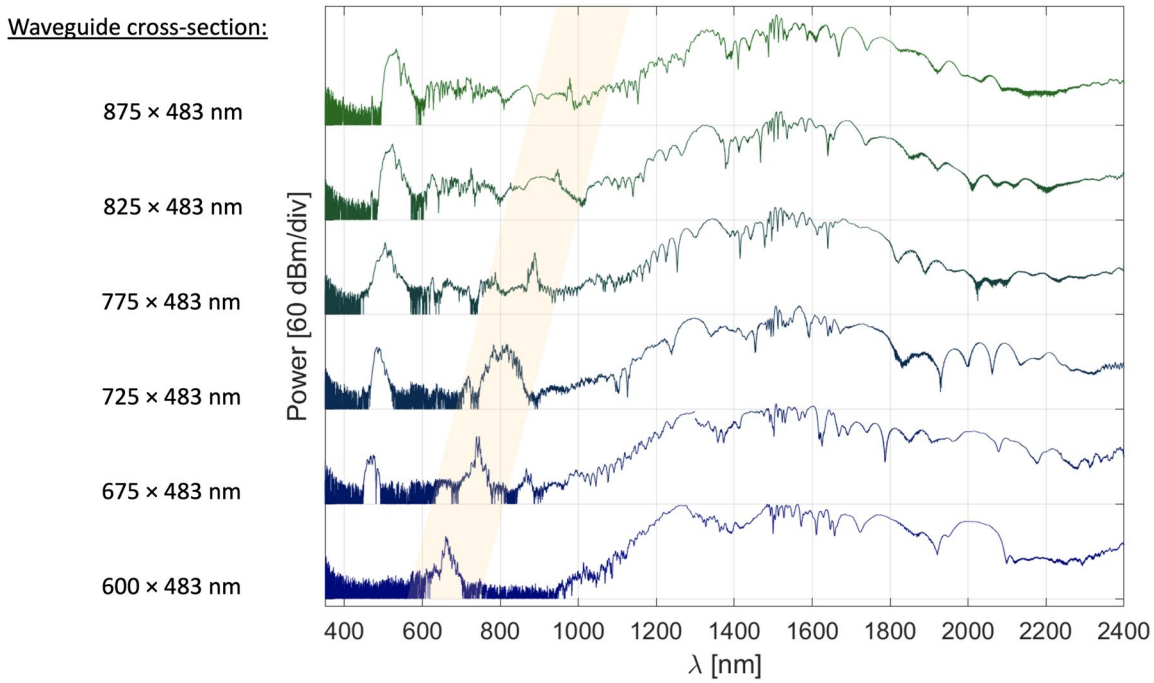


Figure 9.5: **Prospect for self-referencing.** Simultaneous supercontinuum generation and second-harmonic generation for different waveguide widths. The power of the highlighted peak is measured against the input power; a quadratic relation with input power is recovered, indicating that the peak is likely originating from second-harmonic generation.

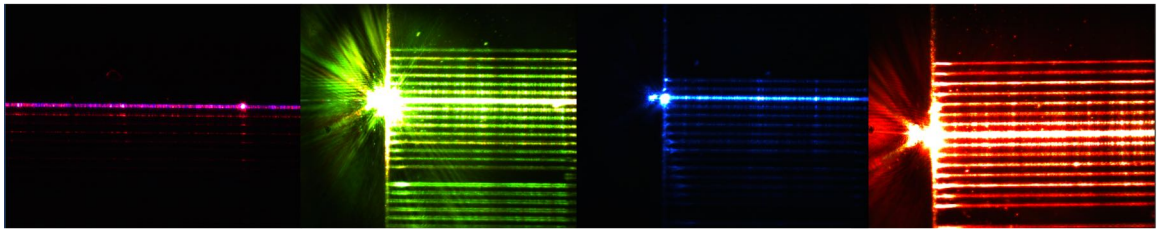

Figure 9.6: **Optical images during operation.** Scattered visible light from waveguides of different widths, where the photo is taken near or at the end of the waveguide.

# Chapter 10

# Multi-mode multi-emitter cavity QED

In Chapters 7-10, we discussed three distinct classical photonics demonstrations utilizing the optical nonlinearities of SiC. In this Chapter, we turn in a quite different direction to study one of the most unique attributes of the material: SiC hosts optically-addressable crystal defects (*color centers*) with very long spin lifetimes.

We detail the integration of stable and coherent color centers into thin-film integrated photonics for the first time, using the SiC platform. We measure a whispering gallery mode resonator coupled to two spin qubits, and study the multi-emitter multi-mode cavity quantum electrodynamics (QED) unique to this system.

Color centers [129, 130, 131] are among the leading contenders for the realization of distributed quantum information processing, including communication [132, 133] and computation [134], combining a long-lived multi-qubit spin register [135] with a photonic interface in the solid state. To continue scaling up quantum networks while maintaining high entanglement generation rates, the intrinsically weak interaction between photons and color centers must be enhanced via integration into photonic resonators [136, 137, 16, 133, 138, 139, 140]. Efforts in cavity integration have already enabled milestone demonstrations such as cavity-mediated coherent interaction between two emitters [137], single-emitter cooperativity exceeding 100 and spin-memory-assisted quantum communication [133]. The ultimate goal of quantum computation and error-protected communication [141] requires the realization of photonic circuits with high complexity and minimal inter-node loss, and will require bringing together all integrated photonics expertise developed in the past two decades [142].

Yet color center technologies cannot at present take advantage of the state of the art in integrated photonics, due to two central challenges. First, thin-film-on-insulator photonics technologies have been incompatible with high-quality color centers: this motivated the focus on bulk-crystal-carving

methods [143, 136, 93, 144, 145], suitable for fabrication of individual devices but restrictive in terms of large-scale monolithic photonic circuits. Second, absence of a first-order Stark shift, which renders a defect's optical transitions insensitive to electric field noise (as is the case for inversion symmetric defects [146, 147]) had been widely considered to be a prerequisite for color centers to maintain optical coherence in nanophotonic structures. This notion motivates the dominant focus on group-IV color centers in diamond (SiV, SnV, GeV) [148]. While inversion symmetry is not in theory needed for the absence of a first-order Stark shift [149], a non-polar, non-centrosymmetric defect is yet to be identified experimentally. Among the materials that lack crystal inversion symmetry is SiC [17], which has otherwise emerged as the top contender for wafer-scale integration of color centers with excellent spin-optical properties (such as the silicon vacancy ($V_{Si}$) [150, 151, 152, 153, 145] and the divacancy [110, 154]). The requirement of zero first-order Stark shift for maintaining optical coherence in nanostructures has only recently been challenged in a demonstration of optically-coherent $V_{Si}$ in bulk-carved SiC nanobeams [145].

In this Chapter, we demonstrate the integration of optically-coherent non-inversion-symmetric color centers into scalable thin-film SiC nanophotonics. We demonstrate cavity cooperativity of a single $V_{Si}$ color center of up to 0.8, allowing for the observation of dipole-induced transparency [155] in SiC. We use this platform to demonstrate superradiant emission of two SiC color centers.

## 10.1 Optically-coherent color centers

The photonic device consists of a microdisk resonator integrated with a waveguide (Fig. 10.1(a)), fabricated in 4H-SiCOI [16]. The high-Q transverse-magnetic (TM) modes of the resonator optimally align with the dipole moment of the $V_{Si}$ in a *c*-cut wafer [150]. The coupling waveguide terminates in a flat facet on both ends to allow for efficient single-mode free-space coupling. We observe a total coupling efficiency from the waveguide to the single-mode fiber of up to 24%, which includes all setup losses. The experiments are performed at 4.3 K in a closed-cycle cryostat (Montana Instruments). The microresonator modes are tuned spectrally via argon gas condensation [156]. A pulsed femtosecond laser centered at 740 nm is used to uniformly excite the emitters in the disk: it couples to all resonator modes simultaneously, owing to its broad spectrum. As the microresonator is gas-tuned, an enhancement of emission at the $V_{Si}$ zero-phonon line (ZPL) wavelength of 916.5 nm (as observed via a spectrometer) indicates Purcell enhancement of one or more $V_{Si}$. With a resonator mode parked at the Purcell enhancement condition, we measure the absorption lines of the coupled emitters via photoluminescence excitation (PLE), where a weak (0.5 pW in the waveguide) continuous-wave resonant laser is scanned across the ZPL while detecting the phonon sideband (PSB) of the emitters. A PLE scan shows that in this device, two emitters are coupled to the cavity (Fig. 10.1b), henceforth labeled emitters A and B. The $V_{Si}$ is known to feature two spin-conserving optical transitions, $A_1$ and $A_2$, split by 1 GHz [151]. We perform experiments with a weak off-axis

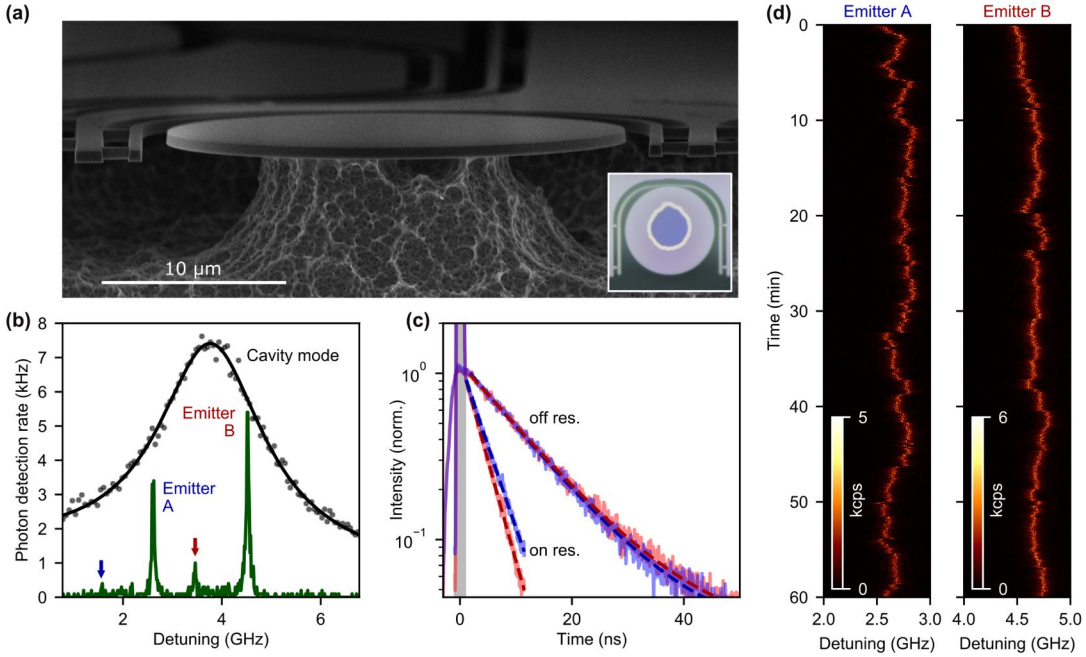


Figure 10.1: **Spectrally-stable $V_{Si}$ emitters in integrated 4H-SiCOI photonics. (a)** Scanning electron micrograph of the device. A waveguide, which wraps around the disk (seen in the optical microscope image, inset), is coupled to the resonator. A microscope objective is used to couple light to and from the flat facets of the waveguide. **(b)** A cavity photoluminescence spectrum (emitter PLE spectrum) in black (green), taken with a scanning resonant laser with 1.5 μW (0.5 pW) of power in the waveguide. We extract a loaded cavity quality factor of $Q = 1.3 \cdot 10^5$. The prominent peaks at 2.7 and 4.5 GHz detuning are the $A_2$ transitions of the two emitters. The corresponding $A_1$ transitions are labelled with arrows. In this figure and henceforth, laser detuning is relative to 327.113 THz (916.5 nm). **(c)** Lifetime measurements for emitter A (blue) and emitter B (red) on- and off-resonance with the cavity. The gray region represents the excitation pulse. **(d)** A 1-hour PLE scan (3.6 s per line) of each emitter (while the other is selectively ionized into the dark state), with the cavity positioned on-resonance with the emitter.

external magnetic field that mixes the ground-state spins, which renders the optical transitions no longer spin-conserving, eliminating resonant-laser-induced spin-polarization. We focus our study on the $A_2$ transition of each emitter, which is brighter due to its higher quantum efficiency [151]. We optimize the magnetic field orientation to reduce the relative intensity of the $A_1$ transition upon resonant driving through coherent population trapping of the spin-$\frac{3}{2}$ sublevels [157]. In order to investigate the strength of cavity-waveguide coupling, we scan a laser at a higher power (1.5 μW in the waveguide) to observe a dip in power on resonance. The absence of a cavity transmission dip suggests that the resonator mode is strongly undercoupled to the waveguide. In order to observe the cavity resonance, we take advantage of the fluorescence generated by the resonator surfaces that

can be excited by a laser in the $V_{Si}$ ZPL wavelength range and can emit in the $V_{Si}$ PSB wavelength range. Since the fluorescence is proportional to the power circulating in the resonator, the fluorescence intensity traces out the Lorentzian profile of the cavity mode, from which we extract a loaded quality factor of $1.3 \cdot 10^5$ (Fig. 10.1b).

The emitter-cavity coupling rate is a key metric for cavity quantum electrodynamics systems. We determine coupling strength of each emitter to the cavity by measuring the emitter lifetime reduction on resonance, known as Purcell enhancement. First, we selectively ionize one emitter into the dark state via strong resonant excitation, and tune the cavity on-resonance with the remaining bright emitter. We then excite the emitter with 150 ps resonant pulses (obtained via pulse-shaping a mode-locked Ti:Sapphire laser) through the cavity mode and detect the transient ZPL emission using temporal filtering. As shown in Fig. 10.1(c), the on-resonance lifetime for emitter A (B) is measured to be 4.2 ns (3.5 ns), which corresponds to a lifetime reduction of 2.7 (3.2) from the bulk lifetime of 11.3 ns [19], and a Purcell enhancement $F$ of 30 (39) [157]. From the simulated mode volume of $128(\frac{\lambda}{n})^3$ for the fundamental $TM_{00}$ mode, we find the theoretical maximum Purcell enhancement of 77 in this device. The observed Purcell enhancement is comparable to that achieved in the first integration demonstrations of the diamond silicon vacancy [136, 158] and tin vacancy [139, 140] into photonic crystal nanobeam cavities, despite the much stronger mode confinement of those devices. We attribute this to the optimal dipole overlap of the $V_{Si}$ with the cavity TM mode and the less stringent emitter positioning requirements of the microdisks. Via resonant pulsed excitation with 1 ns long pulses (generated from a continuous-wave laser using electro-optic amplitude modulation) and detection of the PSB emission with the cavity detuned by $-80$ GHz, we measure the off-resonant lifetime of emitter A (B) to be 10.7 ns (11.1 ns). The minor discrepancy between the off-resonant lifetimes and the bulk lifetime (11.3 ns) is attributed to the coupling of the emitters to other modes of the microdisk.

Although Purcell enhancement has been observed in several color center platforms [138, 159, 136, 158, 139], including thin-film diamond [160] and SiC [16], to date cavity-coupled color centers that retain their optical coherence have only been demonstrated in bulk-carved diamond [136, 137]. To quantify the optical coherence and the spectral stability of the $V_{Si}$ in 4H-SiCOI microdisks, we perform continuous PLE scans on each emitter while on- and off-resonance with the cavity. The on-resonance PLE scans are shown in Fig. 10.1(d). Emitters A and B were measured at different times, and the cavity was spectrally aligned with the measured emitter before the start of each one-hour acquisition. Over the course of one hour, no emitter ionization is observed, and slow spectral diffusion is below 500 MHz. The average single-scan optical transition linewidth for emitter A (B) is found to be 54.3(3) MHz (63.4(3) MHz), which corresponds to 17 MHz (18 MHz) of spectral diffusion beyond the transform limit. Repeating the measurement off-resonance, we find the emitter A (B) linewidth to be 37.8(8) MHz (38.5(8) MHz), which corresponds to 24 MHz of spectral diffusion beyond the transform limit [157]. The reduced spectral diffusion on-resonance may be due to a

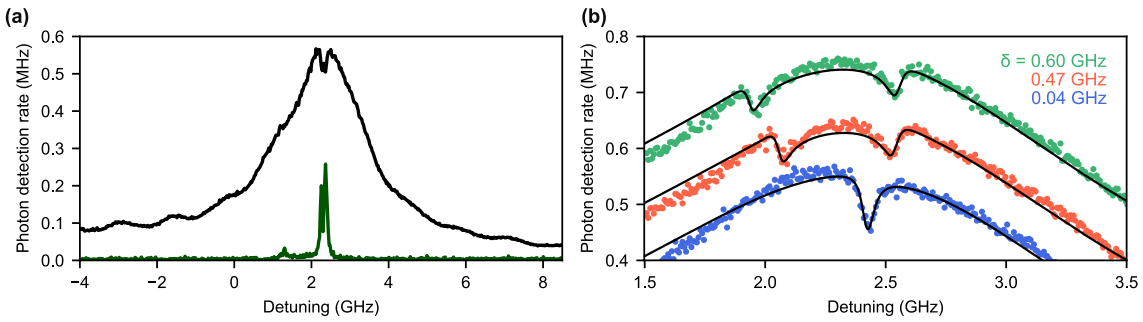


Figure 10.2: **Dipole induced transparency (DIT) in SiC. (a)** A wide laser scan across the cavity resonance, showing the transmission spectrum through the device (black). The $V_{Si}$ phonon sideband emission is simultaneously detected (green, multiplied by 50x). Excitation of the resonator mode is performed through a scattering imperfection on the disk edge and transmission through the waveguide is detected. **(b)** Close-up scan at the cavity center for different emitter detunings $\delta$. Orange and green traces are offset by +0.1 and +0.2 MHz, respectively.

decreased rate of excitation of surface-related defects, because the well-confined TM cavity mode is efficiently excited with low laser power. These results indicate excellent spectral stability of the nanophotonics-integrated $V_{Si}$.

## 10.2 Dipole-induced transparency

From the measured Purcell enhancement and off-resonant emitter linewidths, we calculate the emitter-cavity cooperativity $C = \frac{4g^2}{\kappa\gamma}$ to be 0.6 and 0.8 for emitter A and B, respectively. This regime enables the observation of dipoled-induced transparency (DIT) [155], where the $V_{Si}$ scatter photons from an input coherent state. Because the device studied here is strongly under-coupled to the bus waveguide, DIT is difficult to observe through waveguide transmission. We instead excite the disk through a scattering point on its edge, and detect transmission into the waveguide, thus in effect performing the measurement in a drop-port configuration [155]. Scanning the continuous-wave laser across the disk resonance, DIT dips for both emitters are clearly observed, shown in Fig. 2(a,b). The slow spectral drift of the emitters allows us to measure DIT for different relative detunings. Looking forward, spin initialization, targeted emitter placement, and cavities with a larger $Q/V$ metric [16, 15] will enable stronger transmission contrast in DIT for the realization of spin-photon entanglement and spin-readout via the modification of cavity reflectivity [137, 133].

### 10.2.1 Derivation for whispering gallery mode resonator

Dipole induced transparency is often explored for a system where a single cavity mode couples to one or more emitters [155], which is the case for a nanobeam [136], two-dimensional photonic

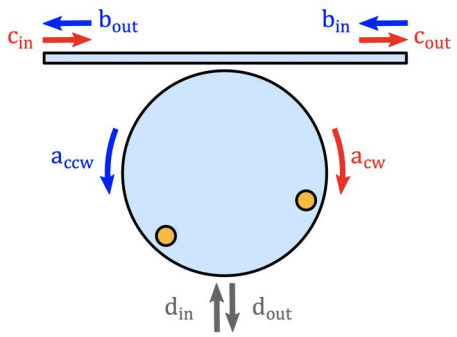


Figure 10.3: **Input-output diagram for the microdisk.** Bath and cavity operators for a disk resonator coupled to a single bus waveguide along with a scattering port.

crystalm[15], or Fabry-Pérot resonator [161]. The whispering gallery mode (WGM) resonator is distinct in that each resonance corresponds to two degenerate cavity modes. In this section, we define a model to describe transmission through the WGM resonator in the presence of quantum emitters. We describe our model in the clockwise (CW) and counter-clockwise (CCW) propagating mode basis. These modes are degenerate with resonance frequency $\omega_0$ and are described by cavity mode annihilation operators $a_{\mathrm{CW}}$ and $a_{\mathrm{CCW}}$. Using the input-output formalism [28], we write the relations between the bath operators, including the scattering-defect excitation port used in experiment (Figure 10.3):

$$
\begin{aligned}
b_{\mathrm{out}} &= \sqrt{\kappa_c} a_{\mathrm{CCW}} + b_{\mathrm{in}} \\
c_{\mathrm{out}} &= \sqrt{\kappa_c} a_{\mathrm{CW}} + c_{\mathrm{in}} \\
d_{\mathrm{out}} &= \sqrt{\kappa_d} D + d_{\mathrm{in}} = \sqrt{\kappa_d}(\sqrt{\alpha} \cdot a_{\mathrm{CW}} + \sqrt{1-\alpha} \cdot a_{\mathrm{CCW}}) + d_{\mathrm{in}}
\end{aligned}
$$

Here, $D$ is the resonator mode which the scattering port couples to fully. Note that it is not necessarily a standing wave: $D$ couples with strength $\alpha$ to $a_{\mathrm{CW}}$ and $(1-\alpha)$ to $a_{\mathrm{CCW}}$. We have defined two coupling rates: $\kappa_c$ between the resonator and the bus waveguide and $\kappa_d$ between the resonator and the scattering channel. The emitters in the WGM resonator couple maximally to two different standing waves:

$$
\begin{aligned}
S_1 &= \frac{1}{\sqrt{2}}[a_{\mathrm{CW}} e^{i\theta} + a_{\mathrm{CCW}} e^{-i\theta}] \\
S_2 &= \frac{1}{\sqrt{2}}[a_{\mathrm{CW}} e^{i\phi} + a_{\mathrm{CCW}} e^{-i\phi}]
\end{aligned}
$$

where $\theta$ and $\phi$ define the azimuthal orientation (phase) of the standing waves relative to the excited mode $D$. The emitters, modeled as a pair of two-level systems with associated annihilation operators

$\sigma_1$ and $\sigma_2$, couple to these standing waves with coupling coefficients $g_1$ and $g_2$. We write a non-Hermitian Tavis-Cummings Hamiltonian which includes the decay of the emitters and the cavity:

$$\begin{aligned} H_{\mathrm{TC}} =&(\omega_0 + \Delta - \delta/2 - i\gamma_1)\sigma_1^\dagger\sigma_1 + (\omega_0 + \Delta + \delta/2 - i\gamma_2)\sigma_2^\dagger\sigma_2 \\ &+ (\omega_0 - i\kappa)(a_{\mathrm{CW}}^\dagger a_{\mathrm{CW}} + a_{\mathrm{CCW}}^\dagger a_{\mathrm{CCW}}) + \underbrace{\left[g_1 S_1^\dagger\sigma_1 + g_2 S_2^\dagger\sigma_2 + \mathrm{h.c.}\right]}_{H_I} \end{aligned}$$

where $\omega_0$ is the cavity resonance frequency, $\Delta$ is the frequency difference between the cavity and the center of the two emitters, $\delta$ is the frequency difference between the two emitters, $\gamma_j$ is the linewidth of the $j$th emitter (which includes all sources of decay and dephasing), and $\kappa$ is the total decay rate of the cavity. We can explicitly write out the coupling term with respect to the CW and CCW modes:

$$g_1 S_1^\dagger\sigma_1 + g_2 S_2^\dagger\sigma_2 = \frac{g_1}{\sqrt{2}}(e^{-i\theta}a_{\mathrm{CW}}^\dagger\sigma_1 + e^{i\theta}a_{\mathrm{CCW}}^\dagger\sigma_1) + \frac{g_2}{\sqrt{2}}(e^{-i\phi}a_{\mathrm{CW}}^\dagger\sigma_2 + e^{i\phi}a_{\mathrm{CCW}}^\dagger\sigma_2)$$

We can define coupling coefficients:

$$G_1 = \frac{g_1}{\sqrt{2}}e^{-i\theta}, \quad G_2 = \frac{g_2}{\sqrt{2}}e^{-i\phi}$$

and re-write the interaction term:

$$H_I = (G_1 a_{\mathrm{CW}}^\dagger + G_1^* a_{\mathrm{CCW}}^\dagger)\sigma_1 + (G_2 a_{\mathrm{CW}}^\dagger + G_2^* a_{\mathrm{CCW}}^\dagger)\sigma_2 + \mathrm{h.c.}$$

The Heisenberg equations for the two CW and CCW cavity modes are defined as

$$\begin{aligned} \dot{a}_{\mathrm{CW}} &= -i[H_{TC}, a_{\mathrm{CW}}] - \frac{\kappa}{2}a_{\mathrm{CW}} - \sqrt{\kappa_c}c_{\mathrm{in}} - \sqrt{\alpha}\sqrt{\kappa_d}d_{\mathrm{in}} \\ \dot{a}_{\mathrm{CCW}} &= -i[H_{TC}, a_{\mathrm{CCW}}] - \frac{\kappa}{2}a_{\mathrm{CCW}} - \sqrt{\kappa_c}b_{\mathrm{in}} - \sqrt{1-\alpha}\sqrt{\kappa_d}d_{\mathrm{in}} \end{aligned}$$

Then we can write all four Heisenberg equations (in the frequency domain):

$$\begin{aligned} -i\omega a_{\mathrm{CW}} &= (-i\omega_0 - \frac{\kappa}{2})a_{\mathrm{CW}} - \sqrt{\kappa_c}c_{\mathrm{in}} - \sqrt{\alpha}\sqrt{\kappa_d}d_{\mathrm{in}} - iG_1\sigma_1 - iG_2\sigma_2 \\ -i\omega a_{\mathrm{CCW}} &= (-i\omega_0 - \frac{\kappa}{2})a_{\mathrm{CCW}} - \sqrt{\kappa_c}b_{\mathrm{in}} - \sqrt{1-\alpha}\sqrt{\kappa_d}d_{\mathrm{in}} - iG_1^*\sigma_1 - iG_2^*\sigma_2 \\ -i\omega\sigma_j &= -i[(\omega_0 + \Delta + (-1)^j\frac{\delta}{2}) - \frac{\gamma_j}{2}]\sigma_j - iG_j^* a_{\mathrm{CW}} - iG_j a_{\mathrm{CCW}} \end{aligned}$$

The measurement of Figure 2 of the main text describes the transmission through the "drop" waveguide formed between the input scattering point on the disk and the output bus waveguide:

$$t_c = \langle c_{\text{out}} \rangle / \langle d_{\text{in}} \rangle$$
$$t_b = \langle b_{\text{out}} \rangle / \langle d_{\text{in}} \rangle$$

We solve for $a_{\text{CW}}$ in terms of the input bath operators and use the expectation values of our input-output equations:

$$\langle c_{\text{in}} \rangle = \langle b_{\text{in}} \rangle = 0$$
$$\langle c_{\text{out}} \rangle = \sqrt{\kappa_c} \langle a_{\text{CW}} \rangle$$
$$\langle b_{\text{out}} \rangle = \sqrt{\kappa_c} \langle a_{\text{CCW}} \rangle$$

We solve the system of equations to arrive at the following expressions:

$$t_c = \frac{\Gamma_1 \Gamma_2 \sqrt{\kappa_d \kappa_c}}{\Phi^2 - \psi^+ \psi^-} [\sqrt{1-\alpha}\psi^+ - \sqrt{\alpha}\Phi]$$

$$t_b = \frac{\Gamma_1 \Gamma_2 \sqrt{\kappa_d \kappa_c}}{\Phi^2 - \psi^+ \psi^-} [\sqrt{\alpha}\psi^- - \sqrt{1-\alpha}\Phi]$$

where we have defined

$$\Gamma_1(\omega) = [-i(\omega - \omega_0 - \Delta + \delta/2) + \gamma_1/2], \quad \Gamma_2(\omega) = [-i(\omega - \omega_0 - \Delta - \delta/2) + \gamma_2/2]$$

$$\psi^+ = G_1^2 \Gamma_2 + G_2^2 \Gamma_1, \quad \psi^- = G_1^{*2} \Gamma_2 + G_2^{*2} \Gamma_1$$

$$\Phi = (-i(\omega - \omega_0) + \kappa/2)\Gamma_1 \Gamma_2 + |G_1|^2 \Gamma_2 + |G_2|^2 \Gamma_1$$

To account for the Fano shape observed experimentally in the transmission spectrum, we add a coherent term with a defined phase $\rho$ and amplitude $B$. We include the relative amplitude $A$ with an offset $C$:

$$T_c(\omega) = |A \cdot t_c(\omega) + B \cdot e^{i\rho}|^2 + C$$

Note that this equation does not account for the non-unity occupation probability[158] of the spin-1/2 ground state (corresponding to the $A_2$ transition). This results in an underestimate of the coupling strength between the excited mode $D$ and the emitter standing waves $S_1$ and $S_2$. In the main text, the fits are performed as follows. The cavity and Fano parameters $\omega_0$, $\kappa$, $B$, $C$, and $\rho$ are fit to the wide scan data (Fig. 10.2(a)). These parameters are fixed for all other fits. For each close-in scan in Fig. 2(b), the PLE measurement which is taken simultaneously is fit to extract the parameters $\delta$ and $\Delta$. We set the values for $g_1$ and $g_2$ to those extracted from the lifetime

measurements. In the DIT fit, the free parameters are $\theta$, $\phi$, $\alpha$, and $A$.

## 10.3 Superradiance

Photon interference between two color centers, a prerequisite for the generation of remote spin-spin entanglement, has been an outstanding challenge in SiC. Here, we demonstrate two-photon interference between two microdisk-integrated emitters, which arises from their collective coupling to the same cavity mode. To observe photon interference in the continuous wave regime, a tunable above-resonant laser is coupled to a resonator mode around 730 nm to excite both emitters. We note that while above-resonant excitation in bulk crystal has been used to obtain nearly transform-limited photon emission from the $V_{Si}$ [152], we observe that in nanostructures it induces rapid spectral diffusion due to disturbance of the surface charge environment, broadening the optical linewidths to approximately 0.5 GHz. This spectral instability reduces the rate of superradiant emission (however, optical coherence may be preserved using resonant excitation, as shown later in the work). Fig. 3(a) shows the second-order auto-correlation $g^{(2)}(\tau)$ of the color centers' collective emission in the Hanbury Brown and Twiss configuration, where emission into the waveguide is split between two detectors via a beamsplitter. The sharp peak at zero time delay is a signature of superradiant emission and the probabilistic generation of entanglement between the two color centers. This feature has also been observed with up to three waveguide-integrated quantum dots [162, 163] and a pair of waveguide-integrated silicon vacancy centers in diamond [136, 164]. In contrast, for cross-correlations between the two waveguide propagation directions, an anti-bunching interference dip is observed (Fig. 3(b)). This feature is indicative of photon pairs preferentially leaving the resonator in the same direction.

The experimentally-observed photon statistics are explained by the out-of-phase coupling of the two emitters to a pair of degenerate clockwise and counterclockwise optical modes of the resonator. The interaction Hamiltonian for this system can be written as

$$H_I = g_A \sigma_A^\dagger S_A + g_B \sigma_B^\dagger S_B + \text{h.c.}, \tag{10.1}$$

where $\sigma_A$ and $\sigma_B$ are the lowering operators for emitters A and B, respectively, and $g_A$ and $g_B$ are the emitter-cavity coupling strengths; each emitter couples to its own standing wave supermode $S_A = (a_{CW} + a_{CCW})/\sqrt{2}$ and $S_B = (e^{-i\phi} a_{CW} + e^{i\phi} a_{CCW})/\sqrt{2}$, where $a_{CW}$ ($a_{CCW}$) is the clockwise (counterclockwise) resonator propagating mode, and phase $\phi$ corresponds to the emitters' azimuthal separation in the resonator. Consider two special cases: (i) for $\phi = (0 \mod \pi)$, $S_A = \pm S_B$ and the two emitters couple to the same standing wave mode, resulting in a single-mode interaction[137]; (ii) for $\phi = (\pi/2 \mod \pi)$, $S_A$ and $S_B$ are orthogonal, and in the standing wave basis the emitters are de-coupled. However, because the measurement is performed in the propagating mode basis $\{a_{CW}, a_{CCW}\}$ (corresponding to emission to the right and to the left, respectively), the pair of

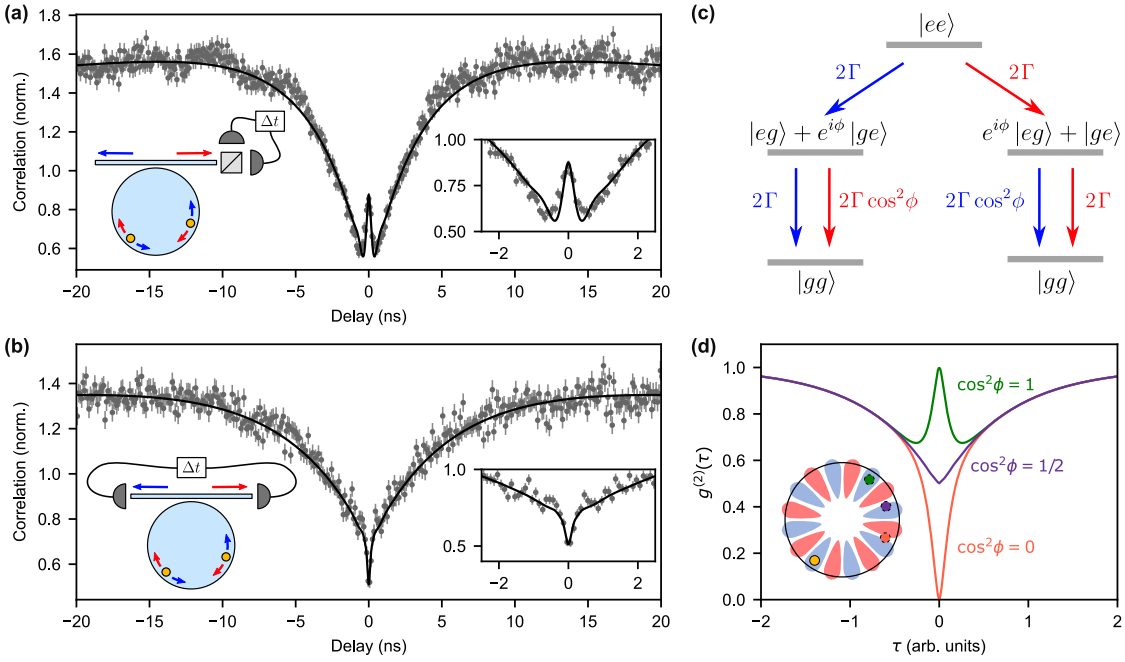


Figure 10.4: **Superradiant emission of two $V_{Si}$ color centers. (a)** Second-order correlation of the photon emission along one waveguide direction displays bunching at zero time delay, a signature of superradiance. Inset: zoom-in of the superradiance feature. Error bars represent standard error. **(b)** The relative phase $\phi$ of the emitters impacts the cross-correlation photon statistics between the opposite waveguide directions and can produce anti-bunched emission. The solid line in a,b is the numerical fit based on a five-level model [19] of the $V_{Si}$ (normalized to $g^{(2)}(\tau \to \infty) = 1$) **(c)** The level structure representing the pair of two-level-system emitters decaying into degenerate clockwise (red arrows) and counterclockwise (blue arrows) optical modes. The corresponding transition rates are indicated next to the arrows, where $\Gamma$ is the unmodified single-emitter decay rate into a propagating mode. **(d)** Theoretically-predicted phase-dependent cross-correlation between clockwise and counterclockwise modes for a pair of ideal two-level emitters. The inset shows a schematic of the mode profile and the two emitters. The placement of the second emitter (relative to the first emitter, yellow) corresponds to the three cases.

emitters exhibits interference for all values of $\phi$. For $(\phi \mod \pi) \neq 0$, the cross-correlation between the two waveguide propagation directions will reveal interference features unique to a multi-mode, multi-emitter system.

The collective emission behavior can be understood via a cascaded decay diagram shown in Fig. 10.4(c). Starting with the two-emitter excited state $|ee\rangle$, emission into the clockwise mode projects the emitters into the superposition state $(e^{i\phi}|eg\rangle + |ge\rangle)/\sqrt{2}$. From this state, decay via clockwise emission proceeds with the superradiant rate $2\Gamma$, where $\Gamma$ is the unmodified single-emitter decay rate into a propagating mode. In contrast, the rate of counterclockwise emission is modified by $\cos^2\phi$, as follows from the transition amplitude $\langle gg|\,(e^{i\phi}\sigma_A + \sigma_B)(e^{i\phi}|eg\rangle + |ge\rangle)/\sqrt{2}$. When

$\cos^2\phi = 0$, photons leave the resonator always in the same direction, which corresponds to perfect antibunching in the cross-correlation. For $\cos^2\phi = \pm 1$, the cross-correlation is identical to the autocorrelation on a single waveguide direction. These cases are illustrated in Fig. 10.4(d). The correlation measurements (Fig. 10.4(a,b)) are fit to a reduced five-level emitter model [151, 53, 19] with free parameters of excitation power, $\phi$, cavity detuning, and background noise. The presence of background noise from the above-resonant excitation reduces the interference contrast.

In conclusion, we have demonstrated near-unity cooperativity between a color center and a microresonator fabricated in a wafer-scalable, CMOS-compatible semiconductor photonics platform. Additionally, we observe two-photon superradiance between two SiC color centers. The integration of $V_{Si}$ into state-of-the-art microring resonators [46] and high-confinement photonic crystal cavities [15] would enable deterministic emitter-photon interactions in SiC. Taken together with the recent demonstrations of nuclear spin control [154, 145], wide spectral tuning via electric fields [110, 53] and single-shot readout [165], SiC satisfies the prerequisites to implement a fully-monolithic quantum photonic processor. The maintained spin-optical coherence of the $V_{Si}$ at elevated temperatures of up to 20 K [145, 166] offers an additional degree of flexibility for operation with low-cost cryogenic systems. Finally, the spectral stability of the $V_{Si}$, despite its substantial dipole moment [53], suggests that a first-order insensitivity to electric fields is not a prerequisite for color center compatibility with nanostructures.

## 10.4 Technological outlook

Most advanced spin-defect experiments to-date rely on the strategy of coupling emitted photons directly into an optical fiber. However, for applications other than fiber network communications, a photon in a fiber is not an advantage over a photon in an integrated waveguide: Practical realization of the key components for quantum networks actually plays to the strengths of integrated photonics rather than fiber optics. Integrated photonics have already achieved system complexity beyond what can be practically realized in macroscopic fiber-based devices, integrating hundreds of elements with mean fidelities of linear components exceeding 99.9% [167]. On-chip integration of single-photon detectors has seen remarkable progress in recent years [168, 169, 170], and integration with photonic resonators will likely enable narrowband integrated single photon detection with efficiencies exceeding 99% in the near future. The chip-integrated approach may prove to be the most promising for large-scale quantum systems. This architecture is illustrated in Fig. 10.5.

In this fully-monolithic realization of chip-integrated spin-based quantum technologies, the photon never leaves the chip, never couples into a fiber or passes through lossy bulk active elements, and is not subject to system fluctuations inherent in a large-scale macroscopic system. In fact, the photon never leaves the waveguide into which the quantum node emitted it, because switching, interference, and detection can all be realized in a waveguide geometry [169, 167]. Compact and efficient on-chip

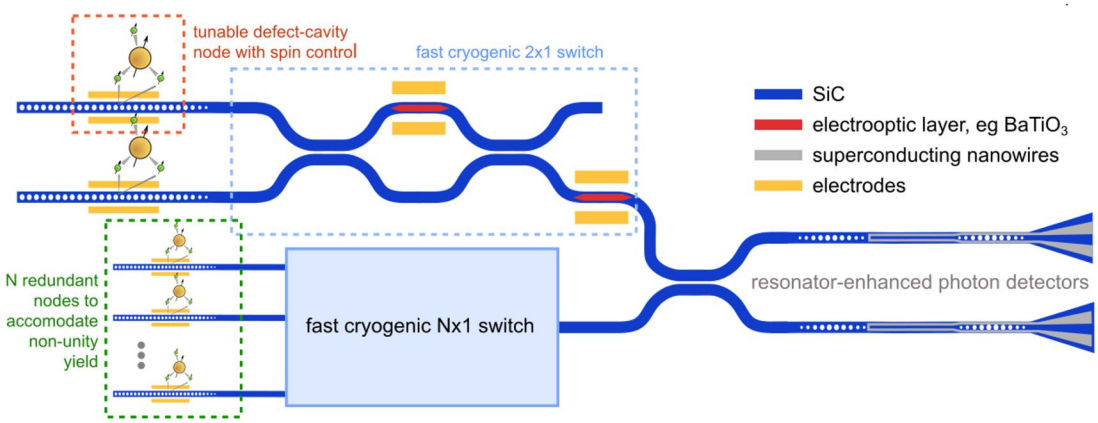


Figure 10.5: **Quantum photonic processor.**A conceptual diagram demonstrating how the example photonic network shown in Fig. 4.1b could be realized in a fully monolithic platform. In order to account for non-unity fabrication yield, $N$ redundant nodes are fabricated in the place of one node, and a Nx1 switch (composed of cascaded 2x1 switches) selects one working node.

photon detectors can be placed anywhere in the integrated circuit to convert a (fragile) quantum signal into a (robust) classical signal which can be routed off-chip via standard CMOS electronics such as vias and buried electrical layers, aiding in the realization of circuit connectivity. The relative simplicity of the integrated approach is a source of optimism for satisfying the extremely low loss requirements of useful quantum photonic computation.

SiC-on-insulator is a promising candidate to realize a fully-integrated defect-based quantum photonic processor, using high Q/V photonic crystal cavities, fast cryogenic optical modulators, and integrated detectors. In order to overcome the challenge of non-unity yield, each quantum node may consist of $N$ redundant cavity-coupled spin-defect elements coupled to a bus waveguide. Using this configuration, one can achieve post-selection without any additional cavity-waveguide losses, by tuning all but one working node away from the quantum network operation frequency. If necessary, a similar approach can be employed for post-selection of detectors (which are to be integrated with low-Q resonators or long waveguides to maximize photon absorption probability). Each node is electrically interfaced to tune the defect optical transition and to coherently manipulate the spin. Fast cryogenic modulators and switches based on a directional coupler or resonator drop-filter configuration can be integrated directly into the SiC platform, taking advantage of its electrooptic effect. Cryogenic integration based on this approach has only recently been demonstrated [171]. To increase the bandwidth and decrease the footprint, an additional electro-optically active layer, such as barium titanate ($BaTiO_3$) [171], can be sputtered and patterned in an adiabatic taper atop the SiC waveguide to minimize scattering loss. Finally, regardless of the optical frequency of operation of the quantum processor, efficient frequency conversion to the telecommunications band using the strong intrinsic second-order nonlinearity of SiC (12 pm/V) [90] would prepare the optically-encoded

quantum information for long-distance communication.

# Conclusion

In Part I of this Dissertation, we started from the signal-idler quantum comb with a monochromatic pump to build up a linearized formalism for describing the quantum fluctuations across the comb. We extended this model to the multimode case describing the dissipative Kerr soliton. We then used two-photon correlation measurements to validate this model for the below-threshold lines of soliton crystals and study the correlations of states leading up to soliton formation. Identifying the validity of the model permitted us to then theoretically study the structure and degree of quadrature squeezing that exists across the below-threshold modes. Using a multimode squeezing formalism (Bloch-Messiah decomposition), we found that a soliton crystal microcomb state across its entire stability region features a high degree of quadrature squeezing in a supermode structure dominated by two modes. We also found evidence that soliton crystals appear to decay in a coherent manner as a threshold process: this result establishes that the squeezed supermode analysis of the below-threshold quantum light is a means to gain further insight into classical comb dynamics. We note that we have considered the simplest realistic configuration for soliton crystal formation. Additional work must be done to analyze the effects of Raman scattering [113, 68] and higher order dispersion on the squeezing structure.

To experimentally test the findings of this work, several techniques may be applied. Measuring the evolution of second-order photon correlations [46] across the step would validate the existence of the threshold process as well as the formation of twin quantum combs. Coherence broadening of an autocorrelation measurement at the end of the soliton crystal step, as observed in Chapter 2, would provide evidence for the coherent threshold phenomenon. In the same autocorrelation, observation of a bichromatic beatnote with the coherence of the quantum light would provide evidence for the twin quantum combs.

Ultrafast imaging [7] could be used to observe the soliton crystal decay and potentially identify whether the macroscopic state evolution reveals the distinction between the annihilation of soliton crystals and non-crystallized multi-soliton states. A question of fundamental importance is whether ($N > 3$)-FSR soliton crystals decay with specific selection rules. This could be readily studied with the imaging measurement. Finally, the photonic molecule device proposed here for direct measurement of out-coupled squeezing can be readily fabricated using current experimental capabilities

[46, 72, 8, 66, 70, 71].

This study may also serve as a starting point for exploring the process by which the linearized model breaks down. The unbounded growth of twin quantum combs in a soliton crystal transitioning to the single soliton state is an unreconciled discontinuity within the linearized model. The experimental observation of this discontinuity may give insights into the quantum parametric processes in Kerr microcombs beyond the linearized model [37].

In Part II of this Dissertation, we have described various experimental demonstrations of nonlinear photonics using the SiCOI platform. The second-order nonlinearity was used for resonant second-harmonic generation (SHG) in microring resonators, and then again for non-resonant SHG in waveguides designed for supercontinuum generation. The third-order nonlinearity was employed in Kerr comb and soliton microcomb generation, which enabled the quantum optics study in Part I of this thesis, as well as supercontinuum generation with the comb extending into the mid-infrared. Finally, we study multi-emitter multi-mode cavity quantum electrodynamics by collective coupling of optically-addressable defects mediated by a thin-film whispering gallery mode resonator. As may have been gathered by the motivations throughout these chapters, SiC is unique in its combination of several material properties, and, with continued development will likely grow in its appeal both for technological applications and fundamental studies.

Going forward, an exciting direction is to combine strongly-coupled defects and nonlinear light generation in the same photonic resonator to explore new physical phenomena that were previously possible to study only theoretically. For example, below-threshold OPO may be used for generating entanglement with emitters, where one mode of the signal-idler pair is resonant with an emitter ensemble [172]. Another direction is *in situ* generation of a single-mode squeezed state and its coupling to indistinguishable few-emitter ensembles. Via bichromatic pumping of the neighboring modes and careful control of the relative detunings, strong degenerate squeezing [64] may be generated in the resonator mode used for Purcell enhancement of the emitters.

# Bibliography


[1] T. Herr, V. Brasch, J. D. Jost, C. Y. Wang, N. M. Kondratiev, M. L. Gorodetsky, and T. J. Kippenberg, "Temporal solitons in optical microresonators," *Nature Photonics*, vol. 8, no. 2, pp. 145–152, 2014.

[2] M.-G. Suh, Q.-F. Yang, K. Y. Yang, X. Yi, and K. J. Vahala, "Microresonator soliton dual-comb spectroscopy," *Science*, vol. 354, no. 6312, pp. 600–603, 2016.

[3] J. Riemensberger, A. Lukashchuk, M. Karpov, W. Weng, E. Lucas, J. Liu, and T. J. Kippenberg, "Massively parallel coherent laser ranging using a soliton microcomb," *Nature*, vol. 581, no. 7807, pp. 164–170, 2020.

[4] B. Corcoran, M. Tan, X. Xu, A. Boes, J. Wu, T. G. Nguyen, S. T. Chu, B. E. Little, R. Morandotti, A. Mitchell, *et al.*, "Ultra-dense optical data transmission over standard fibre with a single chip source," *Nature Communications*, vol. 11, no. 1, p. 2568, 2020.

[5] J. Feldmann, N. Youngblood, M. Karpov, H. Gehring, X. Li, M. Stappers, M. Le Gallo, X. Fu, A. Lukashchuk, A. Raja, *et al.*, "Parallel convolutional processing using an integrated photonic tensor core," *Nature*, vol. 589, no. 7840, pp. 52–58, 2021.

[6] Q.-F. Yang, X. Yi, K. Y. Yang, and K. Vahala, "Counter-propagating solitons in microresonators," *Nature Photonics*, vol. 11, no. 9, pp. 560–564, 2017.

[7] X. Yi, Q.-F. Yang, K. Y. Yang, and K. Vahala, "Imaging soliton dynamics in optical microcavities," *Nature communications*, vol. 9, no. 1, pp. 1–8, 2018.

[8] M. Karpov, M. H. Pfeiffer, H. Guo, W. Weng, J. Liu, and T. J. Kippenberg, "Dynamics of soliton crystals in optical microresonators," *Nature Physics*, vol. 15, no. 10, pp. 1071–1077, 2019.

[9] C. Bao, M.-G. Suh, B. Shen, K. Şafak, A. Dai, H. Wang, L. Wu, Z. Yuan, Q.-F. Yang, A. B. Matsko, *et al.*, "Quantum diffusion of microcavity solitons," *Nature Physics*, pp. 1–5, 2021.

[10] M. A. Guidry, K. Y. Yang, D. M. Lukin, A. Markosyan, J. Yang, M. M. Fejer, and J. Vučković, "Optical parametric oscillation in silicon carbide nanophotonics," *Optica*, vol. 7, no. 9, pp. 1139–1142, 2020.

[11] B.-S. Song, S. Yamada, T. Asano, and S. Noda, "Demonstration of two-dimensional photonic crystals based on silicon carbide," *Optics express*, vol. 19, no. 12, pp. 11084–11089, 2011.

[12] J. Cardenas, M. Zhang, C. T. Phare, S. Y. Shah, C. B. Poitras, B. Guha, and M. Lipson, "High Q SiC microresonators," *Optics express*, vol. 21, no. 14, pp. 16882–16887, 2013.

[13] T. Fan, H. Moradinejad, X. Wu, A. A. Eftekhar, and A. Adibi, "High-Q integrated photonic microresonators on 3C-SiC-on-insulator (SiCOI) platform," *Optics express*, vol. 26, no. 20, pp. 25814–25826, 2018.

[14] T. Fan, X. Wu, A. A. Eftekhar, M. Bosi, H. Moradinejad, E. V. Woods, and A. Adibi, "High-quality integrated microdisk resonators in the visible-to-near-infrared wavelength range on a 3C-silicon carbide-on-insulator platform," *Optics Letters*, vol. 45, no. 1, pp. 153–156, 2020.

[15] B.-S. Song, T. Asano, S. Jeon, H. Kim, C. Chen, D. D. Kang, and S. Noda, "Ultrahigh-Q photonic crystal nanocavities based on 4H silicon carbide," *Optica*, vol. 6, no. 8, pp. 991–995, 2019.

[16] D. M. Lukin, C. Dory, M. A. Guidry, K. Y. Yang, S. D. Mishra, R. Trivedi, M. Radulaski, S. Sun, D. Vercruysse, G. H. Ahn, *et al.*, "4H-silicon-carbide-on-insulator for integrated quantum and nonlinear photonics," *Nature Photonics*, vol. 14, no. 5, pp. 330–334, 2020.

[17] D. M. Lukin, M. A. Guidry, and J. Vučković, "Integrated quantum photonics with silicon carbide: challenges and prospects," *PRX Quantum*, vol. 1, no. 2, p. 020102, 2020.

[18] A. Markosyan, R. Route, M. Fejer, D. Patel, and C. Menoni, "Study of spontaneous and induced absorption in amorphous Ta2O5 and SiO2 dielectric thin films," *Journal of Applied Physics*, vol. 113, no. 13, p. 133104, 2013.

[19] D. Liu, F. Kaiser, V. Bushmakin, E. Hesselmeier, T. Steidl, T. Ohshima, N. T. Son, J. Ul-Hassan, Ö. O. Soykal, and J. Wrachtrup, "The silicon vacancy centers in SiC: determination of intrinsic spin dynamics for integrated quantum photonics," *arXiv preprint arXiv:2307.13648*, 2023.

[20] L. Lugiato, F. Prati, M. Gorodetsky, and T. Kippenberg, "From the Lugiato–Lefever equation to microresonator-based soliton Kerr frequency combs," *Philosophical Transactions of the Royal Society A: Mathematical, Physical and Engineering Sciences*, vol. 376, no. 2135, p. 20180113, 2018.

[21] S. Akhmanov, A. Sukhorukov, and A. Chirkin, "Nonstationary phenomena and space-time analogy in nonlinear optics," *Sov. Phys. JETP*, vol. 28, no. 4, pp. 748–757, 1969.

[22] L. F. Mollenauer, R. H. Stolen, and J. P. Gordon, "Experimental observation of picosecond pulse narrowing and solitons in optical fibers," *Physical Review Letters*, vol. 45, no. 13, p. 1095, 1980.

[23] Y. K. Chembo and C. R. Menyuk, "Spatiotemporal Lugiato-Lefever formalism for Kerr-comb generation in whispering-gallery-mode resonators," *Physical Review A*, vol. 87, no. 5, p. 053852, 2013.

[24] T. Herr, K. Hartinger, J. Riemensberger, C. Wang, E. Gavartin, R. Holzwarth, M. Gorodetsky, and T. Kippenberg, "Universal formation dynamics and noise of Kerr-frequency combs in microresonators," *Nature photonics*, vol. 6, no. 7, pp. 480–487, 2012.

[25] C. Reimer, M. Kues, P. Roztocki, B. Wetzel, F. Grazioso, B. E. Little, S. T. Chu, T. Johnston, Y. Bromberg, L. Caspani, *et al.*, "Generation of multiphoton entangled quantum states by means of integrated frequency combs," *Science*, vol. 351, no. 6278, pp. 1176–1180, 2016.

[26] M. Kues, C. Reimer, J. M. Lukens, W. J. Munro, A. M. Weiner, D. J. Moss, and R. Morandotti, "Quantum optical microcombs," *Nature Photonics*, vol. 13, no. 3, pp. 170–179, 2019.

[27] L. Caspani, C. Xiong, B. J. Eggleton, D. Bajoni, M. Liscidini, M. Galli, R. Morandotti, and D. J. Moss, "Integrated sources of photon quantum states based on nonlinear optics," *Light: Science & Applications*, vol. 6, no. 11, pp. e17100–e17100, 2017.

[28] C. W. Gardiner and M. J. Collett, "Input and output in damped quantum systems: Quantum stochastic differential equations and the master equation," *Physical Review A*, vol. 31, pp. 3761–3774, Jun 1985.

[29] Z. Ou and Y. Lu, "Cavity enhanced spontaneous parametric down-conversion for the prolongation of correlation time between conjugate photons," *Physical Review Letters*, vol. 83, no. 13, p. 2556, 1999.

[30] H. Carmichael, *An open systems approach to quantum optics: lectures presented at the Université Libre de Bruxelles, October 28 to November 4, 1991*, vol. 18. Springer Science & Business Media, 2009.

[31] G. Moille, X. Lu, A. Rao, Q. Li, D. A. Westly, L. Ranzani, S. B. Papp, M. Soltani, and K. Srinivasan, "Kerr-microresonator soliton frequency combs at cryogenic temperatures," *Physical Review Applied*, vol. 12, no. 3, p. 034057, 2019.

[32] Y. K. Chembo, "Quantum dynamics of Kerr optical frequency combs below and above threshold: Spontaneous four-wave mixing, entanglement, and squeezed states of light," *Physical Review A*, vol. 93, no. 3, p. 033820, 2016.

[33] Z. Vernon and J. Sipe, "Strongly driven nonlinear quantum optics in microring resonators," *Physical Review A*, vol. 92, no. 3, p. 033840, 2015.

[34] C. Navarrete-Benlloch, E. Roldán, Y. Chang, and T. Shi, "Regularized linearization for quantum nonlinear optical cavities: application to degenerate optical parametric oscillators," *Optics express*, vol. 22, no. 20, pp. 24010–24023, 2014.

[35] Z. Yang, M. Jahanbozorgi, D. Jeong, S. Sun, O. Pfister, H. Lee, and X. Yi, "A squeezed quantum microcomb on a chip," *Nature Communications*, vol. 12, no. 1, pp. 1–8, 2021.

[36] A. S. Villar, K. N. Cassemiro, K. Dechoum, A. Z. Khoury, M. Martinelli, and P. Nussenzveig, "Entanglement in the above-threshold optical parametric oscillator," *JOSA B*, vol. 24, no. 2, pp. 249–256, 2007.

[37] E. Ng, R. Yanagimoto, M. Jankowski, M. Fejer, and H. Mabuchi, "Quantum noise dynamics in nonlinear pulse propagation," *arXiv preprint arXiv:2307.05464*, 2023.

[38] M. Wolinsky and H. Carmichael, "Quantum noise in the parametric oscillator: from squeezed states to coherent-state superpositions," *Physical review letters*, vol. 60, no. 18, p. 1836, 1988.

[39] B. Vlastakis, G. Kirchmair, Z. Leghtas, S. E. Nigg, L. Frunzio, S. M. Girvin, M. Mirrahimi, M. H. Devoret, and R. J. Schoelkopf, "Deterministically encoding quantum information using 100-photon Schrödinger cat states," *Science*, vol. 342, no. 6158, pp. 607–610, 2013.

[40] G. Kirchmair, B. Vlastakis, Z. Leghtas, S. E. Nigg, H. Paik, E. Ginossar, M. Mirrahimi, L. Frunzio, S. M. Girvin, and R. J. Schoelkopf, "Observation of quantum state collapse and revival due to the single-photon Kerr effect," *Nature*, vol. 495, no. 7440, pp. 205–209, 2013.

[41] S. Deleglise, I. Dotsenko, C. Sayrin, J. Bernu, M. Brune, J.-M. Raimond, and S. Haroche, "Reconstruction of non-classical cavity field states with snapshots of their decoherence," *Nature*, vol. 455, no. 7212, pp. 510–514, 2008.

[42] A. Marandi, Z. Wang, K. Takata, R. L. Byer, and Y. Yamamoto, "Network of time-multiplexed optical parametric oscillators as a coherent Ising machine," *Nature Photonics*, vol. 8, no. 12, pp. 937–942, 2014.

[43] Y. Yamamoto, K. Aihara, T. Leleu, K.-i. Kawarabayashi, S. Kako, M. Fejer, K. Inoue, and H. Takesue, "Coherent Ising machines—Optical neural networks operating at the quantum limit," *npj Quantum Information*, vol. 3, no. 1, p. 49, 2017.

[44] A. Dutt, K. Luke, S. Manipatruni, A. L. Gaeta, P. Nussenzveig, and M. Lipson, "On-chip optical squeezing," *Physical Review Applied*, vol. 3, no. 4, p. 044005, 2015.

[45] M. A. Guidry, D. M. Lukin, K. Y. Yang, and J. Vučković, "Multimode squeezing in soliton crystal microcombs," *Optica*, vol. 10, no. 6, pp. 694–701, 2023.

[46] M. A. Guidry, D. M. Lukin, K. Y. Yang, R. Trivedi, and J. Vučković, "Quantum optics of soliton microcombs," *Nature Photonics*, vol. 16, no. 1, pp. 52–58, 2022.

[47] A. B. Matsko and L. Maleki, "On timing jitter of mode locked Kerr frequency combs," *Optics express*, vol. 21, no. 23, pp. 28862–28876, 2013.

[48] D. C. Cole, E. S. Lamb, P. Del'Haye, S. A. Diddams, and S. B. Papp, "Soliton crystals in Kerr resonators," *Nature Photonics*, vol. 11, no. 10, pp. 671–676, 2017.

[49] M. Karpov, M. H. Pfeiffer, H. Guo, W. Weng, J. Liu, and T. J. Kippenberg, "Dynamics of soliton crystals in optical microresonators," *Nature Physics*, vol. 15, no. 10, pp. 1071–1077, 2019.

[50] A. Coillet, Z. Qi, I. V. Balakireva, G. Lin, C. R. Menyuk, and Y. K. Chembo, "On the transition to secondary Kerr combs in whispering-gallery mode resonators," *Optics letters*, vol. 44, no. 12, pp. 3078–3081, 2019.

[51] T. F. da Silva, G. C. do Amaral, D. Vitoreti, G. P. Temporão, and J. P. von der Weid, "Spectral characterization of weak coherent state sources based on two-photon interference," *JOSA B*, vol. 32, no. 4, pp. 545–549, 2015.

[52] C. Navarrete-Benlloch, R. Garcés, N. Mohseni, and G. de Valcárcel, "Floquet theory for temporal correlations and spectra in time-periodic open quantum systems: Application to squeezed parametric oscillation beyond the rotating-wave approximation," *Physical Review A*, vol. 103, no. 2, p. 023713, 2021.

[53] D. M. Lukin, A. D. White, R. Trivedi, M. A. Guidry, N. Morioka, C. Babin, Ö. O. Soykal, J. Ul-Hassan, N. T. Son, T. Ohshima, *et al.*, "Spectrally reconfigurable quantum emitters enabled by optimized fast modulation," *npj Quantum Information*, vol. 6, no. 1, pp. 1–9, 2020.

[54] G. Vidal and R. F. Werner, "Computable measure of entanglement," *Physical Review A*, vol. 65, no. 3, p. 032314, 2002.

[55] M. Zhang, C. Wang, Y. Hu, A. Shams-Ansari, T. Ren, S. Fan, and M. Lončar, "Electronically programmable photonic molecule," *Nature Photonics*, vol. 13, no. 1, pp. 36–40, 2019.

[56] Ó. B. Helgason, F. R. Arteaga-Sierra, Z. Ye, K. Twayana, P. A. Andrekson, M. Karlsson, J. Schröder, and V. Torres-Company, "Dissipative solitons in photonic molecules," *Nature Photonics*, pp. 1–6, 2021.

[57] M. Kues, C. Reimer, P. Roztocki, L. R. Cortés, S. Sciara, B. Wetzel, Y. Zhang, A. Cino, S. T. Chu, B. E. Little, *et al.*, "On-chip generation of high-dimensional entangled quantum states and their coherent control," *Nature*, vol. 546, no. 7660, pp. 622–626, 2017.

[58] G. J. De Valcarcel, G. Patera, N. Treps, and C. Fabre, "Multimode squeezing of frequency combs," *Physical Review A*, vol. 74, no. 6, p. 061801, 2006.

[59] G. Patera, N. Treps, C. Fabre, and G. J. De Valcarcel, "Quantum theory of synchronously pumped type I optical parametric oscillators: characterization of the squeezed supermodes," *The European Physical Journal D*, vol. 56, no. 1, pp. 123–140, 2010.

[60] J. Roslund, R. M. De Araujo, S. Jiang, C. Fabre, and N. Treps, "Wavelength-multiplexed quantum networks with ultrafast frequency combs," *Nature Photonics*, vol. 8, no. 2, pp. 109–112, 2014.

[61] Y. Cai, J. Roslund, G. Ferrini, F. Arzani, X. Xu, C. Fabre, and N. Treps, "Multimode entanglement in reconfigurable graph states using optical frequency combs," *Nature communications*, vol. 8, no. 1, pp. 1–9, 2017.

[62] Y.-S. Ra, A. Dufour, M. Walschaers, C. Jacquard, T. Michel, C. Fabre, and N. Treps, "Non-gaussian quantum states of a multimode light field," *Nature Physics*, vol. 16, no. 2, pp. 144–147, 2020.

[63] Z. Vernon, N. Quesada, M. Liscidini, B. Morrison, M. Menotti, K. Tan, and J. Sipe, "Scalable squeezed-light source for continuous-variable quantum sampling," *Physical Review Applied*, vol. 12, no. 6, p. 064024, 2019.

[64] Y. Zhao, Y. Okawachi, J. K. Jang, X. Ji, M. Lipson, and A. L. Gaeta, "Near-degenerate quadrature-squeezed vacuum generation on a silicon-nitride chip," *Physical Review Letters*, vol. 124, no. 19, p. 193601, 2020.

[65] É. Gouzien, L. Labonté, J. Etesse, A. Zavatta, S. Tanzilli, V. d'Auria, and G. Patera, "Hidden and detectable squeezing from microresonators," *Physical Review Research*, vol. 5, no. 2, p. 023178, 2023.

[66] D. C. Cole, E. S. Lamb, P. Del'Haye, S. A. Diddams, and S. B. Papp, "Soliton crystals in Kerr resonators," *Nature Photonics*, vol. 11, no. 10, pp. 671–676, 2017.

[67] E. Gouzien, S. Tanzilli, V. d'Auria, and G. Patera, "Morphing supermodes: a full characterization for enabling multimode quantum optics," *Physical Review Letters*, vol. 125, no. 10, p. 103601, 2020.

[68] A. Hosaka, T. Kawamori, and F. Kannari, "Multimode quantum theory of nonlinear propagation in optical fibers," *Physical Review A*, vol. 94, no. 5, p. 053833, 2016.

[69] J. Junker, D. Wilken, N. Johny, D. Steinmeyer, and M. Heurs, "Frequency-dependent squeezing from a detuned squeezer," *Physical Review Letters*, vol. 129, no. 3, p. 033602, 2022.

[70] Y. He, J. Ling, M. Li, and Q. Lin, "Perfect soliton crystals on demand," *Laser & Photonics Reviews*, vol. 14, no. 8, p. 1900339, 2020.

[71] Z. Gong, X. Liu, Y. Xu, and H. X. Tang, "Near-octave lithium niobate soliton microcomb," *Optica*, vol. 7, no. 10, pp. 1275–1278, 2020.

[72] H. Jung, S.-P. Yu, D. R. Carlson, T. E. Drake, T. C. Briles, and S. B. Papp, "Tantala Kerr nonlinear integrated photonics," *Optica*, vol. 8, no. 6, pp. 811–817, 2021.

[73] R. S. Bennink and R. W. Boyd, "Improved measurement of multimode squeezed light via an eigenmode approach," *Physical Review A*, vol. 66, no. 5, p. 053815, 2002.

[74] P. Del'Haye, S. B. Papp, and S. A. Diddams, "Hybrid electro-optically modulated microcombs," *Physical review letters*, vol. 109, no. 26, p. 263901, 2012.

[75] M. Zhang, B. Buscaino, C. Wang, A. Shams-Ansari, C. Reimer, R. Zhu, J. M. Kahn, and M. Lončar, "Broadband electro-optic frequency comb generation in a lithium niobate microring resonator," *Nature*, vol. 568, no. 7752, pp. 373–377, 2019.

[76] G. Liang, H. Huang, A. Mohanty, M. C. Shin, X. Ji, M. J. Carter, S. Shrestha, M. Lipson, and N. Yu, "Robust, efficient, micrometre-scale phase modulators at visible wavelengths," *Nature Photonics*, vol. 15, no. 12, pp. 908–913, 2021.

[77] Y. Liu, Z. Qiu, X. Ji, A. Lukashchuk, J. He, J. Riemensberger, M. Hafermann, R. N. Wang, J. Liu, C. Ronning, *et al.*, "A photonic integrated circuit–based erbium-doped amplifier," *Science*, vol. 376, no. 6599, pp. 1309–1313, 2022.

[78] L. Di Cioccio, F. Letertre, Y. Le Tiec, A. Papon, C. Jaussaud, and M. Bruel, "Silicon carbide on insulator formation by the Smart-Cut process," *Materials Science and Engineering: B*, vol. 46, no. 1-3, pp. 349–356, 1997.

[79] S. Yamada, B.-S. Song, S. Jeon, J. Upham, Y. Tanaka, T. Asano, and S. Noda, "Second-harmonic generation in a silicon-carbide-based photonic crystal nanocavity," *Optics letters*, vol. 39, no. 7, pp. 1768–1771, 2014.

[80] J. Cardenas, M. Yu, Y. Okawachi, C. B. Poitras, R. K. Lau, A. Dutt, A. L. Gaeta, and M. Lipson, "Optical nonlinearities in high-confinement silicon carbide waveguides," *Optics Letters*, vol. 40, no. 17, pp. 4138–4141, 2015.

[81] A. Yi, Y. Zheng, H. Huang, J. Lin, Y. Yan, T. You, K. Huang, S. Zhang, C. Shen, M. Zhou, *et al.*, "Wafer-scale 4H-silicon carbide-on-insulator (4H–SiCOI) platform for nonlinear integrated optical devices," *Optical Materials*, p. 109990, 2020.

[82] Y. Zheng, M. Pu, A. Yi, B. Chang, T. You, K. Huang, A. N. Kamel, M. R. Henriksen, A. A. Jørgensen, X. Ou, *et al.*, "High-quality factor, high-confinement microring resonators in 4H-silicon carbide-on-insulator," *Optics express*, vol. 27, no. 9, pp. 13053–13060, 2019.

[83] M. Radulaski, T. M. Babinec, S. Buckley, A. Rundquist, J. Provine, K. Alassaad, G. Ferro, and J. Vučković, "Photonic crystal cavities in cubic (3C) polytype silicon carbide films," *Optics express*, vol. 21, no. 26, pp. 32623–32629, 2013.

[84] X. Lu, J. Y. Lee, P. X.-L. Feng, and Q. Lin, "High Q silicon carbide microdisk resonator," *Applied Physics Letters*, vol. 104, no. 18, p. 181103, 2014.

[85] J. S. Pelc, *Frequency conversion of single photons: physics, devices, and applications*. Stanford University, 2012.

[86] T. P. McKenna, H. S. Stokowski, V. Ansari, J. Mishra, M. Jankowski, C. J. Sarabalis, J. F. Herrmann, C. Langrock, M. M. Fejer, and A. H. Safavi-Naeini, "Ultra-low-power second-order nonlinear optics on a chip," *Nature Communications*, vol. 13, no. 1, p. 4532, 2022.

[87] C. Wang, J. Li, A. Yi, Z. Fang, L. Zhou, Z. Wang, R. Niu, Y. Chen, J. Zhang, Y. Cheng, *et al.*, "Soliton formation and spectral translation into visible on CMOS-compatible 4H-silicon-carbide-on-insulator platform," *Light: Science & Applications*, vol. 11, no. 1, p. 341, 2022.

[88] Y. Okawachi, M. Yu, B. Desiatov, B. Y. Kim, T. Hansson, M. Lončar, and A. L. Gaeta, "Chip-based self-referencing using integrated lithium niobate waveguides," *Optica*, vol. 7, no. 6, pp. 702–707, 2020.

[89] E. Bersin, M. Sutula, Y. Q. Huan, A. Suleymanzade, D. R. Assumpcao, Y.-C. Wei, P.-J. Stas, C. M. Knaut, E. N. Knall, C. Langrock, *et al.*, "Telecom networking with a diamond quantum memory," *arXiv preprint arXiv:2307.08619*, 2023.

[90] H. Sato, M. Abe, I. Shoji, J. Suda, and T. Kondo, "Accurate measurements of second-order nonlinear optical coefficients of 6H and 4H silicon carbide," *JOSA B*, vol. 26, no. 10, pp. 1892–1896, 2009.

[91] D. S. Hum and M. M. Fejer, "Quasi-phasematching," *Comptes Rendus Physique*, vol. 8, no. 2, pp. 180–198, 2007.

[92] S. Wang, M. Zhan, G. Wang, H. Xuan, W. Zhang, C. Liu, C. Xu, Y. Liu, Z. Wei, and X. Chen, "4H-SiC: a new nonlinear material for midinfrared lasers," *Laser & Photonics Reviews*, vol. 7, no. 5, pp. 831–838, 2013.

[93] C. Dory, D. Vercruysse, K. Y. Yang, N. V. Sapra, A. E. Rugar, S. Sun, D. M. Lukin, A. Y. Piggott, J. L. Zhang, M. Radulaski, *et al.*, "Inverse-designed diamond photonics," *Nature communications*, vol. 10, no. 1, p. 3309, 2019.

[94] A. Rodriguez, M. Soljačić, J. D. Joannopoulos, and S. G. Johnson, "$\chi(2)$ and $\chi(3)$ harmonic generation at a critical power in inhomogeneous doubly resonant cavities," *Optics express*, vol. 15, no. 12, pp. 7303–7318, 2007.

[95] S. Buckley, *Engineering Photonic Crystal Cavities in III-V Semiconductors for $\chi(2)$ Frequency Conversion*. Stanford University, 2014.

[96] R. Luo, Y. He, H. Liang, M. Li, J. Ling, and Q. Lin, "Optical parametric generation in a lithium niobate microring with modal phase matching," *Physical Review Applied*, vol. 11, no. 3, p. 034026, 2019.

[97] J. Yang, M. A. Guidry, D. M. Lukin, K. Yang, and J. Vučković, "Inverse-designed silicon carbide quantum and nonlinear photonics," *Light: Science & Applications*, vol. 12, no. 1, p. 201, 2023.

[98] L. Deniel, M. A. Guidry, D. M. Lukin, K. Y. Yang, J. Yang, J. Vučković, T. W. Hänsch, and N. Picqué, "Visible to Mid-infrared Supercontinuum Generation in 4H-Silicon-Carbide Nanophotonic Waveguides," in *CLEO: Science and Innovations*, pp. STh1F–4, Optica Publishing Group, 2023.

[99] K. De Greve, L. Yu, P. L. McMahon, J. S. Pelc, C. M. Natarajan, N. Y. Kim, E. Abe, S. Maier, C. Schneider, M. Kamp, *et al.*, "Quantum-dot spin–photon entanglement via frequency downconversion to telecom wavelength," *Nature*, vol. 491, no. 7424, pp. 421–425, 2012.

[100] X. Lu, G. Moille, Q. Li, D. A. Westly, A. Singh, A. Rao, S.-P. Yu, T. C. Briles, S. B. Papp, and K. Srinivasan, "Efficient telecom-to-visible spectral translation through ultralow power nonlinear nanophotonics," *Nature Photonics*, vol. 13, no. 9, pp. 593–601, 2019.

[101] L. Su, D. Vercruysse, J. Skarda, N. V. Sapra, J. A. Petykiewicz, and J. Vučković, "Nanophotonic inverse design with spins: Software architecture and practical considerations," *Applied Physics Reviews*, vol. 7, no. 1, p. 011407, 2020.

[102] W. Haynes, "CRC Handbook of Chemistry and Physics 92nd edition CRC press," 2011.

[103] R. Wei, S. Song, K. Yang, Y. Cui, Y. Peng, X. Chen, X. Hu, and X. Xu, "Thermal conductivity of 4H-SiC single crystals," *Journal of Applied Physics*, vol. 113, no. 5, p. 053503, 2013.

[104] Z. Li and R. C. Bradt, "Thermal expansion of the hexagonal (4H) polytype of SiC," *Journal of Applied Physics*, vol. 60, no. 2, pp. 612–614, 1986.

[105] N. Watanabe, T. Kimoto, and J. Suda, "Thermo-optic coefficients of 4H-SiC, GaN, and AlN for ultraviolet to infrared regions up to 500°C," *Japanese Journal of Applied Physics*, vol. 51, no. 11R, p. 112101, 2012.

[106] S. A. Zargaleh, S. Hameau, B. Eble, F. Margaillan, H. J. von Bardeleben, J.-L. Cantin, and W. Gao, "Nitrogen vacancy center in cubic silicon carbide: A promising qubit in the 1.5 $\mu$m spectral range for photonic quantum networks," *Physical Review B*, vol. 98, no. 16, p. 165203, 2018.

[107] W. F. Koehl, B. B. Buckley, F. J. Heremans, G. Calusine, and D. D. Awschalom, "Room temperature coherent control of defect spin qubits in silicon carbide," *Nature*, vol. 479, no. 7371, pp. 84–87, 2011.

[108] M. Widmann, S. Lee, T. Rendler, N. T. Son, H. Fedder, S. Paik, L. Yang, N. Zhao, S. Yang, I. Booker, A. Denisenko, M. Jamali, S. Momenzadeh, I. Gerhardt, T. Ohshima, A. Gali, E. Janzen, and J. Wrachtrup, "Coherent control of single spins in silicon carbide at room temperature," *Nature Materials*, vol. 14, p. 164–168, 2015.

[109] R. Nagy, M. Niethammer, M. Widmann, Y.-C. Chen, P. Udvarhelyi, C. Bonato, J. U. Hassan, R. Karhu, I. G. Ivanov, N. T. Son, *et al.*, "High-fidelity spin and optical control of single silicon-vacancy centres in silicon carbide," *Nature Comm.*, vol. 10, no. 1, pp. 1–8, 2019.

[110] C. P. Anderson, A. Bourassa, K. C. Miao, G. Wolfowicz, P. J. Mintun, A. L. Crook, H. Abe, J. U. Hassan, N. T. Son, T. Ohshima, *et al.*, "Electrical and optical control of single spins integrated in scalable semiconductor devices," *Science*, vol. 366, no. 6470, pp. 1225–1230, 2019.

[111] T. Kippenberg, S. Spillane, and K. Vahala, "Kerr-nonlinearity optical parametric oscillation in an ultrahigh-Q toroid microcavity," *Physical review letters*, vol. 93, no. 8, p. 083904, 2004.

[112] X. Yi, Q.-F. Yang, K. Y. Yang, M.-G. Suh, and K. Vahala, "Soliton frequency comb at microwave rates in a high-q silica microresonator," *Optica*, vol. 2, no. 12, pp. 1078–1085, 2015.

[113] X. Yi, Q.-F. Yang, K. Y. Yang, and K. Vahala, "Theory and measurement of the soliton self-frequency shift and efficiency in optical microcavities," *Optics letters*, vol. 41, no. 15, pp. 3419–3422, 2016.

[114] X. Xue, Y. Xuan, Y. Liu, P.-H. Wang, S. Chen, J. Wang, D. E. Leaird, M. Qi, and A. M. Weiner, "Mode-locked dark pulse Kerr combs in normal-dispersion microresonators," *Nature Photonics*, vol. 9, no. 9, pp. 594–600, 2015.

[115] Y. Zheng, M. Pu, A. Yi, X. Ou, and H. Ou, "4H-SiC microring resonators for nonlinear integrated photonics," *Optics Letters*, vol. 44, pp. 5784–5787, 2019.

[116] X. Lu, J. Y. Lee, S. Rogers, and Q. Lin, "Optical Kerr nonlinearity in a high-Q silicon carbide microresonator," *Optics Express*, vol. 22, no. 25, pp. 30826–30832, 2014.

[117] J. Riemensberger, A. Lukashchuk, M. Karpov, W. Weng, E. Lucas, J. Liu, and T. J. Kippenberg, "Massively parallel coherent laser ranging using a soliton microcomb," *Nature*, vol. 581, no. 7807, pp. 164–170, 2020.

[118] D. T. Spencer, T. Drake, T. C. Briles, J. Stone, L. C. Sinclair, C. Fredrick, Q. Li, D. Westly, B. R. Ilic, A. Bluestone, *et al.*, "An optical-frequency synthesizer using integrated photonics," *Nature*, vol. 557, no. 7703, pp. 81–85, 2018.

[119] G. Moille, L. Chang, W. Xie, A. Rao, X. Lu, M. Davanco, J. E. Bowers, and K. Srinivasan, "Dissipative Kerr solitons in a III-V microresonator," *Laser & Photonics Reviews*, vol. 14, no. 8, p. 2000022, 2020.

[120] W. Jin, Q.-F. Yang, L. Chang, B. Shen, H. Wang, M. A. Leal, L. Wu, M. Gao, A. Feshali, M. Paniccia, *et al.*, "Hertz-linewidth semiconductor lasers using CMOS-ready ultra-high-Q microresonators," *Nature Photonics*, pp. 1–8, 2021.

[121] B. Stern, X. Ji, Y. Okawachi, A. L. Gaeta, and M. Lipson, "Battery-operated integrated frequency comb generator," *Nature*, vol. 562, no. 7727, pp. 401–405, 2018.

[122] J. Liu, A. S. Raja, M. Karpov, B. Ghadiani, M. H. Pfeiffer, B. Du, N. J. Engelsen, H. Guo, M. Zervas, and T. J. Kippenberg, "Ultralow-power chip-based soliton microcombs for photonic integration," *Optica*, vol. 5, no. 10, pp. 1347–1353, 2018.

[123] K. Y. Yang, D. Y. Oh, S. H. Lee, Q.-F. Yang, X. Yi, B. Shen, H. Wang, and K. Vahala, "Bridging ultrahigh-Q devices and photonic circuits," *Nature Photonics*, vol. 12, no. 5, pp. 297–302, 2018.

[124] Y. He, J. Ling, M. Li, and Q. Lin, "Perfect soliton crystals on demand," *Laser & Photonics Reviews*, vol. 14, no. 8, p. 1900339, 2020.

[125] L. Chang, W. Xie, H. Shu, Q.-F. Yang, B. Shen, A. Boes, J. D. Peters, W. Jin, C. Xiang, S. Liu, *et al.*, "Ultra-efficient frequency comb generation in AlGaAs-on-insulator microresonators," *Nature communications*, vol. 11, no. 1, pp. 1–8, 2020.

[126] C.-S. Brès, A. Della Torre, D. Grassani, V. Brasch, C. Grillet, and C. Monat, "Supercontinuum in integrated photonics: generation, applications, challenges, and perspectives," *Nanophotonics*, vol. 12, no. 7, pp. 1199–1244, 2023.

[127] H. Guo, C. Herkommer, A. Billat, D. Grassani, C. Zhang, M. H. Pfeiffer, W. Weng, C.-S. Brès, and T. J. Kippenberg, "Mid-infrared frequency comb via coherent dispersive wave generation in silicon nitride nanophotonic waveguides," *Nature Photonics*, vol. 12, no. 6, pp. 330–335, 2018.

[128] J. Lu, X. Liu, A. W. Bruch, L. Zhang, J. Wang, J. Yan, and H. X. Tang, "Ultraviolet to mid-infrared supercontinuum generation in single-crystalline aluminum nitride waveguides," *Optics Letters*, vol. 45, no. 16, pp. 4499–4502, 2020.

[129] M. Atatüre, D. Englund, N. Vamivakas, S.-Y. Lee, and J. Wrachtrup, "Material platforms for spin-based photonic quantum technologies," *Nature Reviews Materials*, vol. 3, no. 5, pp. 38–51, 2018.

[130] D. D. Awschalom, R. Hanson, J. Wrachtrup, and B. B. Zhou, "Quantum technologies with optically interfaced solid-state spins," *Nature Photonics*, vol. 12, no. 9, pp. 516–527, 2018.

[131] G. Wolfowicz, F. J. Heremans, C. P. Anderson, S. Kanai, H. Seo, A. Gali, G. Galli, and D. D. Awschalom, "Quantum guidelines for solid-state spin defects," *Nature Reviews Materials*, pp. 906–925, 2021.

[132] M. Pompili, S. L. Hermans, S. Baier, H. K. Beukers, P. C. Humphreys, R. N. Schouten, R. F. Vermeulen, M. J. Tiggelman, L. dos Santos Martins, B. Dirkse, *et al.*, "Realization of a multinode quantum network of remote solid-state qubits," *Science*, vol. 372, no. 6539, pp. 259–264, 2021.

[133] M. K. Bhaskar, R. Riedinger, B. Machielse, D. S. Levonian, C. T. Nguyen, E. N. Knall, H. Park, D. Englund, M. Lončar, D. D. Sukachev, *et al.*, "Experimental demonstration of memory-enhanced quantum communication," *Nature*, vol. 580, no. 7801, pp. 60–64, 2020.

[134] N. H. Nickerson, J. F. Fitzsimons, and S. C. Benjamin, "Freely scalable quantum technologies using cells of 5-to-50 qubits with very lossy and noisy photonic links," *Physical Review X*, vol. 4, no. 4, p. 041041, 2014.

[135] C. E. Bradley, J. Randall, M. H. Abobeih, R. Berrevoets, M. Degen, M. A. Bakker, M. Markham, D. Twitchen, and T. H. Taminiau, "A ten-qubit solid-state spin register with quantum memory up to one minute," *Physical Review X*, vol. 9, no. 3, p. 031045, 2019.

[136] A. Sipahigil, R. E. Evans, D. D. Sukachev, M. J. Burek, J. Borregaard, M. K. Bhaskar, C. T. Nguyen, J. L. Pacheco, H. A. Atikian, C. Meuwly, *et al.*, "An integrated diamond nanophotonics platform for quantum-optical networks," *Science*, vol. 354, no. 6314, pp. 847–850, 2016.

[137] R. E. Evans, M. K. Bhaskar, D. D. Sukachev, C. T. Nguyen, A. Sipahigil, M. J. Burek, B. Machielse, G. H. Zhang, A. S. Zibrov, E. Bielejec, *et al.*, "Photon-mediated interactions between quantum emitters in a diamond nanocavity," *Science*, vol. 362, no. 6415, pp. 662–665, 2018.

[138] A. L. Crook, C. P. Anderson, K. C. Miao, A. Bourassa, H. Lee, S. L. Bayliss, D. O. Bracher, X. Zhang, H. Abe, T. Ohshima, *et al.*, "Purcell enhancement of a single silicon carbide color center with coherent spin control," *Nano Letters*, vol. 20, no. 5, pp. 3427–3434, 2020.

[139] A. E. Rugar, S. Aghaeimeibodi, D. Riedel, C. Dory, H. Lu, P. J. McQuade, Z.-X. Shen, N. A. Melosh, and J. Vučković, "A quantum photonic interface for tin-vacancy centers in diamond," *Physical Review X*, vol. 11, p. 031021, 2021.

[140] K. Kuruma, B. Pingault, C. Chia, D. Renaud, P. Hoffmann, S. Iwamoto, C. Ronning, and M. Lončar, "Coupling of a single tin-vacancy center to a photonic crystal cavity in diamond," *Applied Physics Letters*, vol. 118, no. 23, p. 230601, 2021.

[141] S. Muralidharan, L. Li, J. Kim, N. Lütkenhaus, M. D. Lukin, and L. Jiang, "Optimal architectures for long distance quantum communication," *Scientific reports*, vol. 6, no. 1, pp. 1–10, 2016.

[142] E. Pelucchi, G. Fagas, I. Aharonovich, D. Englund, E. Figueroa, Q. Gong, H. Hannes, J. Liu, C.-Y. Lu, N. Matsuda, *et al.*, "The potential and global outlook of integrated photonics for quantum technologies," *Nature Reviews Physics*, pp. 1–15, 2021.

[143] B. Khanaliloo, M. Mitchell, A. C. Hryciw, and P. E. Barclay, "High-Q/V monolithic diamond microdisks fabricated with quasi-isotropic etching," *Nano Letters*, vol. 15, no. 8, pp. 5131–5136, 2015.

[144] N. H. Wan, T.-J. Lu, K. C. Chen, M. P. Walsh, M. E. Trusheim, L. De Santis, E. A. Bersin, I. B. Harris, S. L. Mouradian, I. R. Christen, *et al.*, "Large-scale integration of artificial atoms in hybrid photonic circuits," *Nature*, vol. 583, no. 7815, pp. 226–231, 2020.

[145] C. Babin, R. Stöhr, N. Morioka, T. Linkewitz, T. Steidl, R. Wörnle, D. Liu, E. Hesselmeier, V. Vorobyov, A. Denisenko, *et al.*, "Fabrication and nanophotonic waveguide integration of silicon carbide colour centres with preserved spin-optical coherence," *Nature Materials*, p. 67–73, 2022.

[146] S. Aghaeimeibodi, D. Riedel, A. E. Rugar, C. Dory, and J. Vučković, "Electrical tuning of tin-vacancy centers in diamond," *Physical Review Applied*, vol. 15, no. 6, p. 064010, 2021.

[147] L. De Santis, M. Trusheim, K. Chen, and D. Englund, "Investigation of the Stark effect on a centrosymmetric quantum emitter in diamond," *Physical Review Letters*, vol. 127, p. 147402, 2021.

[148] C. Bradac, W. Gao, J. Forneris, M. E. Trusheim, and I. Aharonovich, "Quantum nanophotonics with group IV defects in diamond," *Nature Communications*, vol. 10, no. 1, p. 5625, 2019.

[149] P. Udvarhelyi, R. Nagy, F. Kaiser, S.-Y. Lee, J. Wrachtrup, and A. Gali, "Spectrally stable defect qubits with no inversion symmetry for robust spin-to-photon interface," *Physical Review Applied*, vol. 11, no. 4, p. 044022, 2019.

[150] Ö. Soykal, P. Dev, and S. E. Economou, "Silicon vacancy center in 4H-SiC: Electronic structure and spin-photon interfaces," *Physical Review B*, vol. 93, no. 8, p. 081207, 2016.

[151] H. B. Banks, Ö. O. Soykal, R. L. Myers-Ward, D. K. Gaskill, T. Reinecke, and S. G. Carter, "Resonant Optical Spin Initialization and Readout of Single Silicon Vacancies in 4H-SiC," *Physical Review Applied*, vol. 11, no. 2, p. 024013, 2019.

[152] N. Morioka, C. Babin, R. Nagy, I. Gediz, E. Hesselmeier, D. Liu, M. Joliffe, M. Niethammer, D. Dasari, V. Vorobyov, *et al.*, "Spin-controlled generation of indistinguishable and distinguishable photons from silicon vacancy centres in silicon carbide," *Nature Communications*, vol. 11, no. 1, p. 2516, 2020.

[153] R. Nagy, D. B. R. Dasari, C. Babin, D. Liu, V. Vorobyov, M. Niethammer, M. Widmann, T. Linkewitz, I. Gediz, R. Stöhr, *et al.*, "Narrow inhomogeneous distribution of spin-active emitters in silicon carbide," *Applied Physics Letters*, vol. 118, no. 14, p. 144003, 2021.

[154] A. Bourassa, C. P. Anderson, K. C. Miao, M. Onizhuk, H. Ma, A. L. Crook, H. Abe, J. Ul-Hassan, T. Ohshima, N. T. Son, *et al.*, "Entanglement and control of single nuclear spins in isotopically engineered silicon carbide," *Nature Materials*, vol. 19, no. 12, pp. 1319–1325, 2020.

[155] E. Waks and J. Vuckovic, "Dipole induced transparency in drop-filter cavity-waveguide systems," *Physical Review Letters*, vol. 96, no. 15, p. 153601, 2006.

[156] K. Srinivasan and O. Painter, "Optical fiber taper coupling and high-resolution wavelength tuning of microdisk resonators at cryogenic temperatures," *Applied Physics Letters*, vol. 90, no. 3, p. 031114, 2007.

[157] D. M. Lukin, M. A. Guidry, J. Yang, M. Ghezellou, S. D. Mishra, H. Abe, T. Ohshima, J. Ul-Hassan, and J. Vučković, "Two-emitter multimode cavity quantum electrodynamics in thin-film silicon carbide photonics," *Physical Review X*, vol. 13, no. 1, p. 011005, 2023.

[158] J. L. Zhang, S. Sun, M. J. Burek, C. Dory, Y.-K. Tzeng, K. A. Fischer, Y. Kelaita, K. G. Lagoudakis, M. Radulaski, Z.-X. Shen, *et al.*, "Strongly cavity-enhanced spontaneous emission from silicon-vacancy centers in diamond," *Nano Letters*, vol. 18, no. 2, pp. 1360–1365, 2018.

[159] D. O. Bracher, X. Zhang, and E. L. Hu, "Selective Purcell enhancement of two closely linked zero-phonon transitions of a silicon carbide color center," *Proceedings of the National Academy of Sciences*, vol. 114, no. 16, pp. 4060–4065, 2017.

[160] A. Faraon, P. E. Barclay, C. Santori, K.-M. C. Fu, and R. G. Beausoleil, "Resonant enhancement of the zero-phonon emission from a colour centre in a diamond cavity," *Nature Photonics*, vol. 5, no. 5, pp. 301–305, 2011.

[161] D. Riedel, I. Söllner, B. J. Shields, S. Starosielec, P. Appel, E. Neu, P. Maletinsky, and R. J. Warburton, "Deterministic enhancement of coherent photon generation from a nitrogen-vacancy center in ultrapure diamond," *Physical Review X*, vol. 7, no. 3, p. 031040, 2017.

[162] J.-H. Kim, S. Aghaeimeibodi, C. J. Richardson, R. P. Leavitt, and E. Waks, "Super-radiant emission from quantum dots in a nanophotonic waveguide," *Nano Letters*, vol. 18, no. 8, pp. 4734–4740, 2018.

[163] J. Q. Grim, A. S. Bracker, M. Zalalutdinov, S. G. Carter, A. C. Kozen, M. Kim, C. S. Kim, J. T. Mlack, M. Yakes, B. Lee, *et al.*, "Scalable in operando strain tuning in nanophotonic waveguides enabling three-quantum-dot superradiance," *Nature materials*, vol. 18, no. 9, pp. 963–969, 2019.

[164] B. Machielse, S. Bogdanovic, S. Meesala, S. Gauthier, M. J. Burek, G. Joe, M. Chalupnik, Y.-I. Sohn, J. Holzgrafe, R. E. Evans, *et al.*, "Quantum interference of electromechanically stabilized emitters in nanophotonic devices," *Physical Review X*, vol. 9, no. 3, p. 031022, 2019.

[165] C. P. Anderson, E. O. Glen, C. Zeledon, A. Bourassa, Y. Jin, Y. Zhu, C. Vorwerk, A. L. Crook, H. Abe, J. Ul-Hassan, T. Ohshima, N. T. Son, G. Galli, and D. D. Awschalom, "Five-second coherence of a single spin with single-shot readout in silicon carbide," *Science Advances*, vol. 8, no. 5, p. eabm5912, 2022.

[166] P. Udvarhelyi, G. Thiering, N. Morioka, C. Babin, F. Kaiser, D. Lukin, T. Ohshima, J. Ul-Hassan, N. T. Son, J. Vučković, *et al.*, "Vibronic states and their effect on the temperature and strain dependence of silicon-vacancy qubits in 4H-SiC," *Physical Review Applied*, vol. 13, no. 5, p. 054017, 2020.

[167] N. C. Harris, G. R. Steinbrecher, M. Prabhu, Y. Lahini, J. Mower, D. Bunandar, C. Chen, F. N. Wong, T. Baehr-Jones, M. Hochberg, *et al.*, "Quantum transport simulations in a programmable nanophotonic processor," *Nature Photonics*, vol. 11, no. 7, p. 447, 2017.

[168] W. H. Pernice, C. Schuck, O. Minaeva, M. Li, G. Goltsman, A. Sergienko, and H. Tang, "High-speed and high-efficiency travelling wave single-photon detectors embedded in nanophotonic circuits," *Nature communications*, vol. 3, no. 1, pp. 1–10, 2012.

[169] F. Najafi, J. Mower, N. C. Harris, F. Bellei, A. Dane, C. Lee, X. Hu, P. Kharel, F. Marsili, S. Assefa, *et al.*, "On-chip detection of non-classical light by scalable integration of single-photon detectors," *Nature communications*, vol. 6, no. 1, pp. 1–8, 2015.

[170] I. Esmaeil Zadeh, J. W. Los, R. B. Gourgues, J. Chang, A. W. Elshaari, J. R. Zichi, Y. J. van Staaden, J. P. Swens, N. Kalhor, A. Guardiani, *et al.*, "Efficient single-photon detection with 7.7 ps time resolution for photon correlation measurements," *ACS Photonics*, 2020.

[171] F. Eltes, G. E. Villarreal-Garcia, D. Caimi, H. Siegwart, A. A. Gentile, A. Hart, P. Stark, G. D. Marshall, M. G. Thompson, J. Barreto, *et al.*, "An integrated optical modulator operating at cryogenic temperatures," *Nature Materials*, pp. 1–5, 2020.

[172] H.-K. Lau, H. Qiao, A. A. Clerk, and T. Zhong, "Efficient in-situ generation of photon-memory entanglement in a nonlinear cavity," *arXiv preprint arXiv:2208.00886*, 2022.